

## 5.0 MELTER EXAMINATION

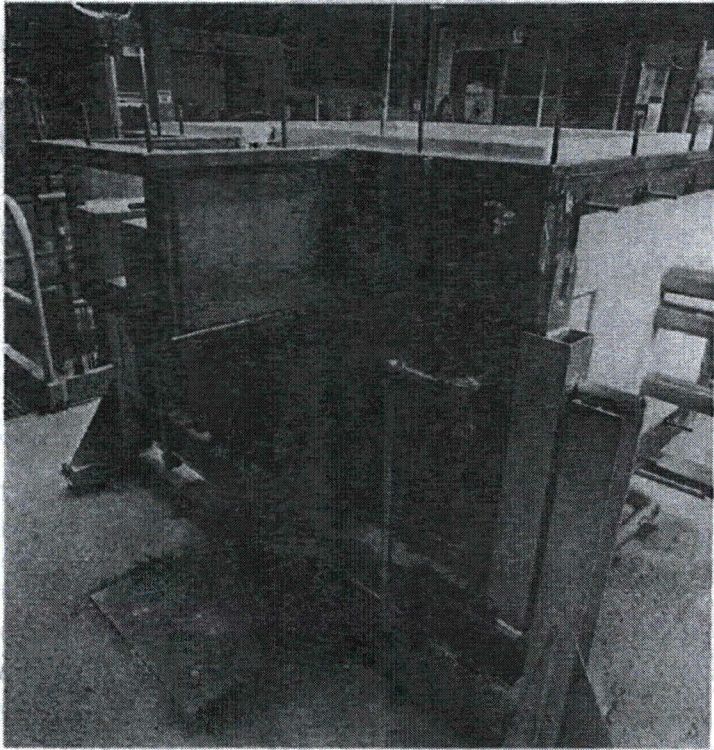
The following sections discuss the observations made of the melter condition during dismantling. The mechanisms producing the observed corrosion of the Monofrax K-3, Alfrax 66, electrodes, ionic booster electrodes and offgas piping are presented in Section 7.0.

### 5.1 CONTAINMENT BOX AND LID

Following the melter draining, the external insulation was removed from the stainless steel containment box. The melter box was found to be in generally good condition, with a few discolored areas from exposure to elevated temperatures. The areas of discoloration were found primarily in the overflow drain section where the internal insulation was at a minimum. The only physical distortion of the containment box was bowing of the lower south-east cooling jacket. This deflection, shown in Figure 22, was probably the result of the elimination of the water coolant flow in the lower cooling jackets. This change was intended to increase the operating temperature of the refractory near the melter floor to minimize the deposition of precipitates from the glass. Following the coolant shut off, sufficient steam pressure to cause the bowing could have occurred as residual water in the jacket began to boil. Also, if the melter drain system pressurized, water could have been injected into the cooling jacket producing the same results. Minor changes in the cooling system design to reduce the coolant flow restrictions can eliminate this problem.

The lid assembly was more seriously affected by the melter operating cycles. Figure 23 shows the melter lid following removal. The photograph illustrates the bowing of the assembly's vertical surfaces, tears in the flanges where the lid is joined to the melter box, and the warpage of the cover plate.

The difference in the condition of the lid and melter box was expected as the containment box was protected by substantial internal insulation, whereas the lid assembly was insulated only externally. The lid, therefore, experienced the full effects of the thermal cycling induced during the operation of the melter.



**APPEARANCE OF  
COOLING JACKETS  
DURING  
CONSTRUCTION**



**DISTORTED  
COOLING  
JACKET**

**FIGURE 22.** Distortion of Lower Southeast Containment Box Cooling Jacket

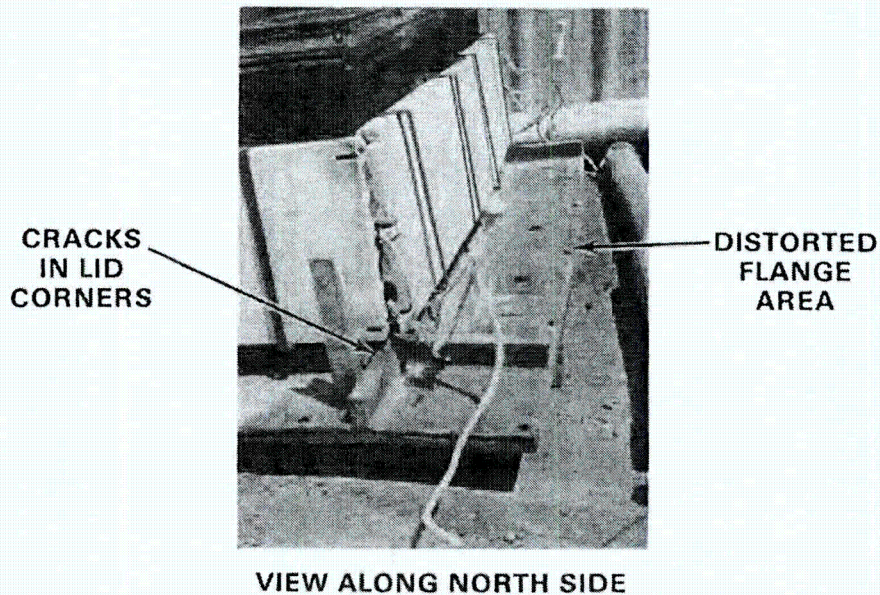
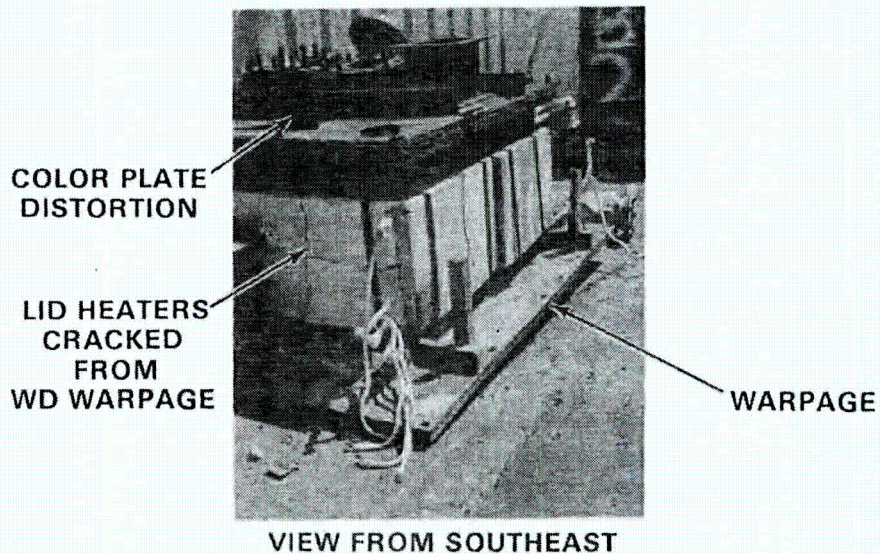


FIGURE 23. Melter Lid Assembly Following Removal

Because lid heaters were installed on the exterior surface of the lid, it also served as a radiative heat source during the melter startup and on other occasions when the external lid heaters were employed. The thermal cycling caused by normal operations, combined with periods of lid heater use resulted in the lid warpage. In some locations, the lid warpage was sufficient to crack the lid heaters, as shown in Figure 23.

The tears in the lid, which developed in each of the corners, are also the result of temperature cycling. Free thermal expansion of the lid was restrained by the water-cooled melter box. This restricted thermal expansion, combined with the different thermal expansion coefficient for the stainless steel and Inconel 601 components, caused the lid weld failures.

The operating temperature cycles and stress concentrations from the numerous penetrations, welds, and dissimilar construction metals account for the severe warpage of the cover plate. The cover plate deformation explains air inleakage experienced early in the operating life of the melter. The distortion of the cover plate, combined with the high-temperature degradation of the asbestos gasketing material initially used to seal the cover plate to the lid assembly, forced the removal of the asbestos rope and the welding of the cover plate to the lid assembly to seal the melter.

## 5.2 RESIDUAL GLASS AND SLAG

The melting cavity contained significant quantities of residual glass and precipitated crystals (slag) after the melter was drained, as pictured in Figure 24. The slag in this photograph covers approximately the bottom 7.5 cm

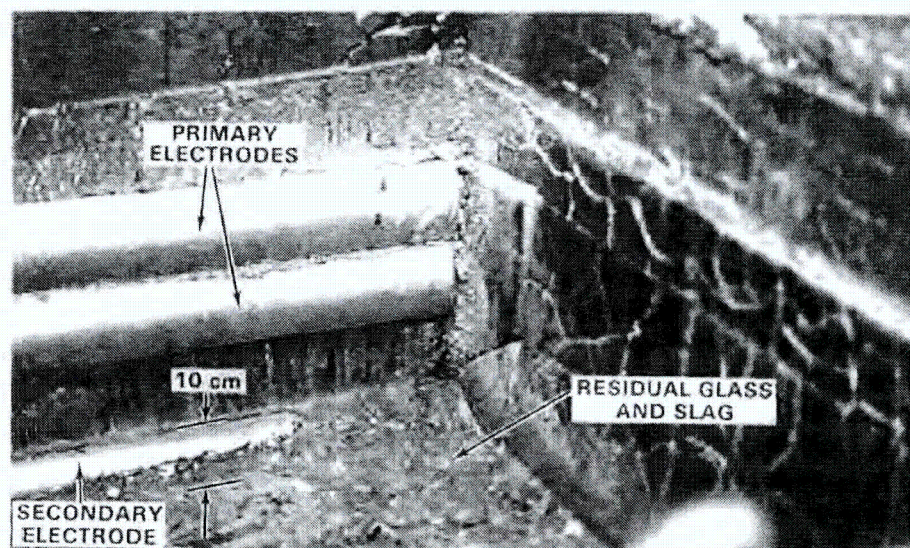


FIGURE 24. Slag and Residual Glass Remaining on Melter Floor Following Shutdown

of the 10.2-cm secondary electrode. Figure 25 is a contour plot of the melter floor showing the depth of slag deposits in centimeters. The empty area in the figure is an area on the melter floor where the slag deposits were disturbed in an early effort to determine the condition of the riser inlet nozzle. Thus, accurate measurement of the slag deposit depth in this region could not be determined.

From Figure 25 it is apparent that there is a slag depth gradient from the electrode walls down to the center. Also, the deposits in the corners of the north wall are deeper than the corresponding corners of the south wall. This pattern is the result of the corners and edges being the coldest locations along the melter floor (thereby tending to precipitate crystalline phases), and of the two convection cells that are present in the melter. These major convection cells were predicted by melter modeling (Quigley and Kreid 1979). The convection cells rise along the melter's east-west

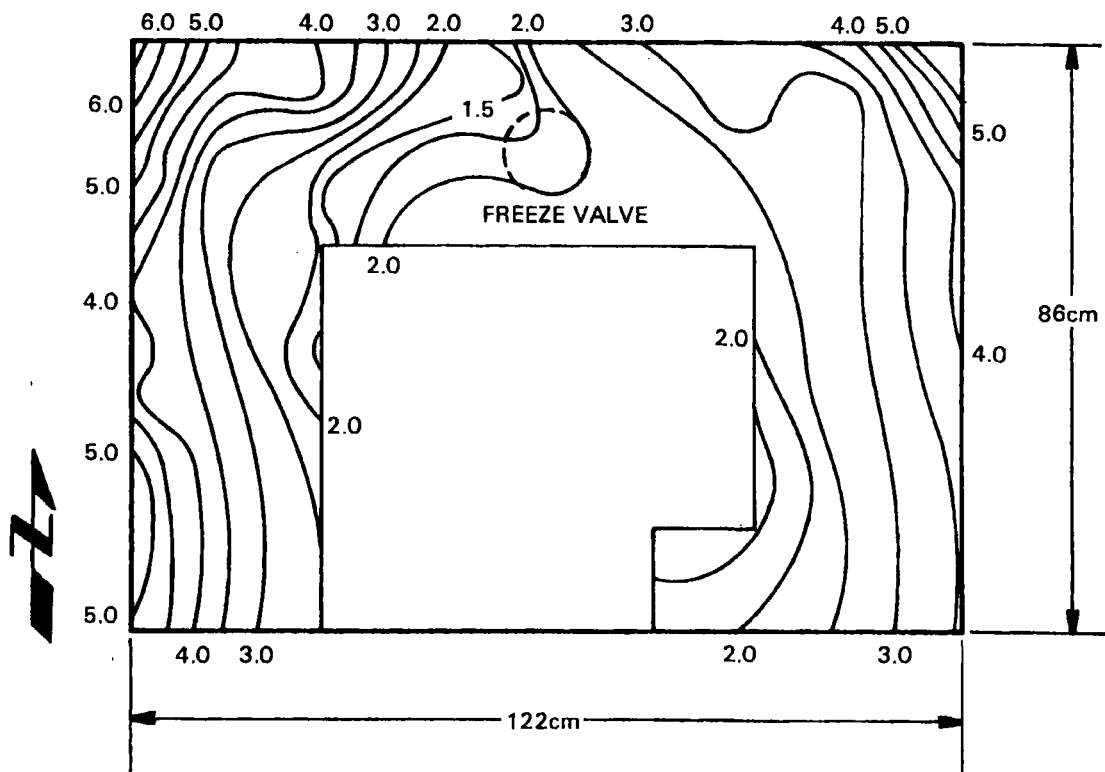


FIGURE 25. Depth at Slag Deposits in LFCM (cm)

centerline, flow toward the electrode walls, and sweep across the electrodes and the melter floor, producing slag accumulations in the relatively stagnant zones at the base of the electrodes.

The fact that the deposits are deepest along the north wall suggests that the slag has a tendency to accumulate on the north side because of the sloping of the melter floor during the idling periods. Typically, when the melter idles, the LFCM is oriented with a  $2^{\circ}$  tilt from horizontal toward the north. Also, the north wall would be generally cooler than the south wall because the overflow drain heading would affect the south wall temperature profiles. The two major operational concerns about the slag layer were whether the slag would grow deep enough to block the riser drain inlet nozzle or prevent the freeze valve from functioning. The slag deposits on the LFCM floor did not interfere with either of these melter operations.

One of the objectives of this investigation was to determine if the concentration of any of the feed chemicals in the slag was greater at one location than at another. This was accomplished by systematically excavating the slag deposit by grids. The grid pattern is shown in Figure 26. Samples were

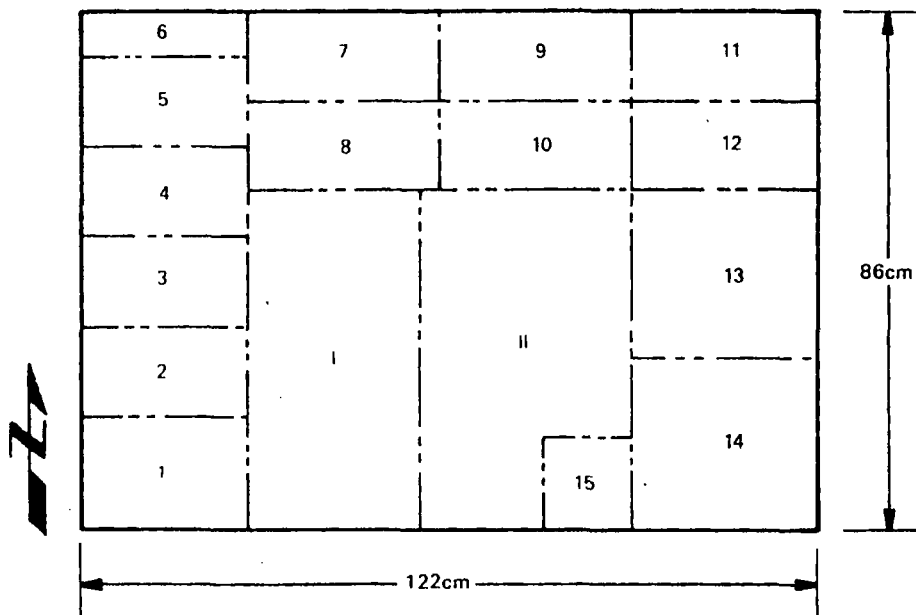


FIGURE 26. Slag Excavation Grid Pattern on LFCM Floor

removed from the various grids and examined by x-ray fluorescence to determine the composition. The results of the analysis are presented in Figures 27 and 28. The results are inconclusive because the elemental concentrations were not found to be constant among the samples removed from a particular grid. However, two findings are apparent from this data. First, the samples containing relatively large concentrations of cerium oxide were removed from areas of the melter floor containing the deepest deposits. This was expected because cerium was a feed component only in the early melter tests and therefore should be found in the older, deeper slag deposits.

Second, a relationship between the concentrations of two groups of elements in the slag was observed. The concentration of Ce, Cr, and Zn vary inversely with the concentration of Fe, Mn, and Ni for all of the locations on the melter floor. This relationship is a result of the time that the slag was formed. The data indicate that the slags formed during the early processing tests were cerium oxide, Zn-Cr spinel, and chromium oxide. These chemicals were common components of the early feeds. Also, the release of  $\text{Cr}_2\text{O}_3$  from the Monofrax K-3 corrosion would be expected to be maximum during the early tests before the spinel layers on the refractory were fully developed. The more recent process test feeds, however, contained substantial quantities of iron, manganese, and nickel, and would tend to form (Mn, Ni)  $\text{Fe}_2\text{O}_4$  spinels. Therefore, the variation in the slag composition is a result of the operating period during which they were formed.

The appearance of the slag is pictured in Figure 29. The samples pictured here were removed from the upper layers of the slag. The composition of the material was shown to be primarily a spinel,  $[(\text{Fe},\text{Mn},\text{Ni})(\text{Fe},\text{Cr})_2\text{O}_4]$ , with sporadic appearances of other crystalline phases. In general, the slag was found to be a complex mixture of glass compositions, Mn-Ni-Fe-Cr spinels, Cr-Fe-Zr crystals,  $\text{CeO}_2$  deposits,  $\text{Al}_2\text{O}_3$  nodules, Ru phases, and trace quantities of all of the other feed components. Additionally, a metallic nickel alloy with small quantities of chromium and iron was found in the slag.

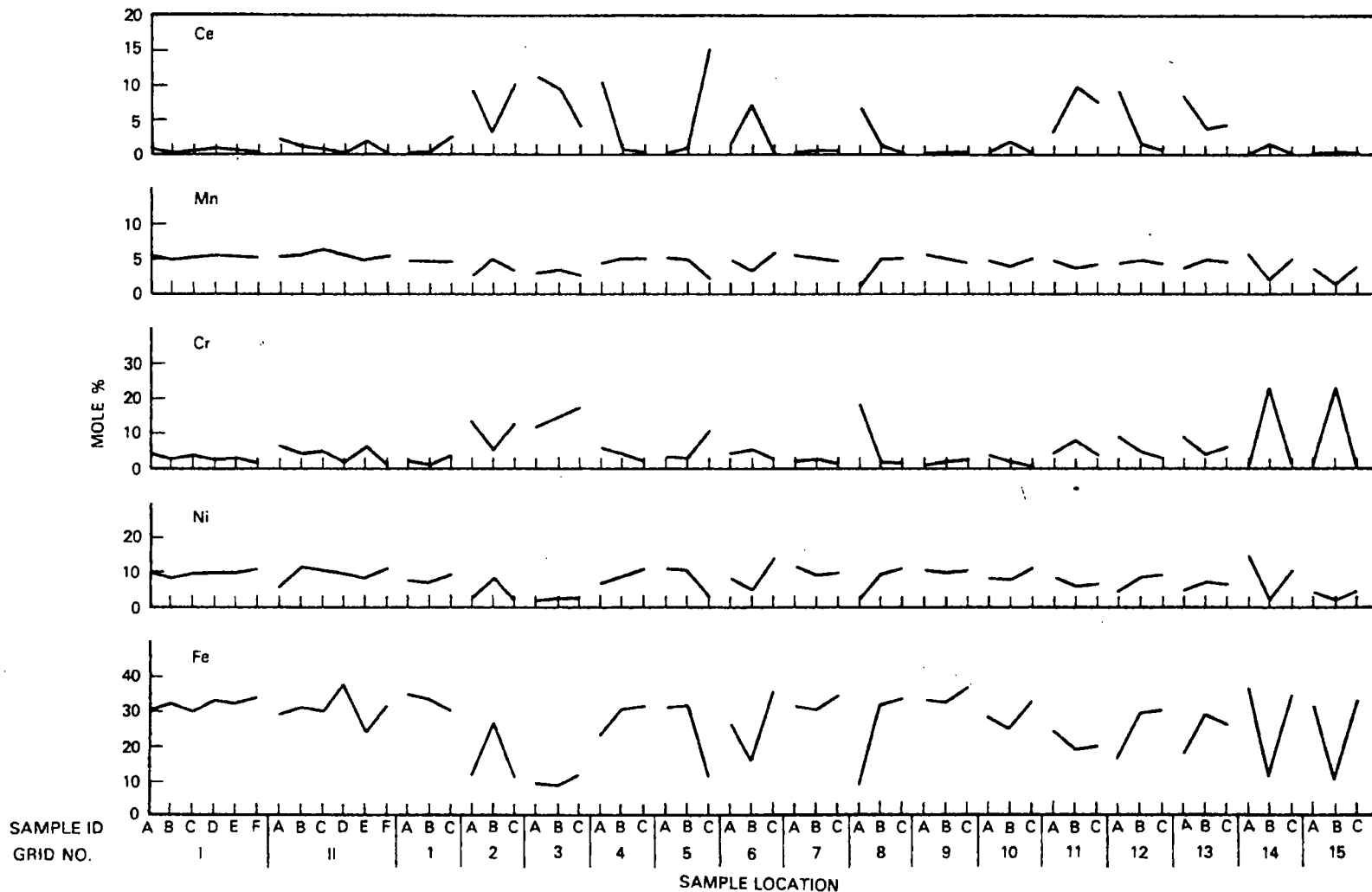


FIGURE 27. Metal Concentrations for Samples Removed from the LFCM Slag, by Grid Number

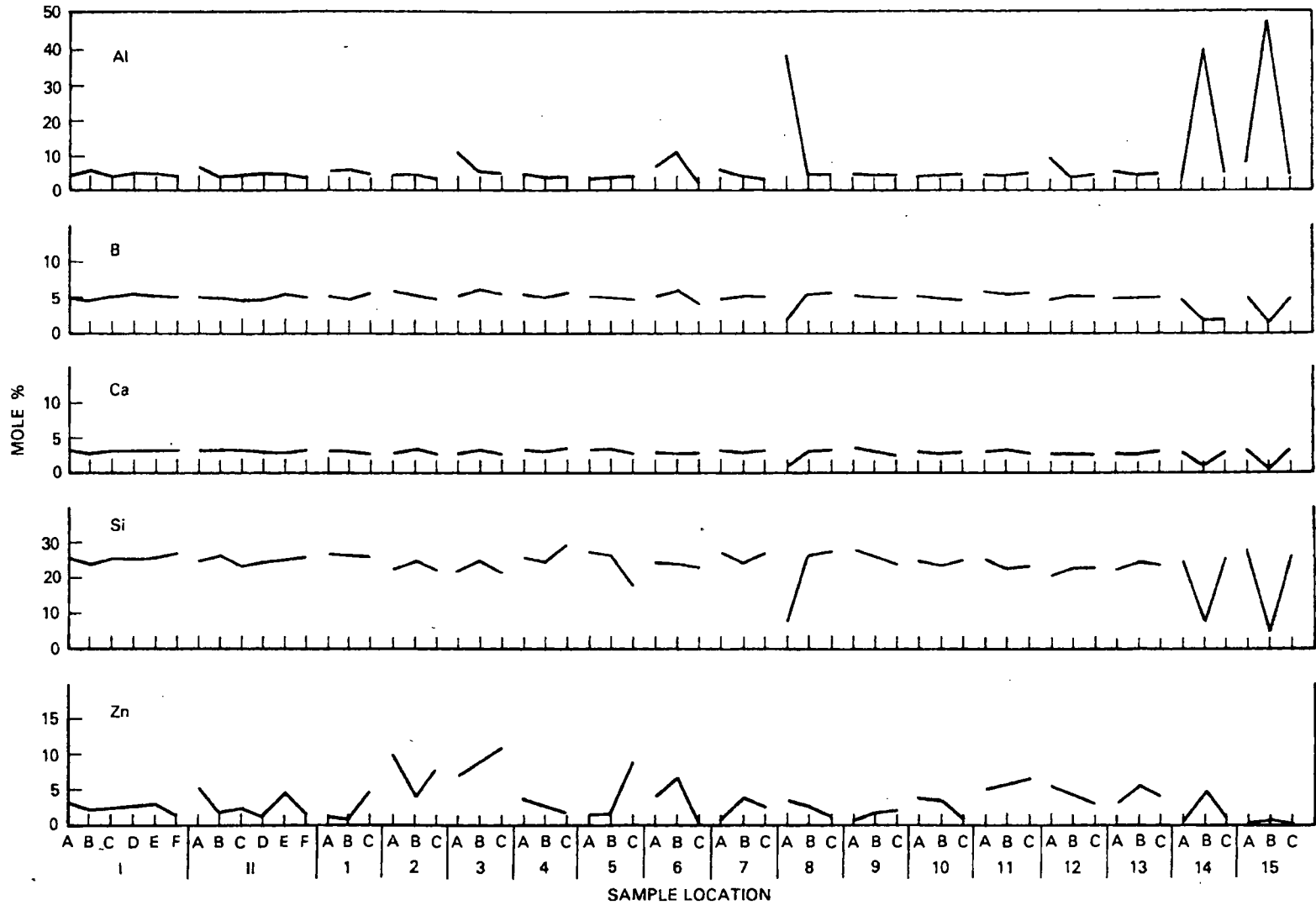


FIGURE 28. Chemical Concentrations for Samples Removed from the LFCM Slag, by Grid Number



FIGURE 29. Enlargement of Slag Sample Removed from Grid Sector II

### 5.3 MELTING CAVITY REFRACTORY

The following section discusses the condition of the various melter refractory components.

#### 5.3.1 Monofrax K-3

The Monofrax K-3 refractory following the melter shut down is pictured in Figures 30, 31, and 32. The most apparent features are the general uniformity of the cracking present in the bricks and the intact cold wall (wall opposite

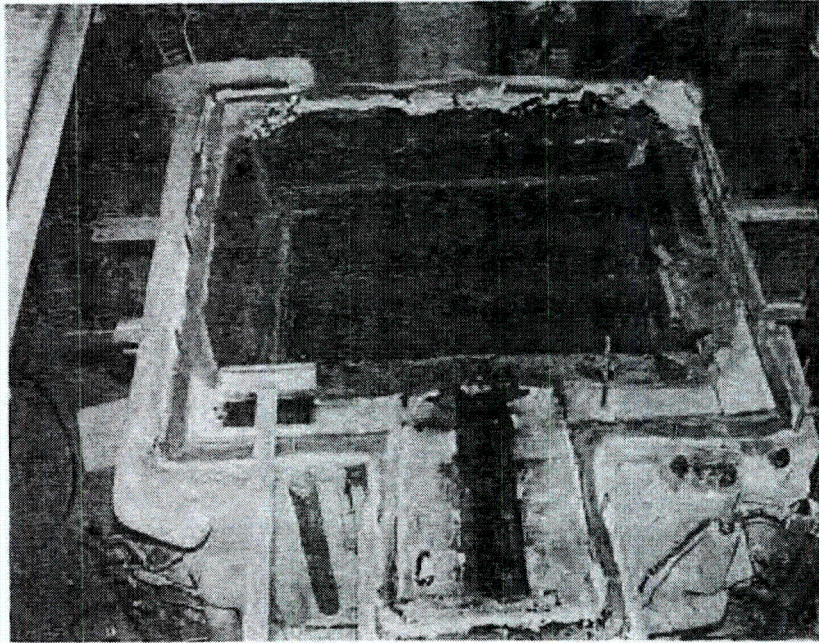


FIGURE 30. Melting Cavity North Monofrax K-3 Wall

the melting cavity drain), whereas several large brick pieces have fallen from the hot wall (south wall). The difference between these refractory walls can also be seen by comparing Figures 33 and 34. These figures are representative of the wall contours. The contours were measured in centimeters from a plane set at an arbitrary distance from the wall. The numbers reported are the distances from this plane to the wall. Because the contour numbers reported for a particular wall are based on a common plane, the changes in the surface characteristics from one point to another are obtained by subtracting the contour magnitudes at the points of interest.

The photographs and respective contour plots display the difference between the conditions of the north and south walls. The mechanisms for crack formation in the Monofrax K-3 is discussed in detail in the stress analysis section of this report (Section 6.0). Briefly, the Monofrax K-3 cracking is due to excessive stresses developed by thermal expansion, and thermal shocking of the refractory during liquid-feed initiation.

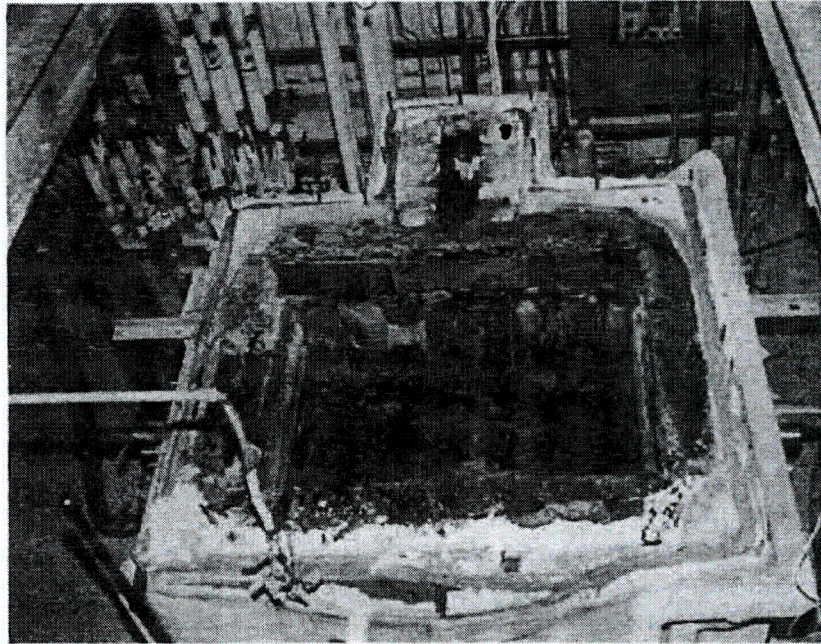


FIGURE 31. Melting Cavity South Monofrax K-3 Wall

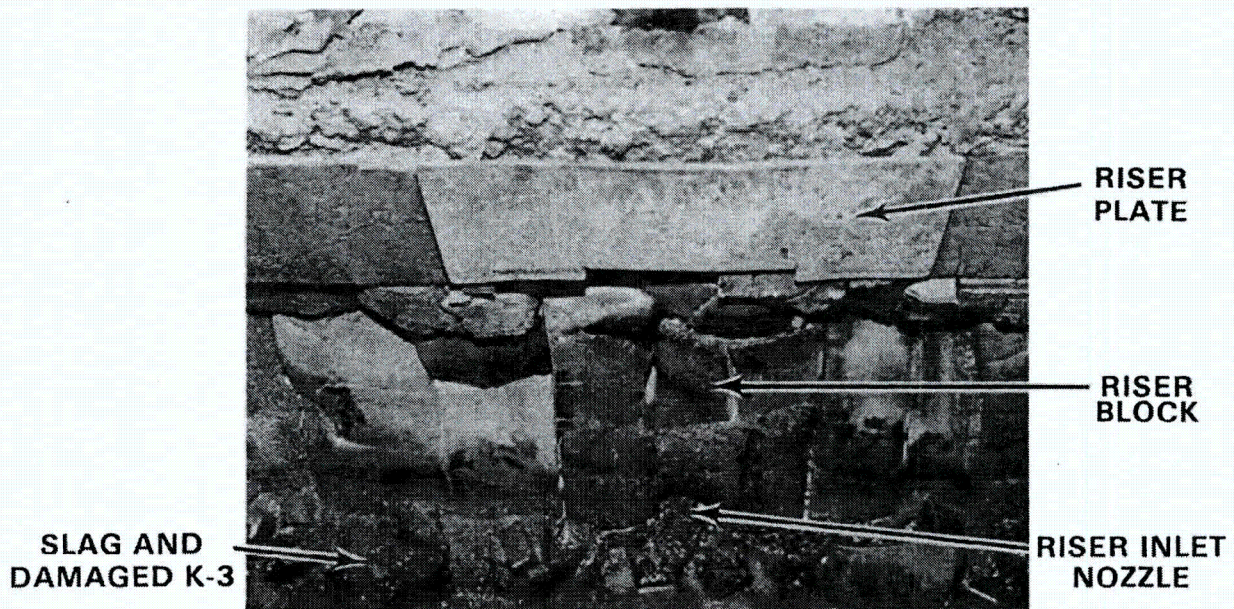


FIGURE 32. Cracking Around LFCM Riser Block

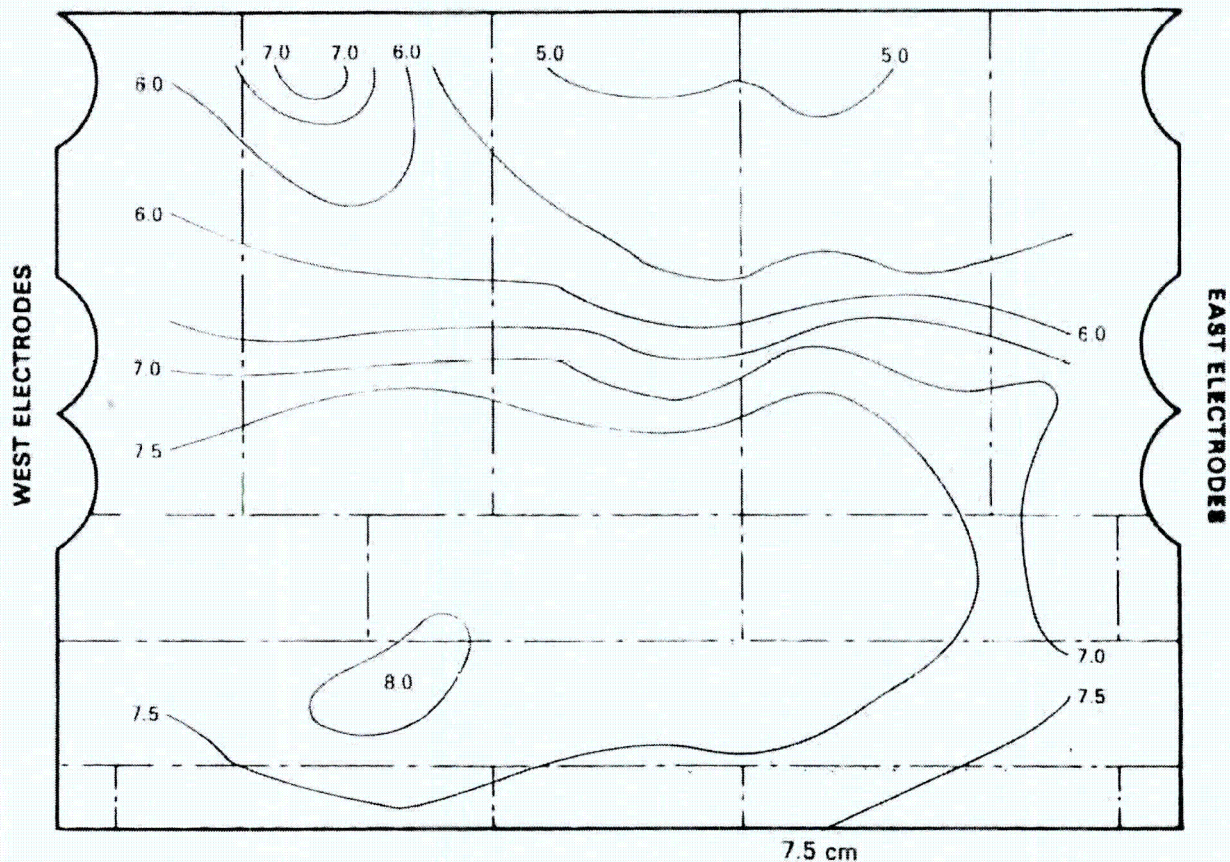
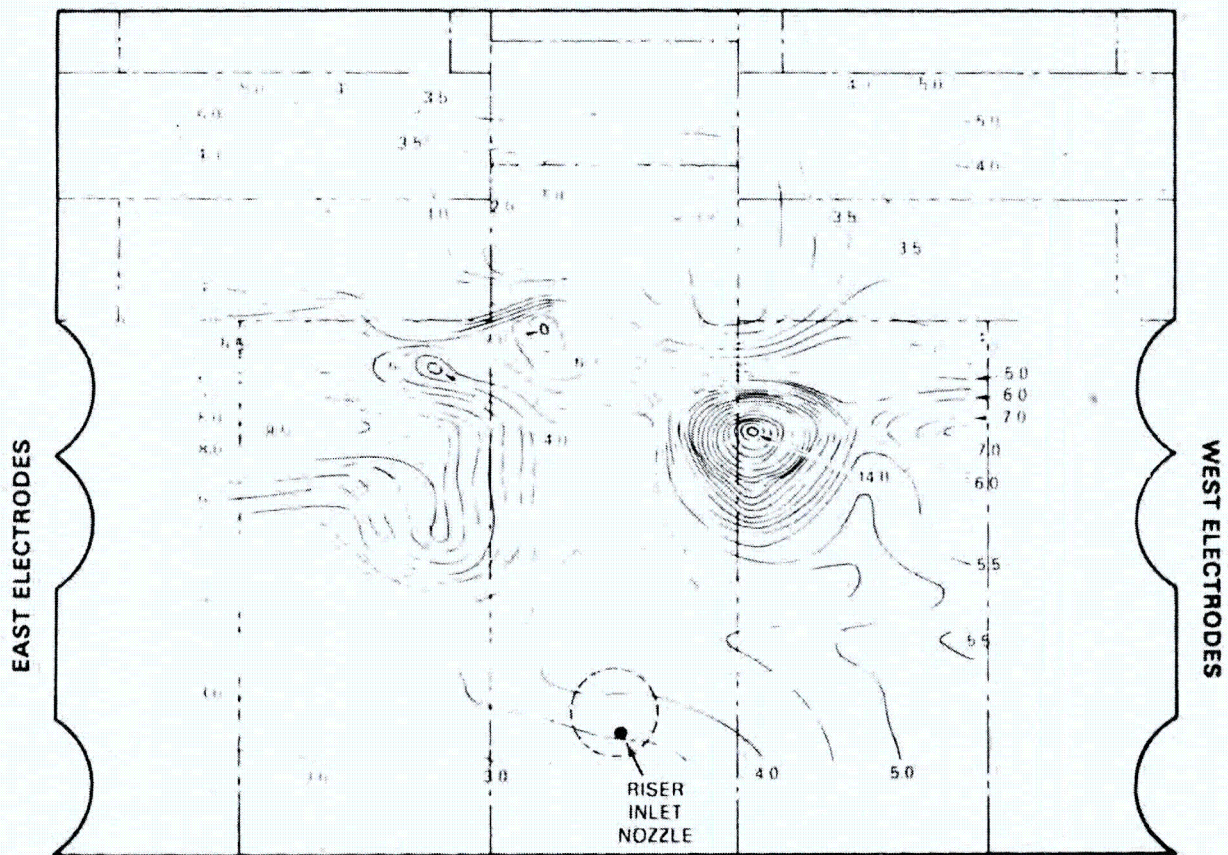


FIGURE 33. Contour Plot of Melting Cavity North Wall Following Drainage

Although both refractory walls are severely cracked, the cold wall remains intact because the cracks are oriented perpendicularly to the glass contact face. This is due to the characteristics of the temperature distribution in the wall. However, the thermal gradients present in the hot wall are oriented such that the cracks are inclined with respect to the glass contact face. Therefore, the cracked portions of the north wall remain in place, but the damaged south wall refractory tended to slough off onto the floor.

Another indication that high refractory stresses are present can be seen in the photograph and contour plot of the east electrode wall, Figures 35 and 36. The refractory above the primary electrodes has bowed toward the melting



**FIGURE 34.** Contour Plot of Refractory South Wall Following Drainage

cavity to relieve the thermal expansion stresses. Similar refractory displacement was produced in the west melting cavity wall.

In general, the Monofrax K-3 was found to be highly corrosion resistant. The north wall underwent a generally uniform corrosion, with the maximum loss of roughly 2.5 cm at the center. The flat corrosion profile of this refractory is established very near the electrodes, as can be seen in Figure 37. The riser drain is another example of the applicability of Monofrax K-3. Figures 38 and 39 are photographs of the drain. The riser inlet has grown during service (original size of inlet shown in Figure 38) as the slag built up, yet the riser itself remains circular and in good condition (Figure 39). The

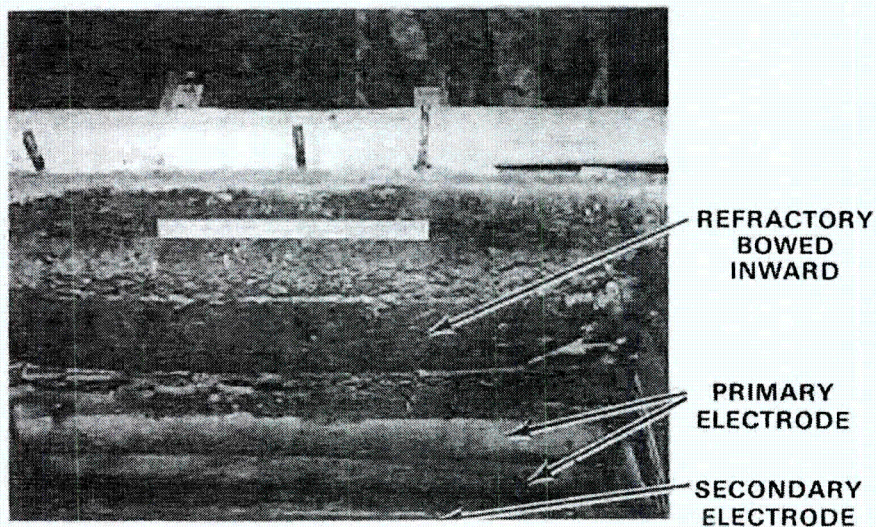


FIGURE 35. Melting Cavity East Electrode Wall

Monofrax K-3 forming the melter floor remains in nearly new condition, remaining at the original 6-in. (15.2-cm) thickness, as shown in Figure 40.

#### 5.3.2 Alfrax 66

Alfrax 66, a high alumina castable refractory, was installed behind the Monofrax K-3 in the walls. When the melter was disassembled, the surface of the Alfrax 66 behind the Monofrax K-3 was covered with a thin glass film. The Alfrax 66 found to be largely unaffected by contact with the glass, appears well suited for the corrosive environments of this application.

As the disassembly progressed, the Alfrax 66 was found to contain many glass-filled cracks. This was especially true in the Alfrax 66 cast around the riser block, Figure 41. A significant quantity of glass penetrated the Alfrax 66 along the north wall. One of the large glass-filled cracks and the large glass pool behind the Alfrax 66 are pictured in Figure 42. This was by far the largest glass penetration found in the examination, forming a solidified layer against the containment box roughly 75-cm by 60-cm by 0.5-cm thick. Minor glass migrations were also found behind the electrodes, but the glass did not penetrate the Alfrax 66 to the containment box in this region

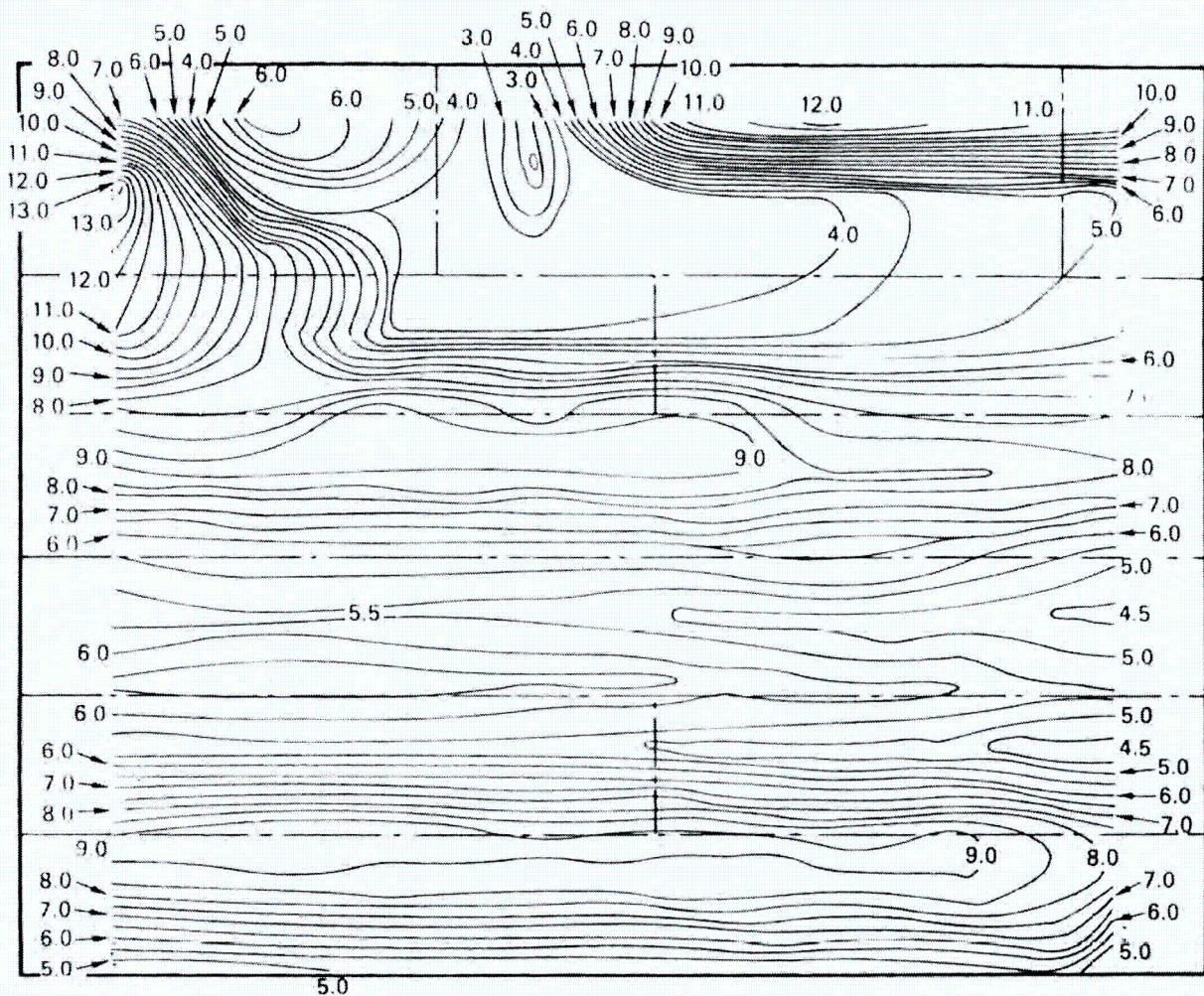


FIGURE 36. Contour Plot of East Electrode Wall

The Alfrax 66 was subjected to conditions most likely to create structural failures in the LFCM application. Alfrax 66 is a castable refractory (mixed with water and cast into place, much like concrete). The solidified Alfrax 66 contains both free water and water of hydration. As the temperature of the refractory exceeds  $100^{\circ}\text{C}$ , the free water begins to vaporize, forming microscopic steam pockets in the refractory. If this water vapor is not allowed to diffuse from the Alfrax 66 (by maintaining the refractory near

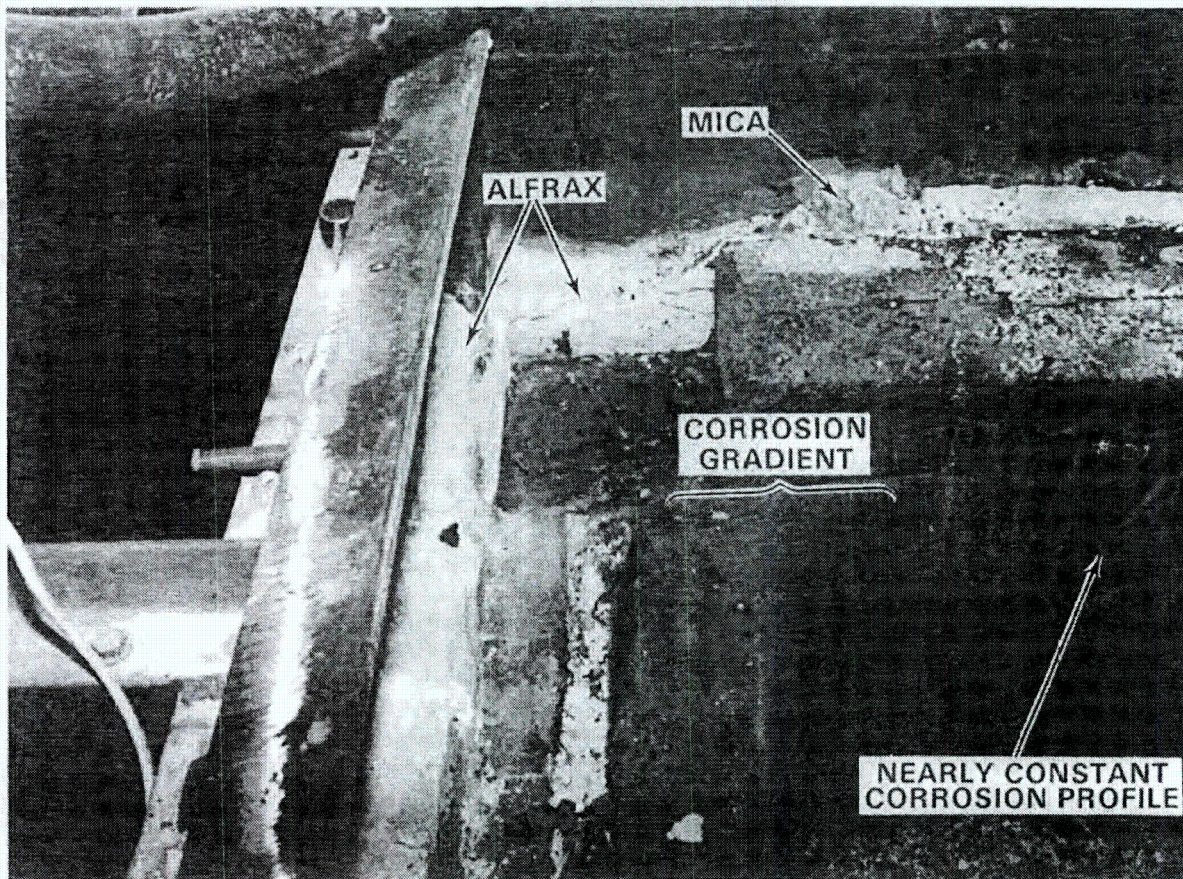


FIGURE 37. Corrosion Profile on North Wall Near Electrodes

100°C) for an extended time period, the internal steam pressure can build until refractory failure occurs. During the melter startup, the melter was heated from ambient to operating temperatures in less than 24 h. This is in sharp contrast to the Alfrax 66 curing schedule recommended by the manufacturer:

- Maintain Alfrax 66 temperatures between 95 to 120°C until visible steam condensation in the coolest melter region ceases.
- Increase the Alfrax 66 temperature (<40°C/h) to 480°C.
- Between 400 to 650°C, reduce the temperature increase to <30°C/h to permit dissipation of hydrated water released in this temperature range.

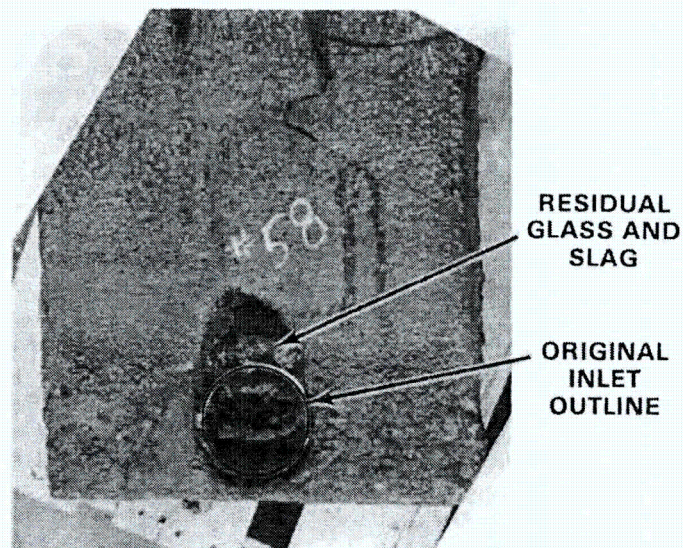


FIGURE 38. Corrosion of Riser Inlet Nozzle

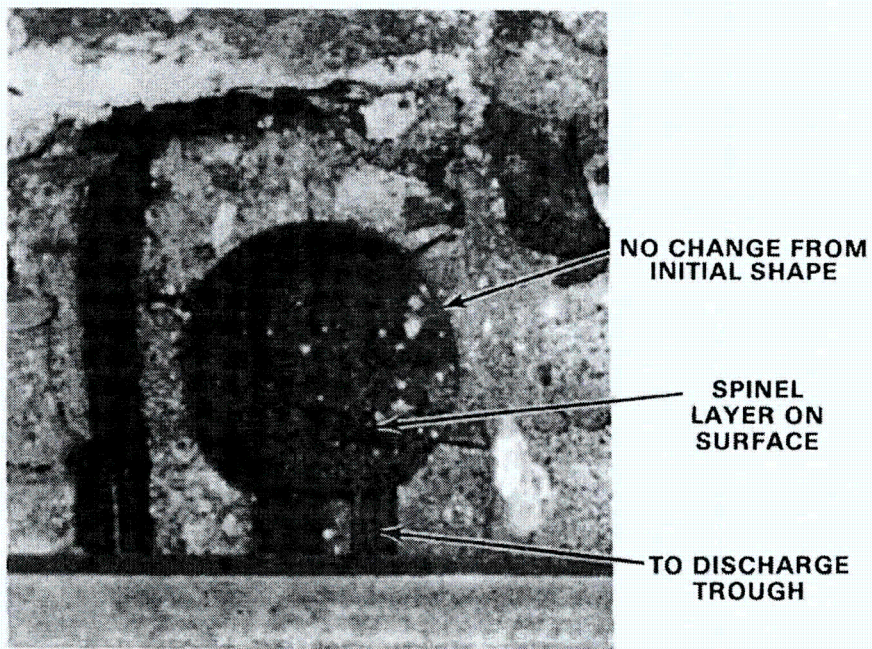


FIGURE 39. Condition of Riser Outlet Following Operating Period

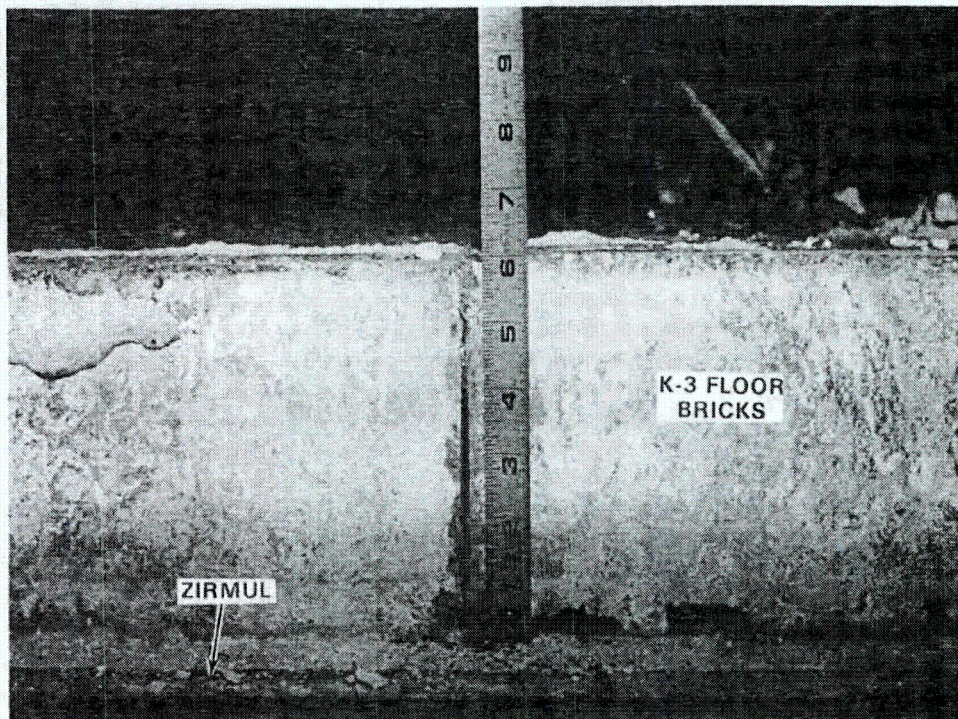


FIGURE 40. Condition of Monofrax K-3 Floor Blocks

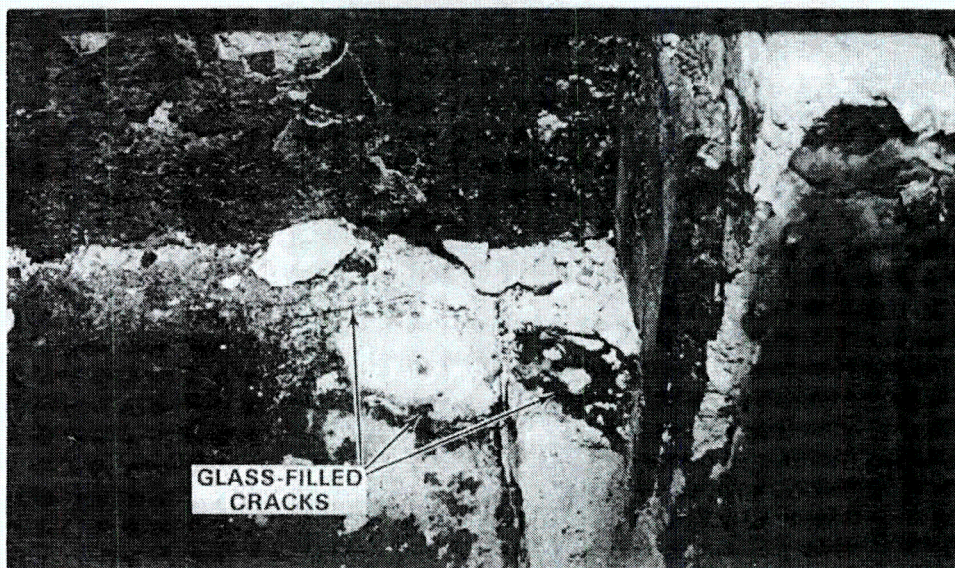


FIGURE 41. Cracking of Alfrax 66 Around Riser Block

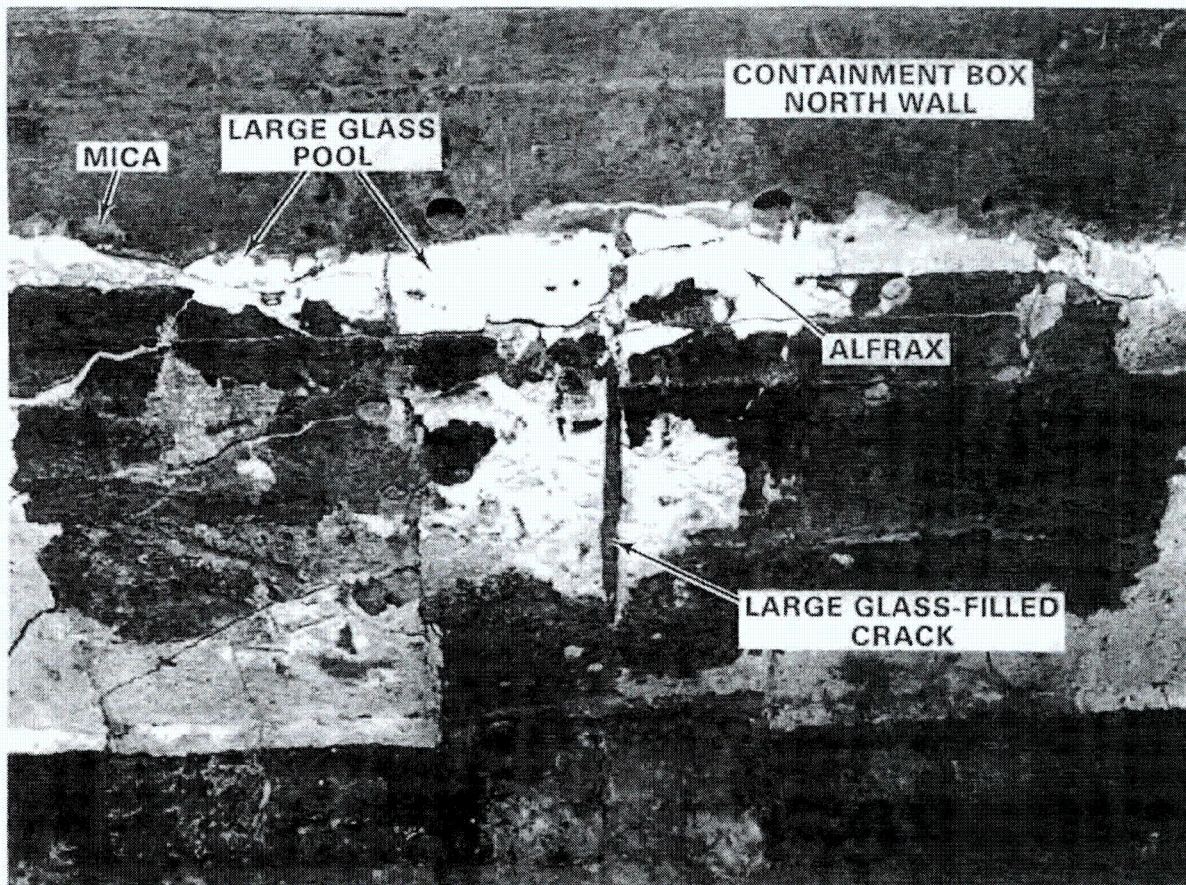


FIGURE 42. Glass Penetration Through Alfrax 66 North Wall

- Above 650<sup>0</sup>C, increase Alfrax 66 temperatures <40<sup>0</sup>C/h until the desired operating temperature is reached.

After the Alfrax is cured, temperature changes should be <40<sup>0</sup>C/h. Also, Alfrax 66 has different initial thermal expansion characteristics than the Monofrax K-3. During Alfrax 66 curing, the thermal expansion is offset by shrinkage of the refractory caused by the water loss. In this refractory installation, the Alfrax 66 was cast behind and above the Monofrax K-3. Therefore, during startup the Monofrax K-3 would expand as the temperature was increased; the Alfrax 66 would tend to retain its initial dimensions. This produces tensile stresses in the Alfrax 66, which could lead to the cracking observed.

Glass samples removed from the cracks near the large glass migration in the north wall and at the base of the riser block resemble glass formulations processed in early melter testing. This supports the conclusion that the Alfrax 66 cracking was the result of the rapid startup and thermal expansion differences between the Monofrax K-3 and the Alfrax 66 refractories. Much of the Alfrax 66 cracking discovered in the LFCM can be prevented in the future by following the recommended curing schedule and by assuring that slip planes are included in the refractory design to permit the Monofrax K-3 to expand during the Alfrax 66 curing period.

### 5.3.3 Zirmul

The Zirmul bricks installed beneath the Monofrax K-3 floor were in excellent condition on removal from the melter. The bricks were covered with a thin layer of glass in the center of the floor, Figure 43, and glass had

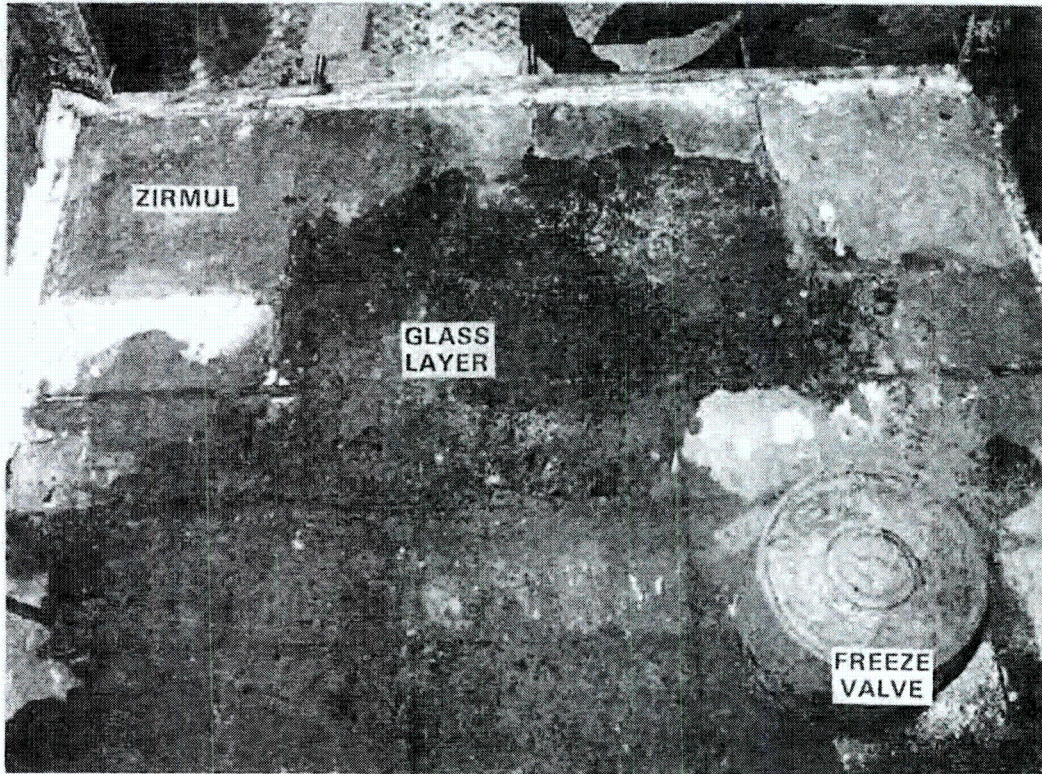


FIGURE 43. Glass Layer on the Zirmul Floor Blocks

penetrated the interbrick joints in this region. Glass was also found in Zirmul cracks near the freeze valve. Visual inspection of the Zirmul revealed no significant interaction between the glass and the refractory. The most severely affected regions were discolored up to 0.5 cm into the bricks. Other than the discoloration, no effects on the Zirmul were detected.

#### 5.4 OVERFLOW DRAIN

The glass discharge was fabricated from Monofrax K-3, Alfrax 66, and a low-density, insulating-type brick. This region of the melter performed satisfactorily during the melter life, but two operational effects were noted during the disassembly.

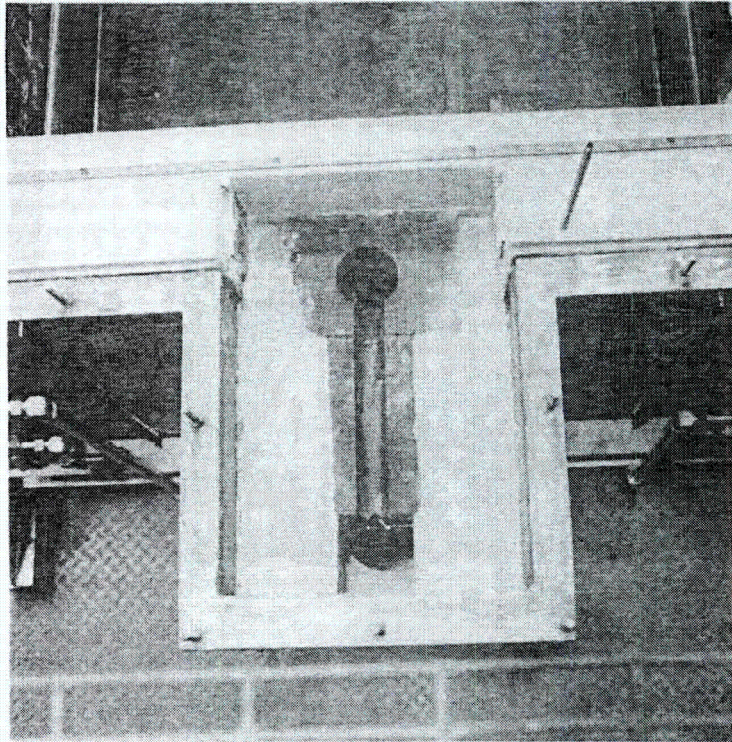
The Monofrax K-3 trough block was found to be broken into two pieces, each roughly one half of the length of the original brick. The channel along the discharge face of the block also appeared to have been fractured during the operating period. This damage may have occurred as the result of thermally shocking the block during rapid overflow section heatup cycles or as the result of mechanical stresses during manual removal of solidified glass. The appearance of the the overflow drain in the new and final states is shown in Figure 44. The damage to the trough block did not affect the operation of the melter.

A more serious concern may be the corrosion of the low density bricks by glass that migrated from the drain. Figure 45 shows the glass covering these bricks. The glass easily penetrated the pores of these bricks and some rounding of the corners is apparent. Use of higher density, more corrosion-resistant bricks may be considered for future designs to prevent loss of structural integrity in this region.

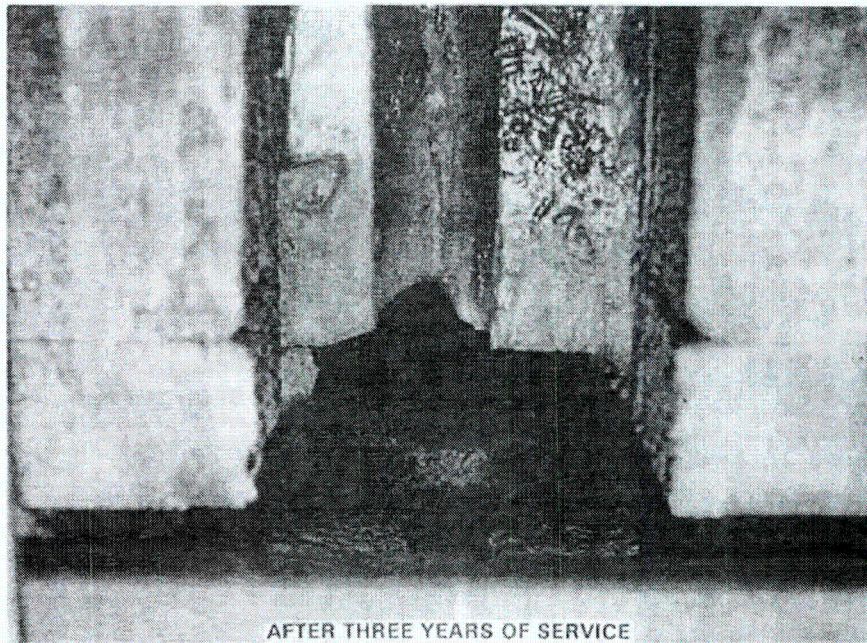
The Inconel 690 pouring tip did not appear to be adversely affected by the three years of melter operation. A detailed examination of the pouring tip is included in Section 7.2.3 of this report.

#### 5.5 ELECTRODES

The primary and secondary electrodes are pictured in Figure 46 (east electrodes) and Figure 47 (west electrodes) after the three years of exposure



OVERFLOW DRAIN AS INSTALLED



AFTER THREE YEARS OF SERVICE

FIGURE 44. Overflow Drain as Installed and After Three Years of Service

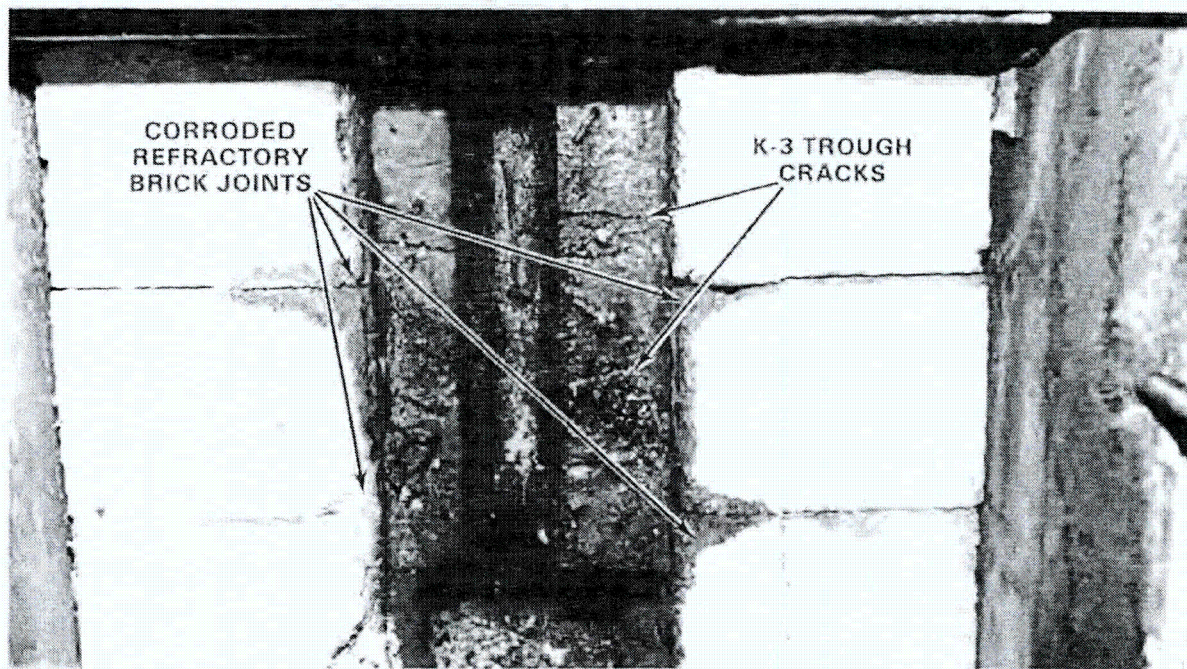


FIGURE 45. Glass Attack of Insulating Bricks in Overflow Drain

to molten glass. Remnants of the spinel crystal layer that covered the electrodes can be seen in these photographs. A similar layer of crystals can be seen adhering to the adjacent refractories. The surface of the primary electrodes appears rough (similar to the surface of sand-blasted cast iron), but the secondary electrodes appear to be in excellent shape. In fact, marks from the original machining process are still visible on the secondary electrodes. The spaces visible at the ends of the electrodes are designed to compensate for the electrode thermal expansion. Minor quantities of glass were found behind the electrodes and between the primary electrode elements.

The difference in the appearance of the primary electrodes and secondary electrodes is due to two factors. The secondary electrodes routinely operated at a lower electrical current output per square centimeter of glass contact face ( $0.34$  to  $0.68$   $A/cm^2$  primary versus  $0.23$  to  $0.62$   $A/cm^2$  secondary). The secondary electrodes also operated at lower temperatures than the primary electrodes (primary operating temperature,  $950$  to  $1100^{\circ}C$ ; secondary operating temperature,  $900$  to  $1000^{\circ}C$ ).

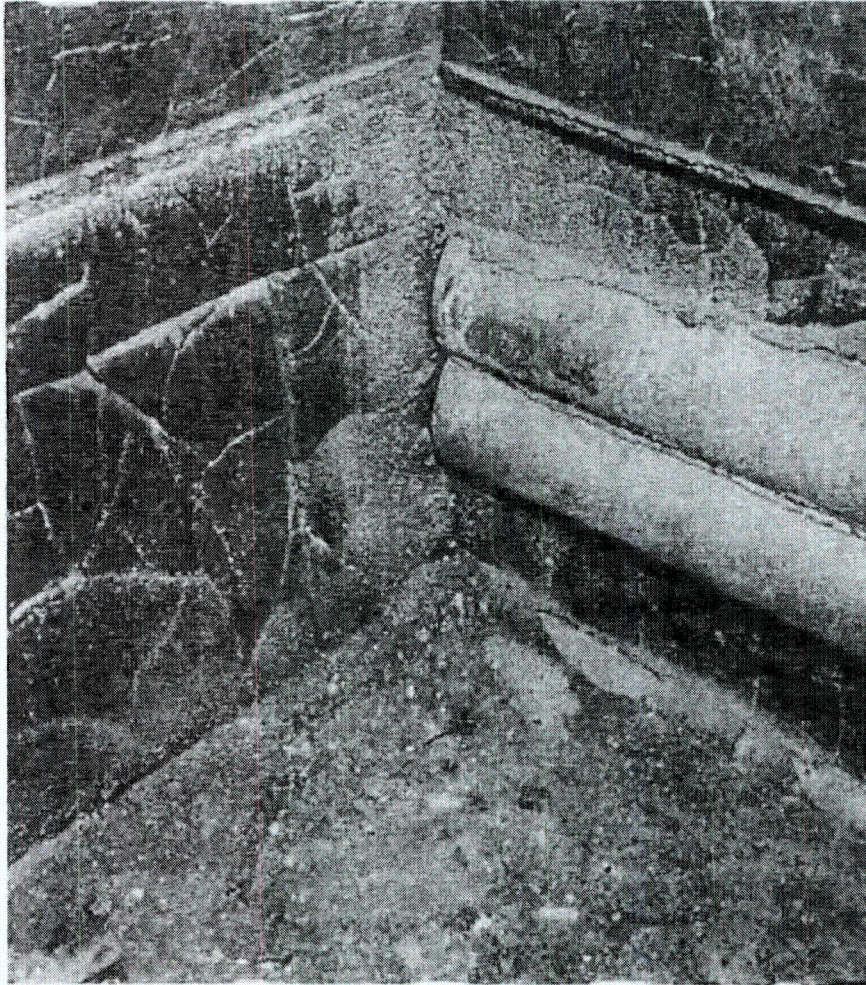


FIGURE 46. East Electrodes Following Operation

The changes in dimensions of the LFCM electrodes are presented in Table 1. Based on this data and assuming that the dimensional changes are only due to material loss (i.e., the effects of high-temperature creep and volume changes related to changing solid phases in the alloy following the extended heat treatment received do not contribute to the measured dimensional changes), the metal loss from the electrodes is 3  $\mu\text{m}/\text{d}$  or less.

Following removal from the melter, the east primary and secondary electrodes were sectioned near the centerline and samples were removed for detailed corrosion examination. The results of these tests are presented in Section 7.2.1 of this document.



FIGURE 47. West Electrodes Following Operation

#### 5.6 IONIC BOOSTER ELECTRODES

The ionic booster electrodes, fabricated from 304L stainless steel, were designed to be continually water cooled. To prevent damage to the melter from water leaking into the melting chamber, the system was designed to stop the coolant flow in the event of an offgas pressure surge in the idling operation mode. On two occasions, an offgas pressure surge (unrelated to an ionic booster coolant leak) tripped the cooling system and went undetected for several days.

Following the second coolant outage, a leak in one of the electrodes developed and air cooling was used for the final three months that the

TABLE 1. Electrode Dimensions

	Length		Width, cm	Height	
	Front, cm	Back, cm		Front, cm	Back, cm
East Primary Top	86.6	86.4	12.5		
East Primary Bottom	85.6	56.4	12.5	20.3	20.2
East Secondary	86.3	86.4	12.7	10.2	10.2
West Primary Top	85.7	86.5	12.5		
West Primary Bottom	85.7	86.4	12.5	20.1	20.2
West Secondary	86.0	86.5	12.7	10.2	10.2
Original Primary Dimensions	86.4	86.4	12.7	20.3	20.3
Original Secondary Dimensions	86.4	86.4	12.7	10.2	10.2

electrodes were installed in the LFCM. The ionic booster electrodes received a total of 25 months exposure to the melting cavity environment.

When the electrodes were removed, the welded zones had become very brittle. The metal bellows used to seal the system and permit vertical electrode motion had developed pin-hole penetrations and had lost all elasticity. Traces of glass were detected in the electrode interior. Apparently the cooling air inside the electrodes blowing past the leakage sites sucked in glass-forming materials during feeding periods. Figure 48 shows the condition of the ionic booster electrodes after removal. Figure 49 is a photograph of the corroded bellows.

Analyses of samples removed from the electrode and bellows showed that the embrittlement of the electrode was caused by sensitization (formation of chromium carbides at the grain boundaries) and that the bellows were corroded by halogens and sulfur compounds. Additional details are presented in Sections 7.2.4 and 7.2.5.

### 5.7 OFFGAS PIPING

The offgas piping connected to the LFCM did not experience significant visible corrosion, and was used for extended periods of time. This piping was generally a stainless steel alloy, either type 304L or 316.

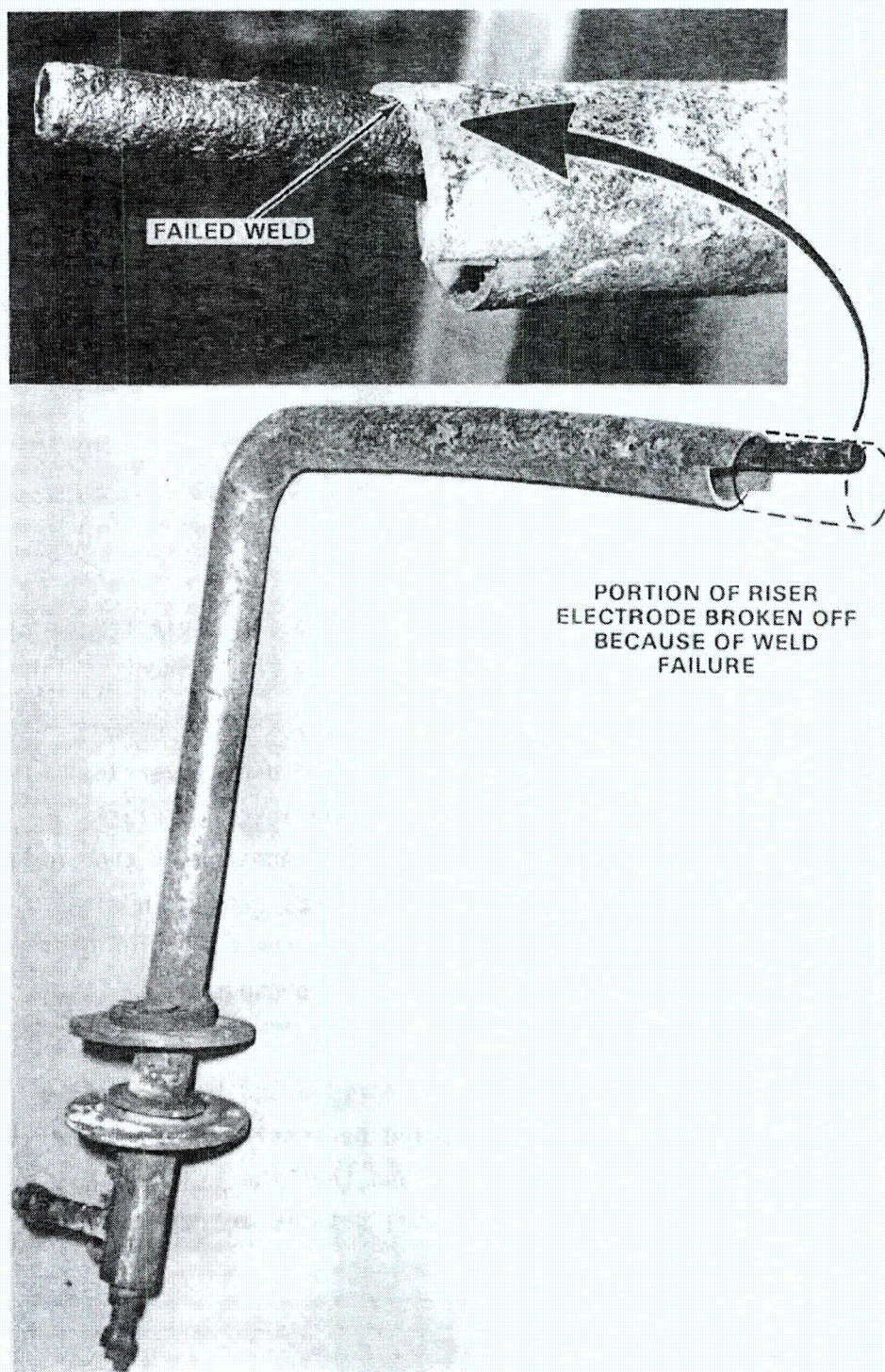


FIGURE 48. Ionic Booster Electrode After Removal from LFCM

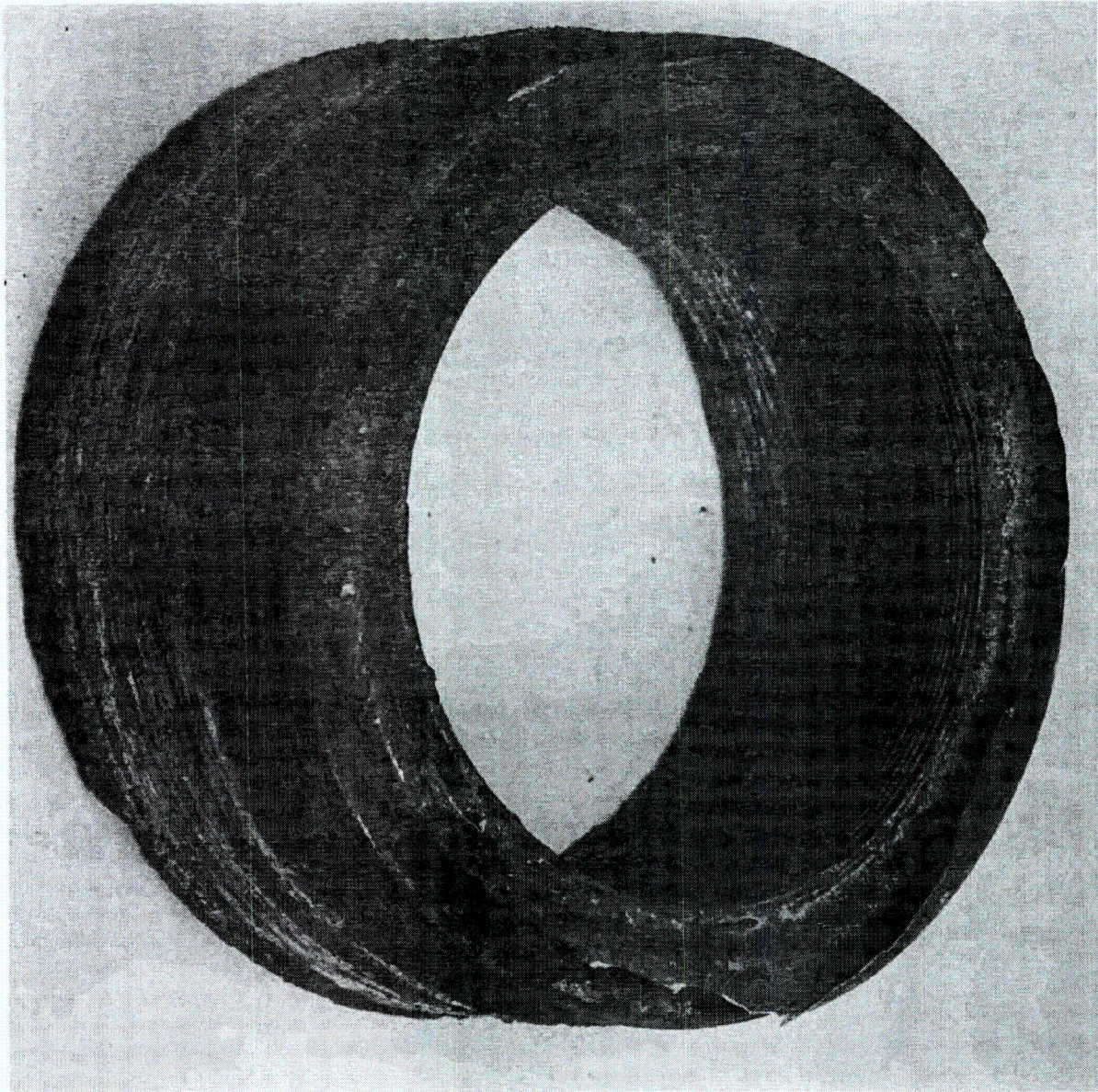


FIGURE 49. Failed Ionic Booster Bellows

Following the shutdown of the LFCM and completion of the methodical disassembly process, the LFCM was reconstructed in the original containment shell. Although this document is intended to summarize the corrosion experience of

the original LFCM, the details of the corrosive attack of the initial offgas jumper between the melter and the offgas system are included because of the rapid failure encountered.

The stainless steel, convoluted piping from which the offgas connecting section immediately adjacent to the melter was fabricated, failed 106 h into the first slurry feeding test. A section of the corroded metal is pictured in Figure 50. This experiment was unique up to that point because the lid heaters were used to increase the slurry feed processing rate. This additional energy input from above the feed resulted in offgas temperatures approaching 600°C. At this temperature the type 204L, stainless steels piping was severely attacked by chlorine and sulfur compounds. The details of the particular corrosion mechanisms are presented in Section 7.2.6.

#### 5.8 FREEZE VALVE

The LFCM freeze valve operated as designed. Following the cessation of the freeze-valve coolant flows, the freeze valve satisfactorily drained the melter. At least 2 cm of slag deposits were above the valve before the draining operation (see Figure 25).

Figure 51 is a photograph of the freeze valve following removal of the refractory. The refractories and slag deposits prevented any damage to the freeze valve during the melter operation, and it was reinstalled in the rebuilt LFCM.

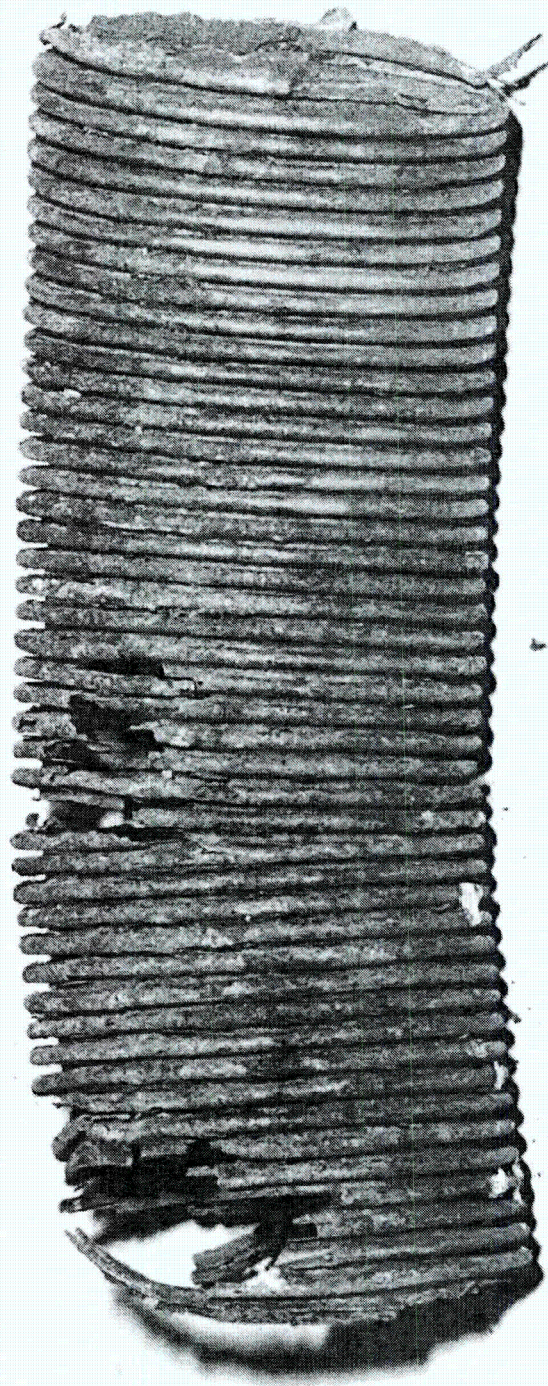


FIGURE 50. Corroded Offgas Piping



FIGURE 51. LFCM Freeze Valve

## 6.0 MELTER STRESS ANALYSIS

An analytical model of a ceramic-lined glass melter was developed to investigate the stress levels possible in refractory designs similar to the LFCM and to predict the effects of the different operating modes on the stress profiles. This model was based on the LFCM refractory design, temperature profiles, and containment box. The modeling was performed with a two-dimensional, finite-element code, ANSYS, with in-plane strain capabilities. The melter simplification required for a two-dimensional model implies that specific planar cuts within the refractory must be selected to investigate the local stress profiles of interest. The two-dimensional model also implies that the modeled structure is long enough in the third dimension to negate end effects, that there is no thermal gradient in the third direction, and that a stress gradient in the third dimension does not occur.

### 6.1 MODEL DESCRIPTION

The cuts (sections) selected for the analytical model were in the north-south direction through the LFCM refractory. This orientation was selected because of the major differences in appearance between the north and south walls after the melter was drained. These cuts meet the model restriction for length in the third direction. However, the changing geometry of the melter in the riser block region, the heating of the upper levels of the riser block from the overflow drain heaters, and the lack of containment shell cooling in the overflow drain region, all give rise to an east-west temperature, and thus stress gradient in these regions. The effects of the temperature and stress gradients in the third dimension are not included in this model.

A possible limitation of a finite-element analysis of the refractory stresses is the inherent linear elasticity assumption of this model. This assumption essentially implies that the modeled material does not fail. Ceramic materials tend to initiate cracks that propagate in a manner characteristic of brittle materials in a moderate to high tensile stress field. Little plastic strain energy is absorbed in the propagation of the crack as

the strain required to fail ceramic matrices is very small. Modeling this type of failure requires a specialized computer routine, very small finite elements, and considerable data on the structural materials being modeled. Generalized codes, such as ANSYS, will not accurately model crack development because the matrix is assumed to be continuous. In actuality, after the development of a crack, the tensile load normal to the crack must be zero and the material is no longer continuous. Also, this type of analysis requires that the refractory characteristics related to fracture failure be well defined. These data are not generally available for refractory ceramics (not available for the Monofrax K-3 and Alfrax 66 in particular) as common design practices do not employ these materials when flexure stress levels are likely to create failures.

Notwithstanding these limitations, a linear-elastic, finite-element model of the refractories will generate results that can be used to assess stress levels within the melter and to determine possible crack initiation sites. The linear-elastic analysis will also indicate the direction of crack propagation once it is initiated. Brittle materials tend to propagate cracks in the direction normal to the orientation of the maximum tensile stress in the material. If relaxation of the stress creating the crack occurs because of the crack propagation, and the direction of the maximum tensile stress changes, the crack will tend to follow the direction normal to the new maximum tensile stress.

Therefore, the constant stress contours generated by the ANSYS model should predict the initial crack direction and the nature of the resulting stress field. Additionally, the ANSYS code does not require the fracture mechanics' characteristics of the refractories. This eliminates the need to assume these values and thereby reduces the potential for modeling error.

Two models, based on the ANSYS code, were used to predict the refractory stress levels in a design similar to the LFCM with various boundary conditions. The initial, simplified model, shown in Figure 52, is based on 15.2-cm Monofrax K-3 walls and floor assuming no Alfrax 66, fiberboard, or containment box. This model was given temperature boundary conditions and allowed to expand

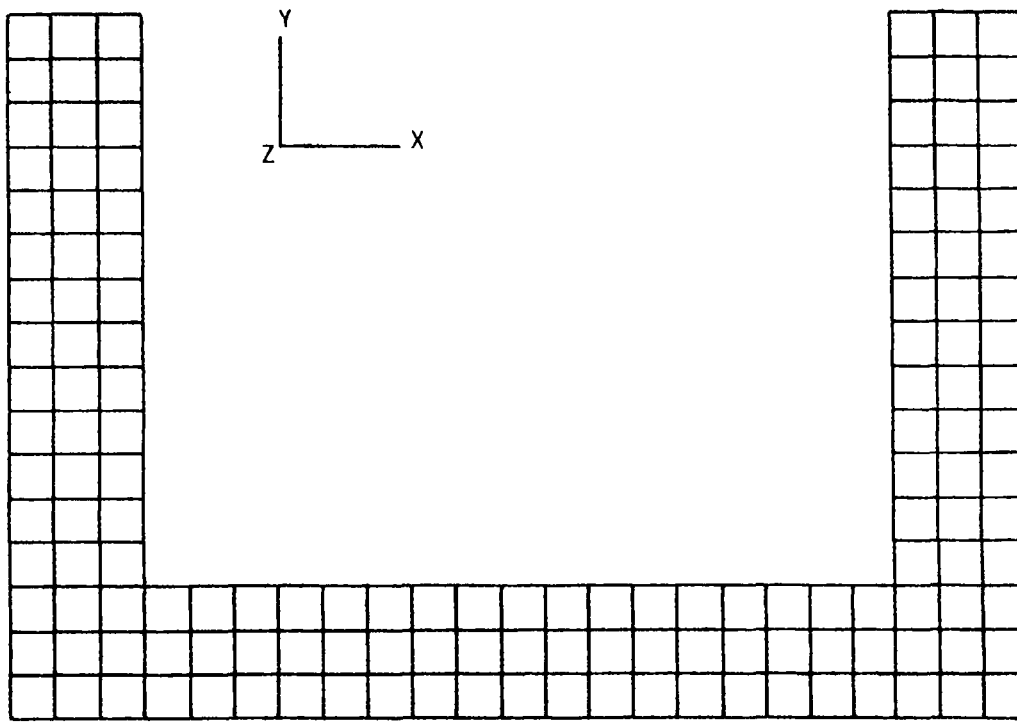


**FIGURE 52.** Simple Model of Melter Used in Preliminary Calculations

freely, but was not permitted translational or rotational motion. With these conditions very low refractory stresses were produced, but the upper corners of the walls were displaced outwards roughly 5 cm. In the next simulation, an additional boundary condition was added which constrained the upper refractory ends from moving. These assumptions produced stresses as high as 345 MPa. The published Monofrax K-3 ultimate compressive strength is 138 MPa (Carborundum Company 1980). The degree of thermal strain allowed in the structure, therefore, will determine the magnitude of the thermal stresses. If the refractory is allowed to expand thermally without restraint, the thermal stresses will be low. Conversely, if the refractory is constrained, the thermal stresses will be high and will generally cause failure of the material.

The second model based on the LFCM refractory design comprises elements representing the Monofrax K-3, Alfrax 66, Zirmul, and the fiberboard. In this

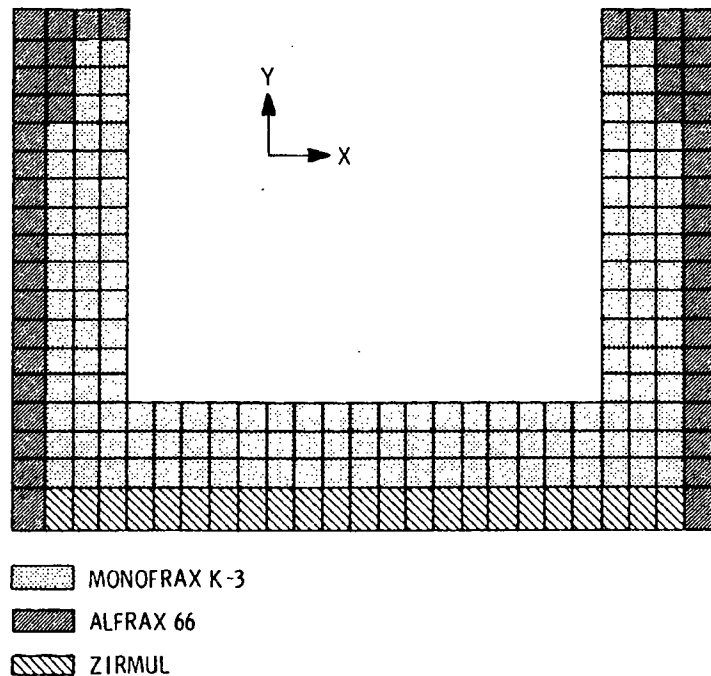
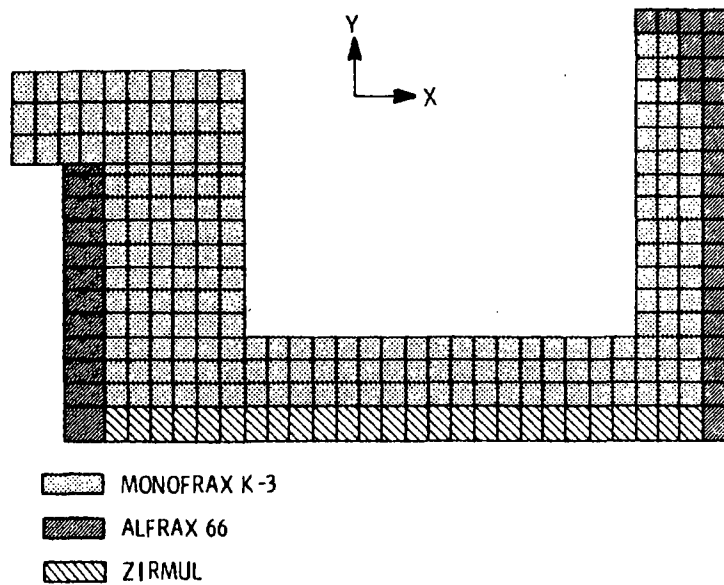


FIGURE 53. Finite-Element Model of Cut Through Melter to East (or West) of Riser Block (Cut #1)

model, three cuts through the melter were analyzed. The modeled refractory planes are depicted in Figures 53 through 55. Figure 53 is to the east or west of the riser block; Figure 54 is cut through the riser block, but to the east or west of the drain riser; and Figure 55 is a plane slicing the refractory through the riser centerline. Between the refractory layers and at the junctions of the blocks, spring or truss elements were employed to model the interaction between refractories or blocks. These trusses have a stiffness that is associated with the contact stiffness at each junction. Each refractory element, therefore, was allowed to transmit a force to the surrounding refractory elements.

Outside the insulating layer of castable Alfrax 66 in the LFCM design, a layer of crushable fiberboard was installed to accommodate thermal expansion of the refractories. This fiberboard was modeled using soft trusses of 1.3-cm length between the outer layer of the refractory and a fixed set of nodes. This fixed set of nodes models the stainless steel containment box.



**FIGURE 54.** Finite-Element Model of Cut Through Melter to East (or West) of Riser Within Riser Block (Cut #2)

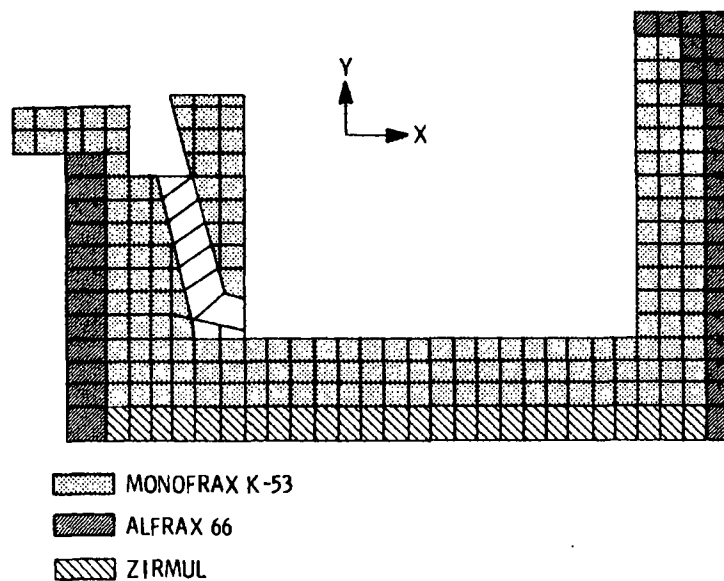


**FIGURE 55.** Finite-Element Model of Cut Through Melter Centerline, Including Riser (Cut #3)

The physical properties of the refractory materials required by this analysis are not readily available from the literature. The elastic constants for Monofrax K-3 (Chan and Nicholson 1978), Zirmul, and Alfrax 66 are listed in Table 2. The elastic properties of Zirmul and Alfrax 66 were estimated by the method suggested by Van Vlack (1964).

## 6.2 ANALYSES RESULTS

The analytical refractory model was subjected to boundary conditions representative of steady-state idling and liquid-feeding operating modes. The third operating mode, calcine feeding, was not simulated because this mode would present temperature profiles somewhere between the idling and liquid-feeding extremes. A discussion of the transient conditions present at liquid-feeding initiation is also presented.

### 6.2.1 Idling Mode

The first two cuts through the refractory were analyzed for temperature boundary conditions representative of idling conditions. The temperature profiles calculated for the model were obtained by performing a steady-state thermal conduction calculation based on an assumed internal face temperature of 1200°C and temperature data from LFCM thermocouples. The predicted temperature profiles are presented in Figures 56 and 57. These calculated thermal patterns were used for temperature conditions for the stress analysis.

The predicted stress contours for the two cuts are shown in Figures 58 through 61. These plots represent the locus of points with constant horizontal or vertical stresses. Tensile stresses are represented by positive numbers, compressive stresses by negative values. For these stress predictions,

TABLE 2. Material Properties of Each Refractory

<u>Material</u>	<u>Young's Modulus, MPa</u>	<u>Poisson's Ratio</u>	<u>Thermal Expansion, cm/cm<sup>0</sup>K</u>	<u>Thermal Conductivity, W/m<sup>0</sup>K</u>
Monofrax K-3	1.4 (10 <sup>6</sup> )	0.4	7.97 (10 <sup>-6</sup> )	2.6 (10 <sup>-8</sup> )
Zirmul	6.9 (10 <sup>5</sup> )	0.4	6.66 (10 <sup>-6</sup> )	1.7 (10 <sup>-8</sup> )
Alfrax 66 Castable	3.4 (10 <sup>5</sup> )	0.4	9.0 (10 <sup>-6</sup> )	2.1 (10 <sup>-8</sup> )

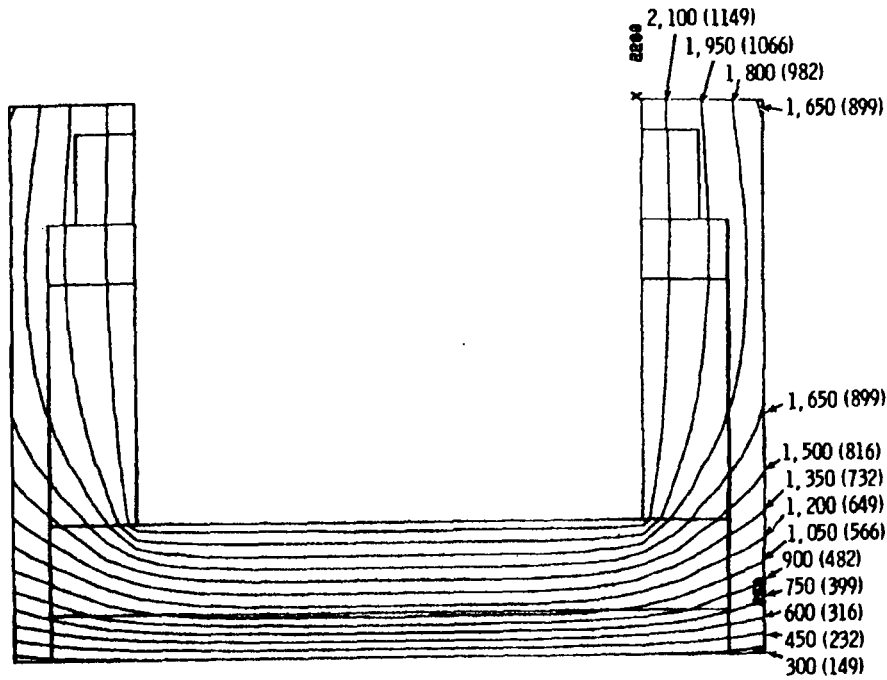


FIGURE 56. Temperature Profiles for Cut #1 Idling-- $^{\circ}$ F ( $^{\circ}$ C)

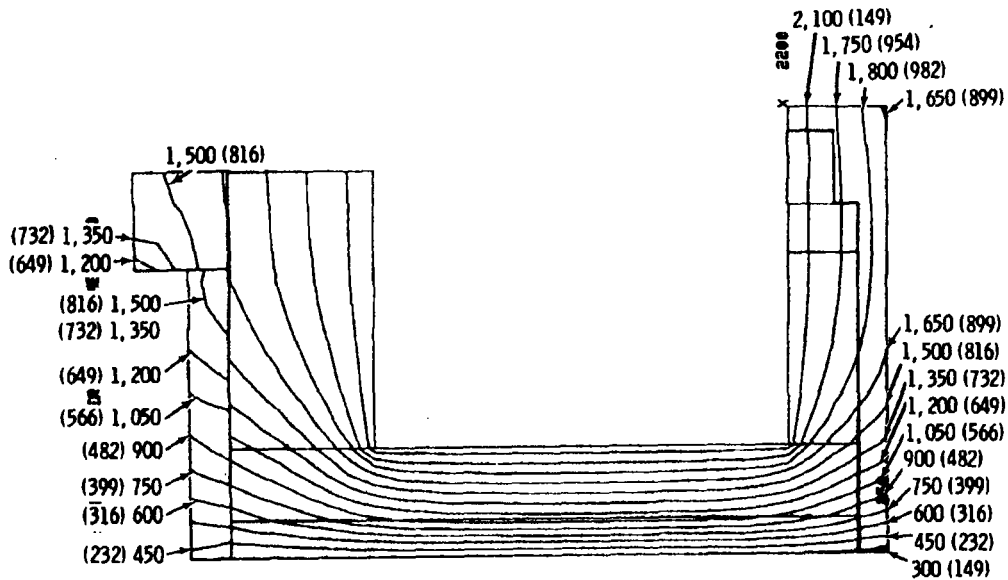


FIGURE 57. Temperature Profiles for Cut #2 Idling-- $^{\circ}$ F ( $^{\circ}$ C)

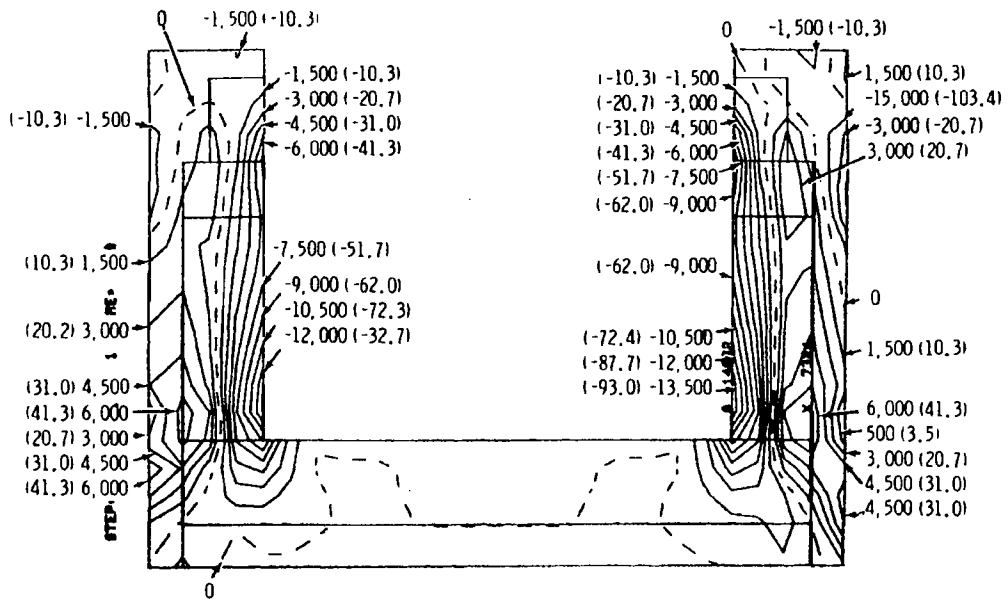


FIGURE 58. Vertical Stress Profiles for Cut #1 Idling

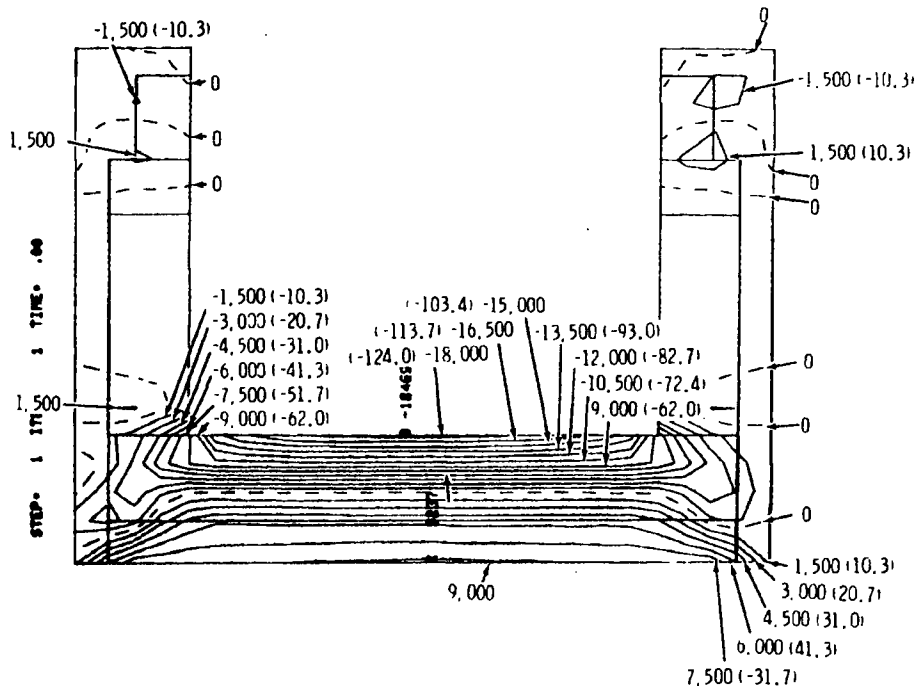


FIGURE 59. Horizontal Stress Profiles for Cut #1 Idling

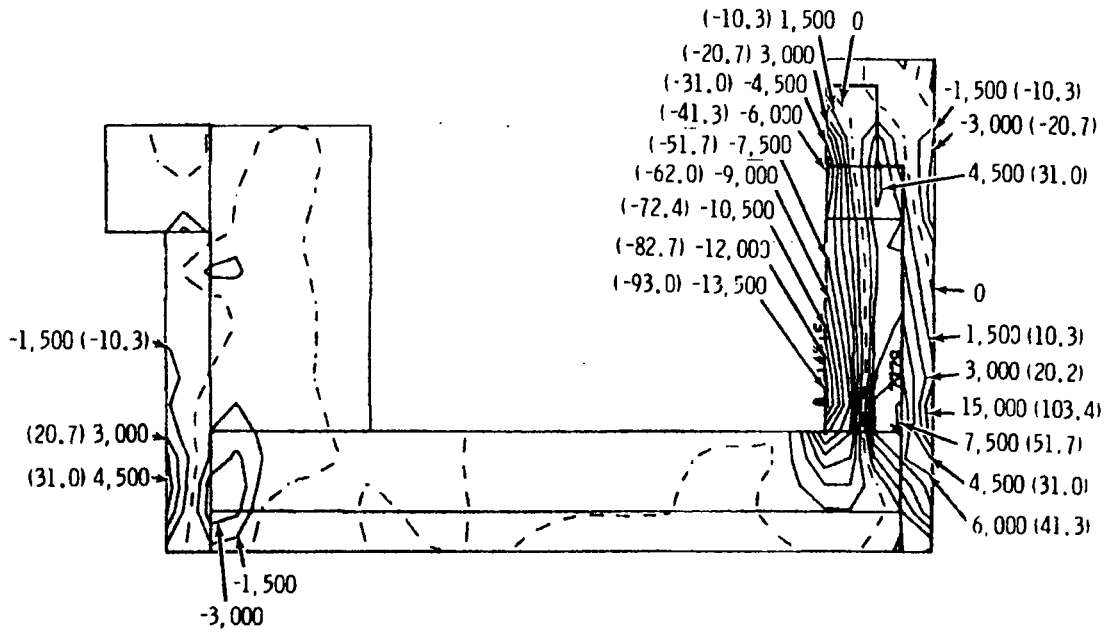


FIGURE 60. Vertical Stress Profiles for Cut #2 Idling

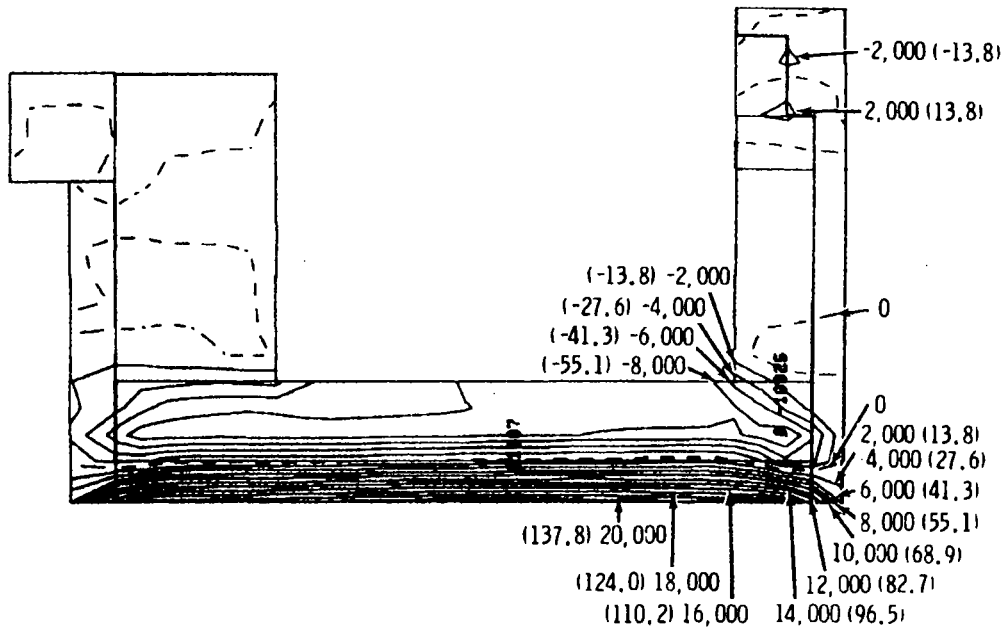


FIGURE 61. Horizontal Stress Profiles for Cut #2 Idling

the walls and floor are constrained from horizontal motion by the representation of the containment box in the model. Vertical growth is not restricted.

Several observations can be made from these predictions. Of special interest are the high compressive stresses at the inside surface of the refractory and the fairly high tensile stresses near the outside of the Monofrax K-3. These stresses are to be expected because of the restraint imposed upon the refractory by the steel jacket. The crushable fiberboard does not provide sufficient allowance at the top of the melter for the walls to freely expand. The compressive stresses predicted do not exceed the 138-MPa rupture strength of the Monofrax K-3, but the tensile stresses at the outer edge of the Monofrax K-3 are as high as 41 MPa. Although the tensile stress is relatively small, ceramic materials are notorious for failure under tension loads, and this stress level may be sufficient to nucleate cracks. The horizontal stress contours of Figure 60 are also relatively high. They are again compressive at the inside surface and tensile at the outside surface. This indicates that the center of the floor attempted to bow upwards but was constrained by the refractory walls.

The north wall of the second cut through the melter displays temperature and stress patterns similar to the first cut. Note, however, that the south wall has fairly low stress levels. The refractory is free to move upward in the model, relieving any thermal stresses in that direction. In the actual melter, the lid contacts the upper surface of this refractory. This interaction was neglected because of the difficulties in accurately modeling the force transmitted at the interface between lid and refractory block.

The effect of restraining the thermal expansion of the riser block on the refractory stress levels is graphically shown in Figure 62. The magnitude of the stresses predicted with this additional boundary condition are nearly twice the rupture strength of Monofrax K-3 and reach 551 MPa in the Zirmul flooring. Neither of these two boundary conditions (total or no restraint from vertical expansion) are likely to represent the actual conditions present in a melter of the LFCM design. The actual stress level is probably a transient function

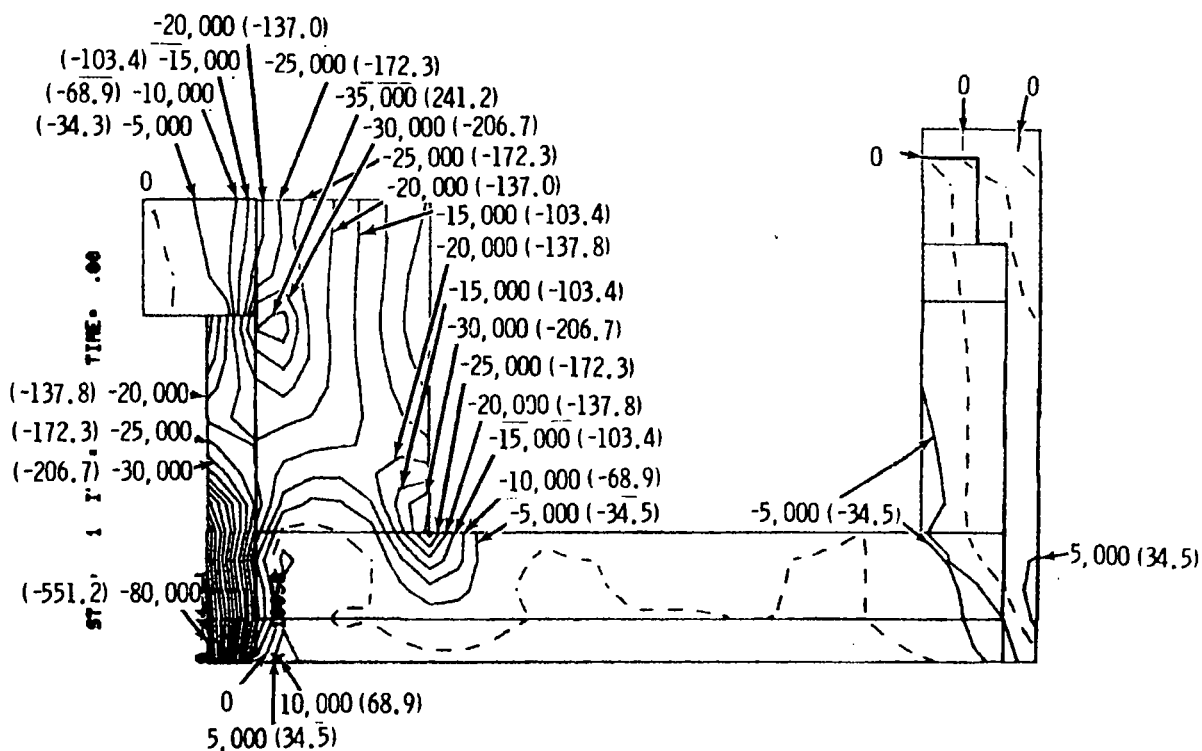


FIGURE 62. Vertical Stress Profiles for Cut #2 Idling with Upper Portion of Riser Block Constrained

of the lid and refractory temperatures. Clearly, the magnitude of the refractory stresses is directly related to the degree of restraint from free thermal expansion.

### 6.2.2 Steady-State Liquid-Feeding Mode

The liquid-feeding analysis was based on the temperature assumptions of 1200°C below 48 cm (nominal glass level) and 149°C above the 48-cm level. These temperature conditions are due to the presence of the cold cap on the glass surface and are the values assumed for earlier LFCM numerical modeling efforts (Hjelm and Donovan 1979). As in the idling simulations, the refractory walls are restrained from north-south expansion, but no vertical expansion constraint was included.

The effect of the change in temperature boundary conditions from the idling mode is readily apparent in Figures 63 through 65. The constant stress contours for this combination of conditions are plotted in Figures 66 through 71.

The thermal stress output by the model for the first two cuts are not significantly different from those in the idling mode. The thermal strains, however, are significantly different. These quantities, unfortunately, are not output by ANSYS, but a short analysis of the thermal strains during the transition to the liquid-feeding mode is presented in Section 6.2.3.

The vertical stress profile predicted in the analysis model for Cut #3 through the riser is of particular interest. The section of Monofrax K-3 that appears to be separated from the rest of the structure is actually tied to the melter through a series of trusses (see Figure 55). The rigidity of these trusses is related to the stiffness of the Monofrax K-3 that surrounds the riser channel. This is the best modeling technique to simulate the modeled melter geometry and stiffness with a two dimensional model. The high compressive stresses on the inside surface of both sides of the riser channel and the tensile stresses on the glass-contact surface of the riser block indicate that the inside portion of the riser block is attempting to bow toward the center of the melter at the top (to the right in Figure 70), but is restrained by the surrounding refractory. This stress pattern, assumably, is created because the surface of the riser is at glass temperature ( $\sim 1200^{\circ}\text{C}$ ), whereas all but the lower tip of the discontinuous refractory section is at  $149^{\circ}\text{C}$ . This is another possible source of fracture in the inside surface of the Monofrax K-3.

### 6.2.3 Transition to Liquid-Feeding Mode

Performing a transient, finite-element analysis of a refractory model based on the LFCM design was not within the scope of this study. Analytical modeling of these effects requires an iterative solution for each of the elements and thus was prohibitively expensive. Along with the reduction of the surface refractory temperature, the major effect of the cold cap is the establishment the local heat flux from the refractory. This heat flux is a

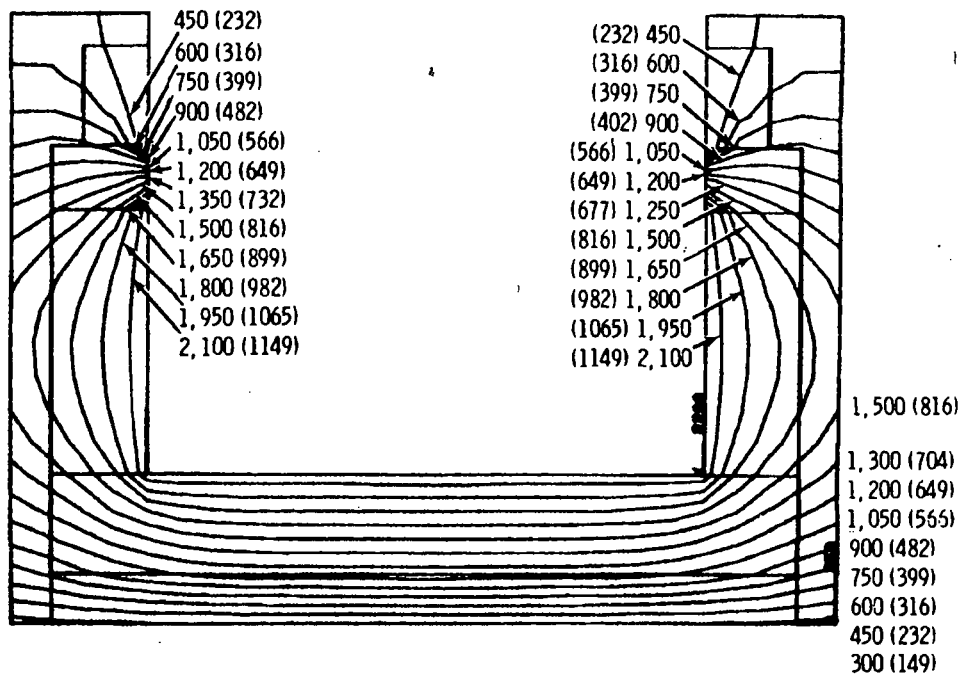


FIGURE 63. Temperature Profiles for Cut #1 Liquid Feed--OF (°C)

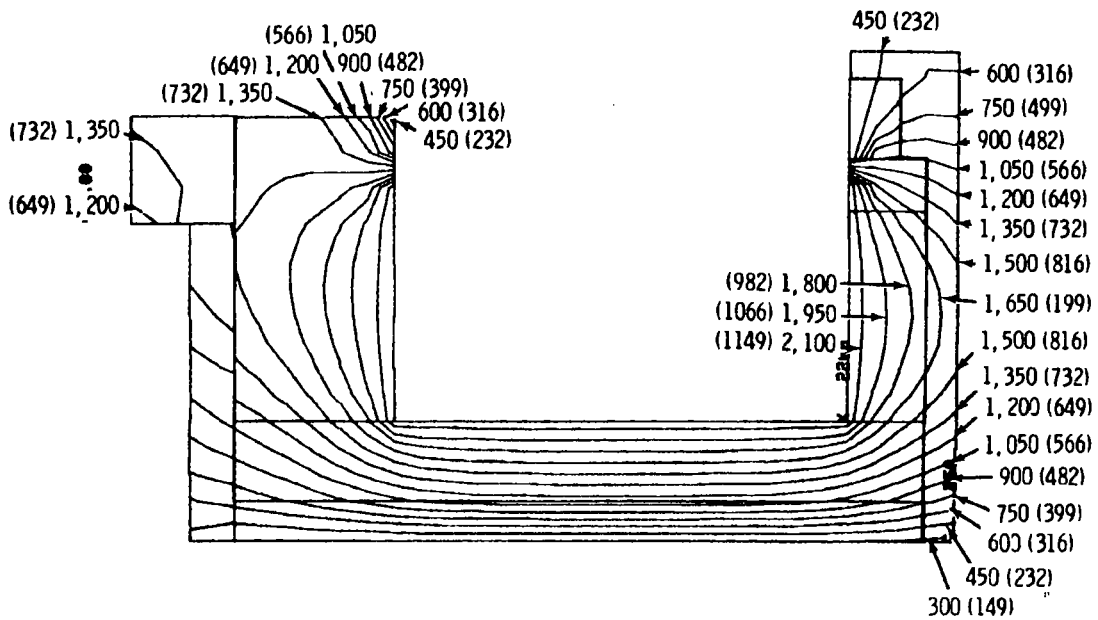


FIGURE 64. Temperature Profiles for Cut #2 Liquid Feed--of (°C)





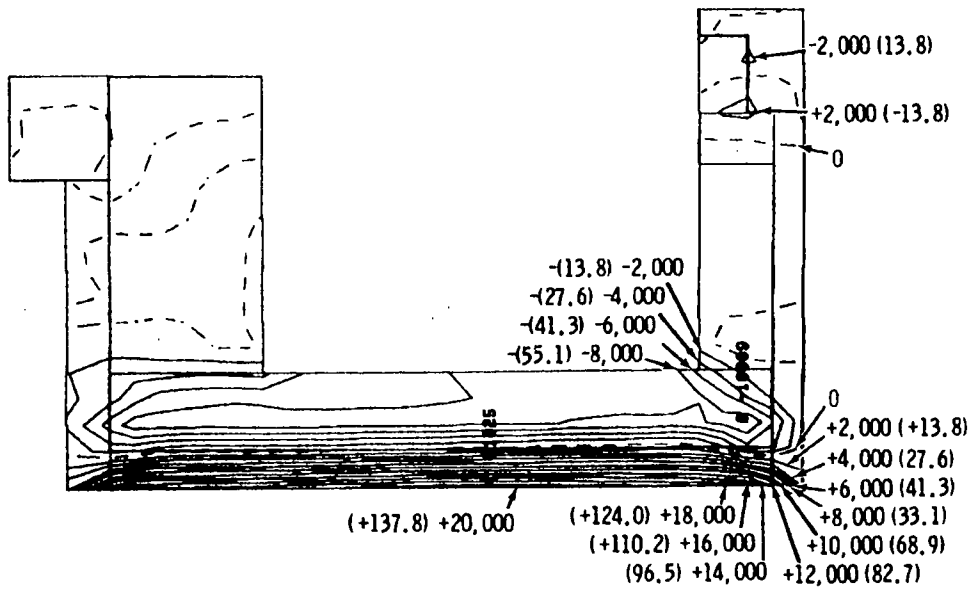


FIGURE 69. Horizontal Stress Profiles for Cut #2 Liquid Feed

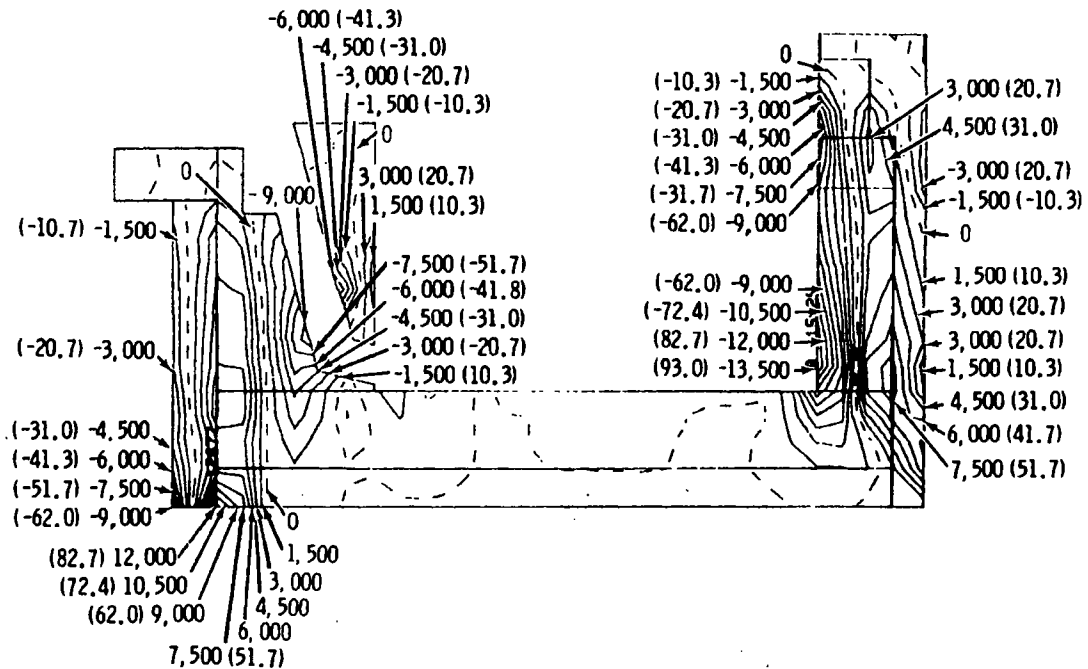


FIGURE 70. Vertical Stress Profiles for Cut #3 Liquid Feed

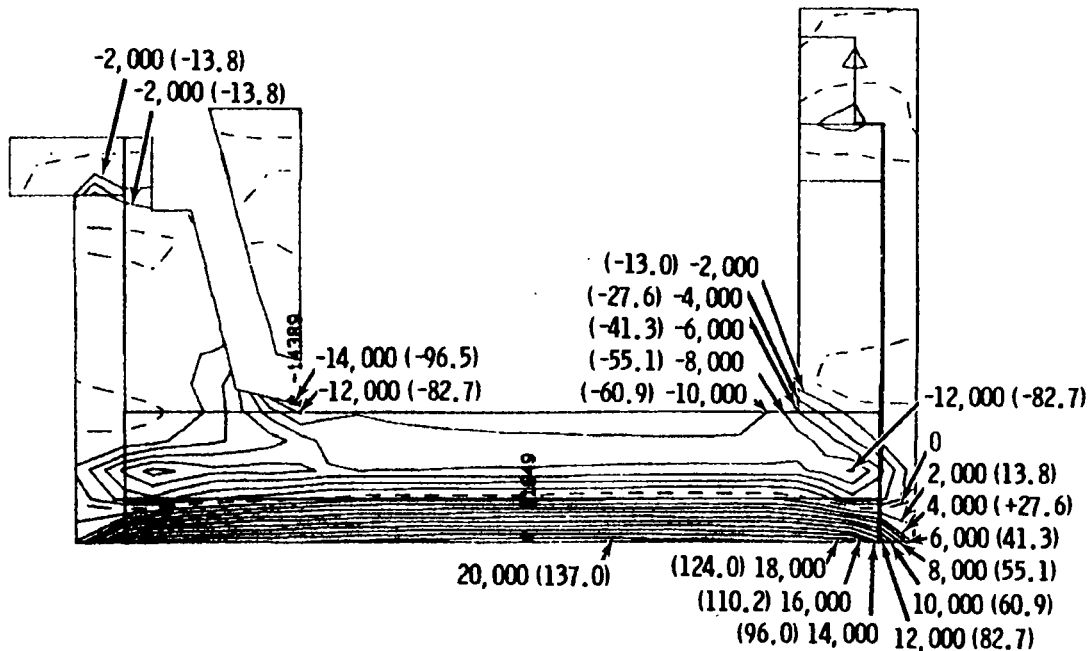


FIGURE 71. Horizontal Stress Profiles for Cut #3 Liquid Feed

function of the cold cap depth, the vaporation rate of the refractory surface, the refractory/cold cap thermal contact resistance, the cold cap thermal conductivity, and the porosity of the cold cap. Currently, these cold cap properties are not well defined. However, simplified calculations were performed to predict the probable upper limit of the transient thermal stress and strains.

When a hot material is cooled rapidly from its outside surface, the outside surface will attempt to shrink. The hot interior resists this shrinkage and surface tensile stresses are created, which can initiate cracks. For example, if a heated marble is plunged into ice water, cracks form at the surface of the marble as the surface shrinks against the hot interior. This effect is the most probable source of cracking in the Monofrax K-3 at the level of the cold cap.

Calculation of the surface tensile-stress upper limit is fairly straight forward. The maximum stress, caused by thermal loading of a member constrained from thermal expansion or contraction can be calculated by:

$$\sigma = E (\alpha) \Delta T$$

where

$\sigma$  = thermal stress

$\alpha$  = thermal expansion coefficient

E = Young's modulus

$\Delta T$  = difference in temperature between the cool outside and hot inside of the refractory.

The thermal stress can be calculated using this equation if a temperature gradient into the refractory is assumed. In this case, the solution assumes an infinite solid initially at 1200°C and an instantaneously applied surface temperature boundary condition of 150°C. Using a one-dimensional, heat-transfer solution, the temperature gradient 5 cm into the refractory is calculated, as well as the thermal stress developed between the surface and this depth. The results are presented in Table 3.

The thermal stress calculations indicate that a sudden temperature change of as little as 115°C exceeds the rupture strength of the Monofrax K-3. This demonstrates the necessity of slow temperature changes within the refractory to prevent excessive thermal-shock tensile stresses.

Another calculation producing similar results is the thermal strain in the Monofrax K-3 created by changing temperatures. The thermal strain is calculated by:

$$\begin{aligned} E &= \alpha (\Delta T) && (E = \text{thermal strain}) \\ &= (7.92 \text{ cm}/^\circ\text{C}) (1056^\circ\text{C}) \\ &= 0.84\% \text{ strain} \end{aligned}$$

In contrast, the strain induced in a ceramic at failure in a standard compression test is defined as:

$$\begin{aligned} E (\text{at failure}) &= \frac{\text{ultimate stress}}{E} && E = \text{Young's modulus} \\ &= 0.1\% \text{ strain} \end{aligned}$$

TABLE 3. Temperatures and Upper Bound Thermal Stresses at Varying Times at a 5 cm Depth into the Refractory

<u>t (minutes)</u>	<u>T (°C)</u>	<u>(MPa)</u>
0	1204	1152
0.25	1089	1026
0.5	1029	960
0.75	970	896
1	914	836
5	263	146
10	159	11

This quantity is significantly smaller than the strain the refractory undergoes in the transition from idling to liquid feeding. This does not mean that heating or cooling the ceramic will cause it to fail. A rapid change in temperature will, however, cause a rapid strain rate. Ceramic materials are inherently susceptible to fracture at high strain rates. Thus, the high strain rate in the transition from idling to liquid feeding is the probable source of the fractures and perhaps of the spalling of the Monofrax K-3 seen in the LFCM when it was disassembled.

### 6.3 MELTER LID

Cracks were discovered in each of the four corners of the melter lid following removal from the LFCM. The positions of these cracks are shown in Figure 72. The lid was fabricated from 0.5 cm Inconel 601 plate with 2.5-cm by 5-cm-type 304L stainless steel stiffeners welded to the exterior to increase the materials resistance to bending moments. These stiffeners (strongbacks) run along all four sides of the vertical box portion of the lid and extend to the edges of the lid. The long-side strongbacks are continuous bars, but the shorter side strongbacks are welded to the long stiffeners in sections. It is at these welds that the melter lid developed cracks.

The failures were the result of differential thermal expansion and excessive thermal stresses in the stiffening members. Because the melter lid was

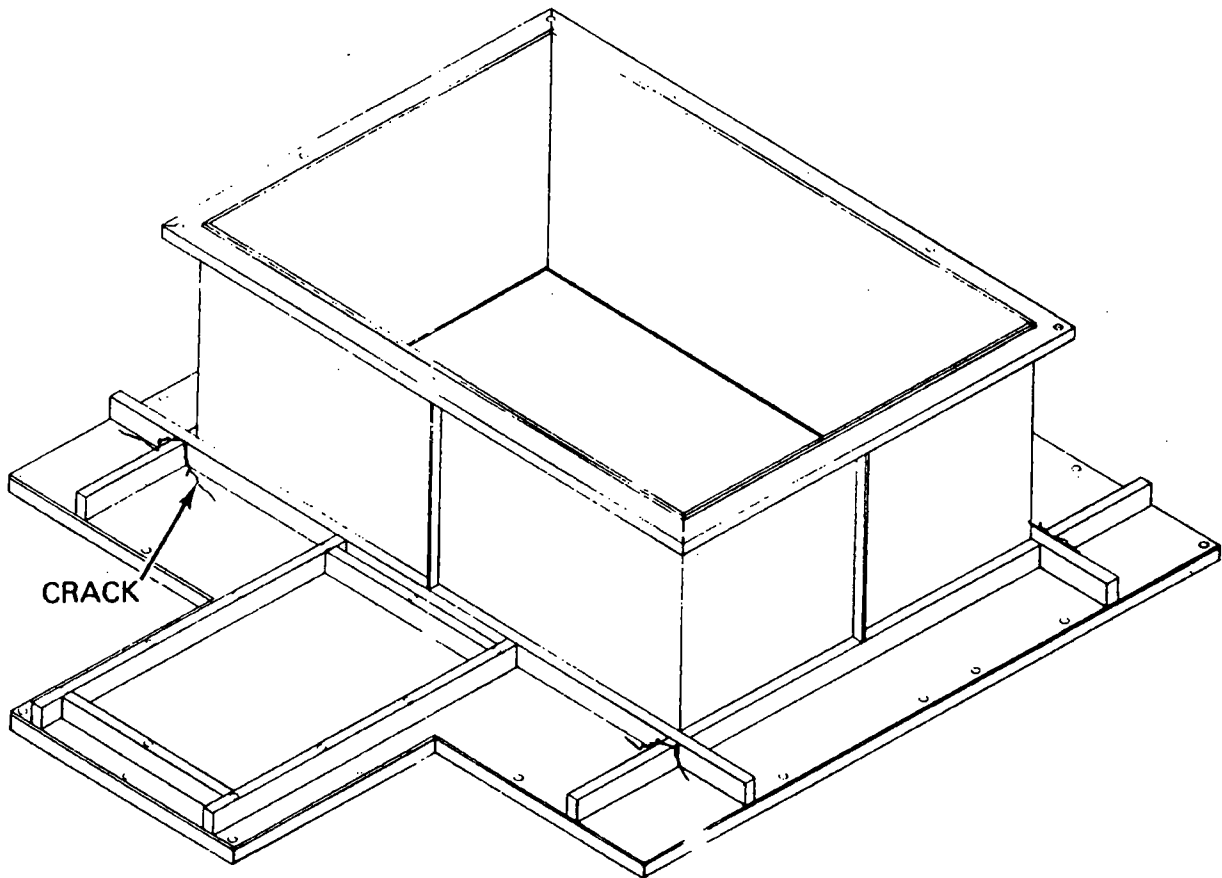


FIGURE 72. Melter Lid Indicating Position of Strongback Weld Cracks

externally insulated, the lid temperature would approach the glass temperature during idling conditions. Assuming that the stainless steel strongback is at approximately the same temperature as the Inconel plate, the total length change required in the short-side strongback for it to be stress-free can be calculated as follows:

$$\begin{aligned}\Delta L &= L\alpha\Delta T \\ &= 0.72 \text{ in.}\end{aligned}$$

where

$\Delta L$  = length change due to temperature increase

$L$  = length of heated portion of strongback = 91.4 cm

$\alpha$  = thermal expansion coefficient of 304 stainless =  $18 \times 10^{-6}/\text{cm}/\text{cm}^{\circ}\text{C}$   
T = temperature change from room temperature to  $1094^{\circ}\text{C}$ .

The strongback obviously cannot freely expand as it is constrained by the Inconel vertical plate (which has a lower expansion coefficient), and by the outside walls of the melter. These walls are held at a much lower temperature than the lid by the water-cooling jackets. Compressive stresses will, therefore, develop in the strongbacks during idling periods. Assuming that 75% of the thermal expansion can be accommodated by the structure, the magnitude of the compression stress in the strongback can be estimated as follows:

$$\sigma = E \alpha T$$
$$\cong 1034 \text{ MPa}$$

The magnitude of this compressive stress indicates that some active plastic flow must occur in the strongback. As metals are heated, they tend to be able to accommodate more of this type of plasticity and also to creep rapidly. Essentially, this strongback will deform plastically and creep to relieve the compression stress. When the melter is placed in the liquid-fed mode and a cold cap develops, the lid cools to roughly  $150^{\circ}\text{C}$ . The strongback will tend to contract as it has already relieved the high compression stresses by creep and deformation. Therefore, tensile stresses will be developed in the strongback of the same order of magnitude as the original compressive stresses. These tensile stresses will produce the weld failures observed in the short-side strongback.

As Inconel 601 has a lower thermal expansion coefficient than type 304L stainless steel, welds between these materials will result in a similar situation as the strongback problem just discussed. During heating to idling temperature, the Inconel will expand less than the stainless steel and will develop tensile stresses (or compression stresses in the steel). The load transfer between the Inconel plate and the stainless steel must occur at the weld joint along the strongback. As such, this weld joint is also suspect and could fail in a melter lid.

The gross deformation and warping of the lid was due to thermal, plastic, and high-temperature creep-related deformations and residual stresses, as discussed above.

## 7.0 MELTER CORROSION INVESTIGATION

Samples from many of the melter construction materials were analyzed in the laboratory. The observations of melter material and the dismantling and structural analyses were correlated to enable an analyses of the construction material condition, which is discussed in this section. The melter components that were examined in detail include: the Monofrax K-3 glass-contact refractory, the castable Alfrax 66 refractory, the power electrodes, the riser plate (a piece of Inconel 690 installed in the Alfrax 66 layer above the riser block for structural support), the pouring tip, the ionic booster electrodes and flexible bellows, and a section of offgas ducting.

### 7.1 REFRACTORY CORROSION

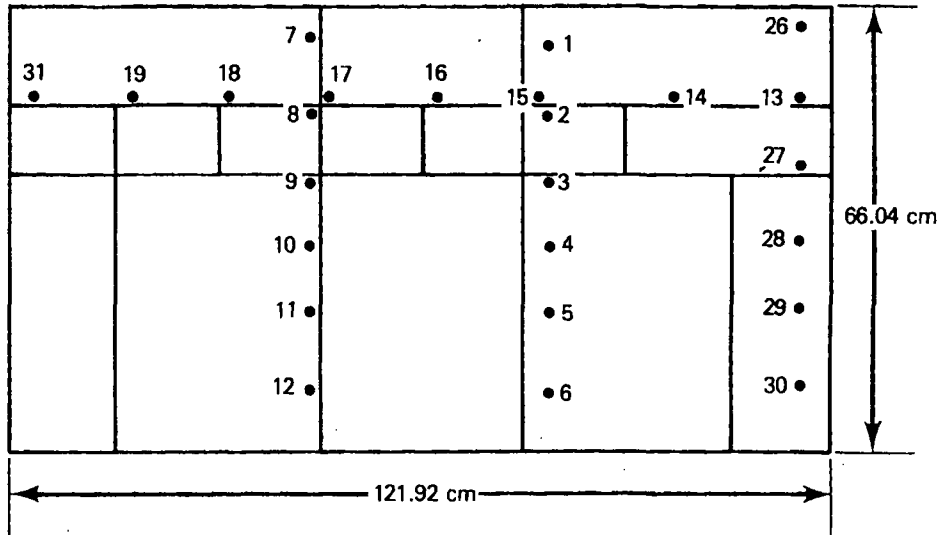
The Monofrax K-3 installed in the floor was apparently well protected from glass corrosion by the layers of precipitates that formed during the operating period, since no decrease in the Monofrax K-3 floor brick thickness was observed. The Zirmul bricks were covered with a thin layer of glass in the center of the floor and glass penetrated the joints between the Zirmul bricks. Glass also penetrated into cracks found in the Zirmul near the freeze drain. Visual examination of the Zirmul revealed no interaction between the glass and the Zirmul refractory in general, but did show discoloration of the bricks to a depth up to 0.5 cm. Other than the discoloration, no adverse effects were observed in the Zirmul. Thus, the refractory corrosion investigation emphasized determining the mechanisms that caused more severe degradation of the other refractory components.

#### 7.1.1 Monofrax K-3 Wall

A series of core samples were removed from the refractory walls to study the effects of the three-year operating period on the Monofrax K-3. The core-sampling locations are shown in Figure 73.

Monofrax K-3 is a fusion-cast refractory composed primarily of  $Al_2O_3$  and  $Cr_2O_3$ . The fused refractory is cast into the desired shape and cooled into blocks with relatively dense outer edges and porous interiors containing

NORTH WALL



LOCATION OF CORE DRILLING SAMPLES

WEST WALL

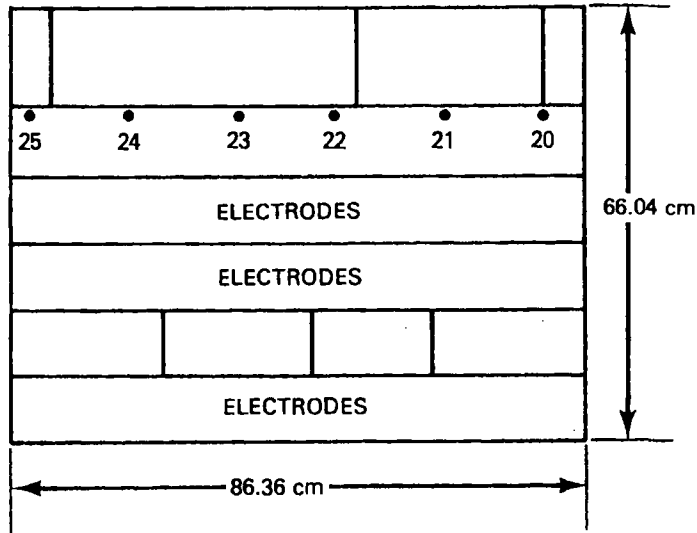


FIGURE 73. Locations of Core Samples Removed from Glass Contact Walls

shrinkage voids. The cooled refractory is a solid solution of two phases. These phases are visible in Figure 74. The light-gray phase is primarily composed of alumina ( $Al_2O_3$ ) with chromium oxide. The darker-gray phase is

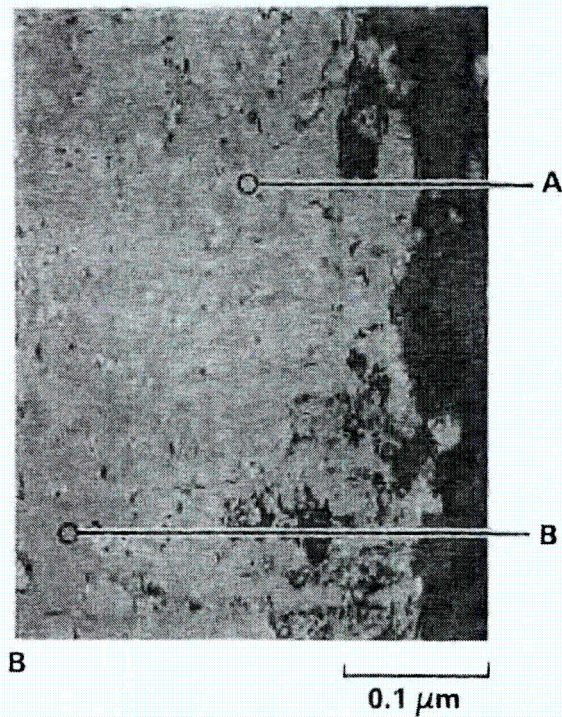


FIGURE 74. Monofrax K-3 Microstructure

rich in  $\text{Cr}_2\text{O}_3$  with oxides of Fe, Al, and Mg. The compositions of these phases are presented in Table 4.

In service both phases are attacked by the glass; however, the high-chromia phase appears to be more severely affected. This conclusion is based on two observations common to each of the core samples investigated. First, at the refractory-glass interface, the glass-contact face is composed primarily of the high-alumina (dark-gray) phase. In several cases, this high-alumina phase retains sharp definition at the original phase boundaries. The chromia phase appears rounded where it contacts the glass, indicating dissolution. These two observations are shown in Figure 75. The preferential attack of the chromia phase is also indicated by the compositional changes of the glass in refractory cracks, such as those shown in Figures 76 and 77. The mole percentages of the glassy-phase constituents at the positions indicated in the figures are listed in Table 5. From the glass-phase compositional data, the increase in Al content is clear. Also apparent is the nearly universal absence of Cr

TABLE 4. Composition of Monofrax K-3 Microstructure Phases

Element	Concentration, Mole%	
	Phase A (Light Gray)	Phase B (Dark Gray)
Na	0 to 2	0 to 1
Mg	0 to 11	0 to 5
Al	19 to 23	26 to 36
Si	0 to 1	0
Ti	0	0 to 8
Cr	10 to 21	0 to 10
Mn	0	0 to 1
Fe	2 to 5	0 to 3
Zn	0 to 1	0
O	49 to 59	55 to 56

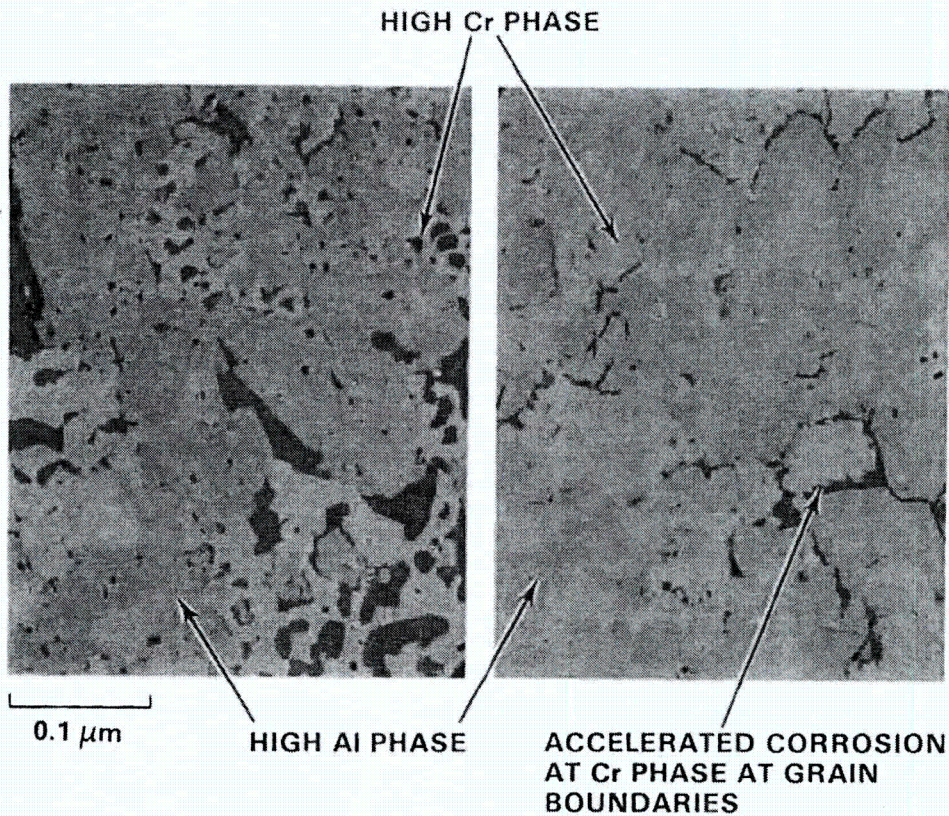


FIGURE 75. Corrosion of Monofrax K-3 High-Chromia Phase

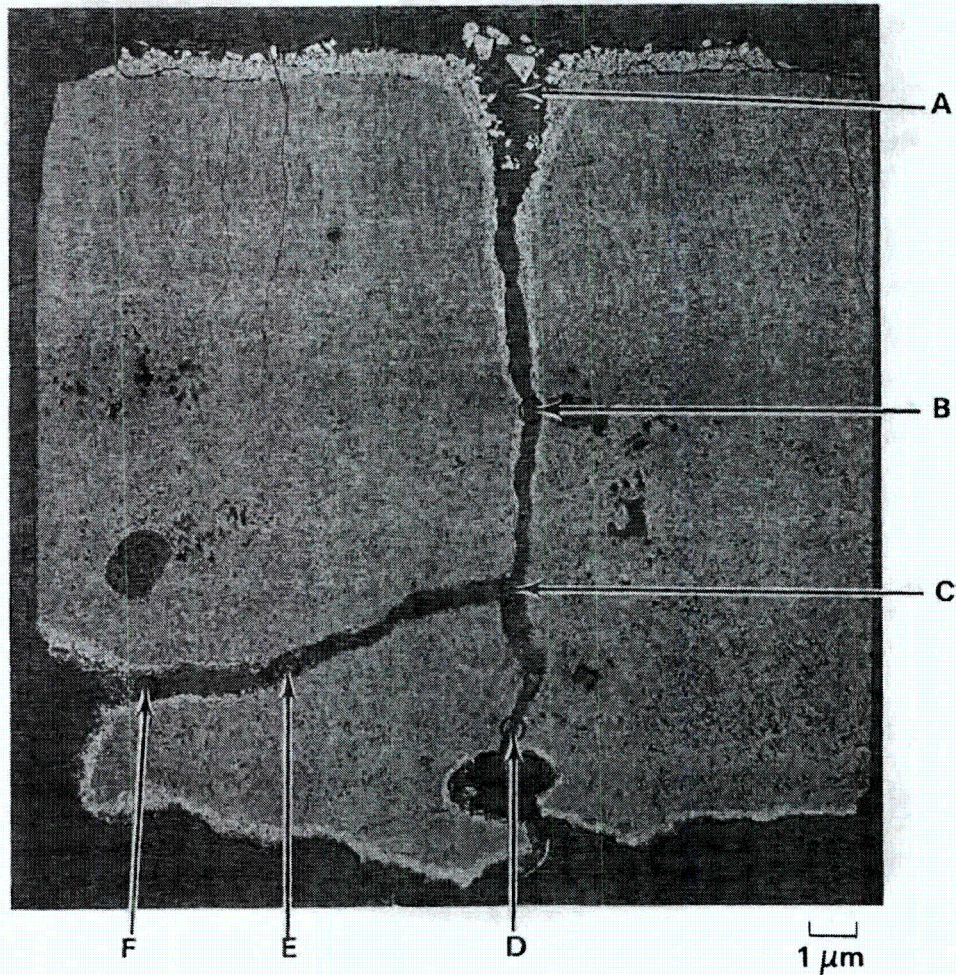


FIGURE 76. Glass-Filled Crack in Monofrax K-3

and Mg, as well as the decrease of Fe present in the glass with increasing distance into the refractory. The facts that the trace components of the high-chromium phase are not present in the glass, and that the alumina concentration of the interior glass phases is relatively high indicate that the chromia and the trace species are forming the crystals visible at the refractory/glass reaction zone. This was supported by microprobe analysis.

The preferential attack of the chromia phase also accounts for several other phenomena associated with the crystalline phase present at the

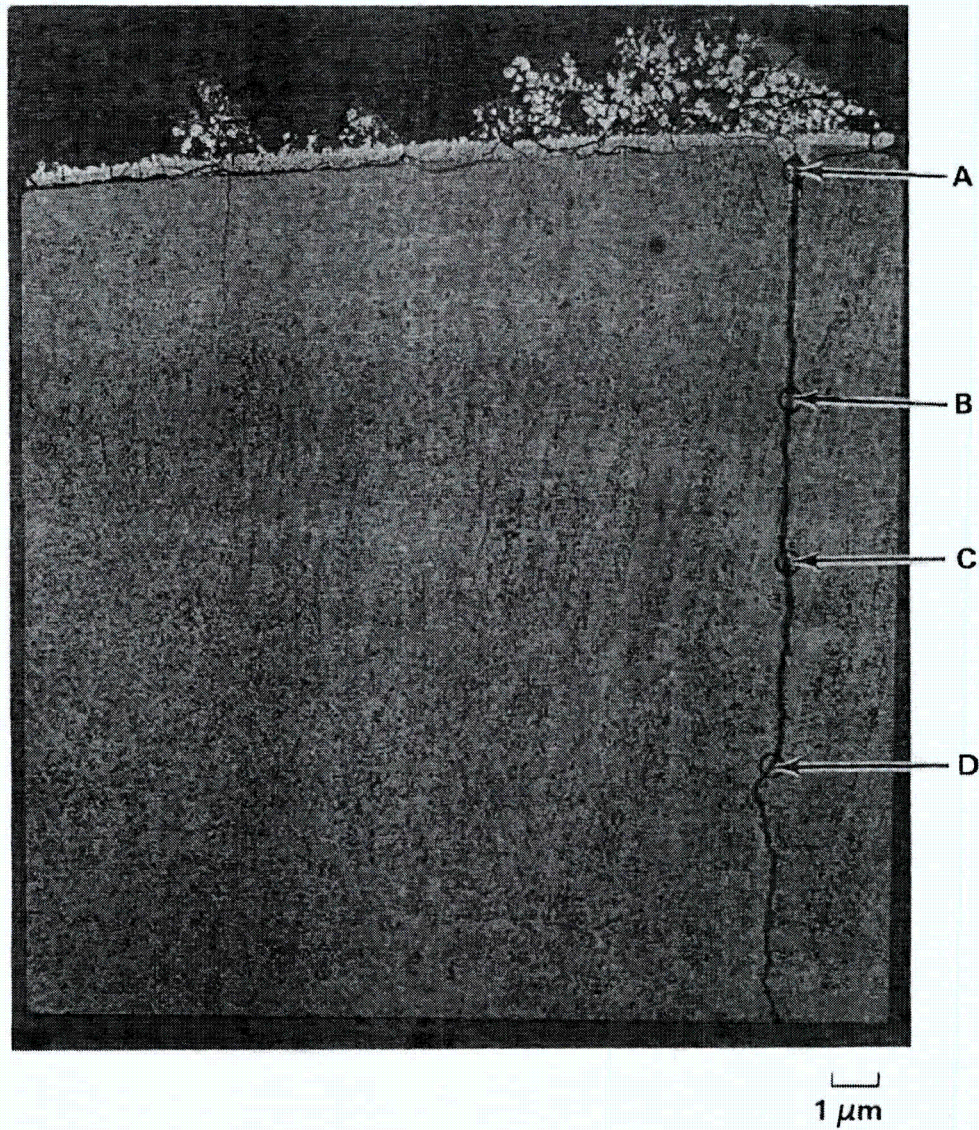


FIGURE 77. Glass-Filled Crack in Monofrax K-3

refractory surfaces. Figures 78 and 79 show typical examples of the crystals growing on the glass-contact faces. The composition of these precipitates and the glass phases present in this layer are shown in Table 6. As with the refractory cracks, the alumina content of the glass phase increases with distance from the bulk glass. Also, the crystals nearest the refractory are primarily  $\text{Cr}_2\text{O}_3$  and progress to a Ni-Fe-Cr spinel across the layer. The Ni-Fe-Cr gradients across this crystalline boundary are clearly displayed in

TABLE 5. Composition of Glass Phases Identified in Figures 76 and 77

Element	Mole%									
	Phase--Figure 76						Phase--Figure 77			
	A	B	C	D	E	F	A	B	C	D
Na	13.6	13.7	13.3	13.0	14.1	13.2	14.0	16.9	16.8	16.1
Mg	0	0	0	0	0	0	0	0	0	0
Al	2.7	3.2	9.4	6.4	4.1	4.4	4.6	16.4	14.8	16.3
Si	17.4	17.3	15.5	16.1	16.9	16.5	17.2	16.3	13.2	17.0
S	0.1	0.3	0	0	0.2	0.1	0.2	0	0.3	0.1
K	0.1	0.1	0.1	0.1	0.1	0.1	0	0.1	0	0.3
Ca	2.1	2.0	0.8	1.6	1.0	1.7	1.7	0.4	2.5	0.4
Ti	0	0	0.1	0.1	0	0.1	0	0	0.1	0
Cr	0	0.1	0	0.1	0.1	0.1	0.1	0.1	2.9	0.1
Mn	0.8	0.8	0.2	0.4	0.6	0.5	0.6	0	0	0
Fe	3.3	2.9	1.3	2.2	2.6	2.5	2.4	0.3	0.2	0.4
Ni	0.2	0.1	0	0	0.1	0	0.1	0	0	0
Zn	0.1	0.1	0.1	0.1	0.2	0.1	0.1	0	0.1	0
O	59.7	59.4	59.1	59.9	59.5	60.7	58.3	49.5	49.1	49.2

Figure 80. As the refractory is corroded by the glass (primarily by alumina dissolution), the chromia content of the refractory is precipitated at the point of dissolution. The glass phase present in this boundary layer serves as the diffusion path for Al and Cr away from the refractory, and the Fe and Ni oxides present in the glass combine with the  $Cr_2O_3$  to form the spinels.

A particularly interesting feature of Figure 81 is the crystalline and glass phase present in the large pore at left center. Table 7 lists the phase composition at the positions indicated. This region is of interest because of the uniformity of the phases present. Location A of the figure was representative of all of the crystals present in this band. This band is also much more similar in composition with respect to the larger crystals (phase C) than similar phases at the refractory/bulk glass boundary. This information, combined with the relatively high Zn content of the phases present (Zn has not been a component of the glasses produced with LFCM since May 1977; see Appendix B) and the similarity of the glass compositions (phases B and D), indicates

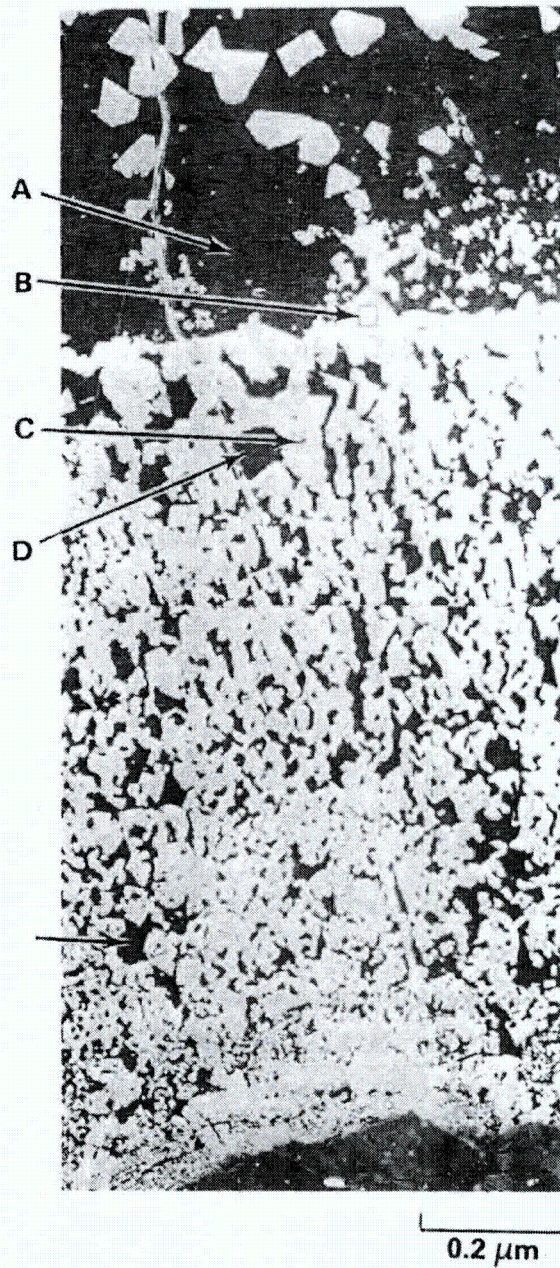


FIGURE 78. Reaction Zone at Monofrax K-3/Glass Interface

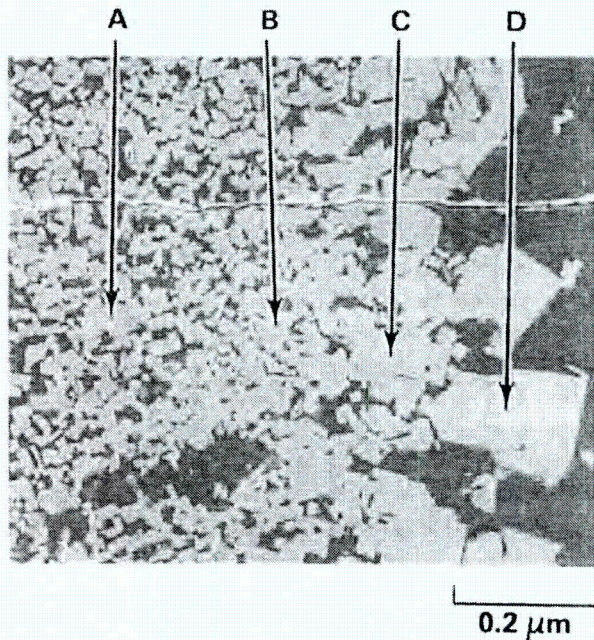


FIGURE 79. Spinel Crystals at Monofrax K-3/Glass Interface

that this region was filled with glass very early in the operating cycle and had come to chemical equilibrium. The fact that chemical equilibrium is indicated in such a large pore relatively close to the glass contact face implies that glass penetration into the bricks will not lead to greatly accelerated refractory corrosion.

From the data gathered during investigations of the Monofrax K-3 corrosion, it can be concluded that the refractory corrosion rate is directly related to the ability of the Al in the bricks to diffuse from the corrosion interface to the bulk glass. This conclusion is supported by the corrosion pattern in the crack shown in Figure 77. Extensive crystal growth is apparent at location A where alumina diffusion to the bulk glass would be most rapid, but progressively fewer phases are present at B, C, and D. This corrosion gradient is shown in Figure 82.

Therefore, to protect the Monofrax K-3 from glass corrosion, the alumina diffusion away from the refractory surface must be minimized. This is best accomplished by maintaining the layer of spinel crystals on the glass-contact

**TABLE 6.** Composition of Phase of Monofrax K-3/Glass Reaction Zone Identified in Figures 78 and 79

Element	Mole%									
	Phase--Figure 78						Phase--Figure 79			
	A	B	C	D	E	F	A	B	C	D
Na	16.3	0	0	15.5	15.2	0	0	0	0	0
Mg	0	0	0.8	0	0	0	0	0	0.7	0
Al	3.1	1.9	2.1	3.3	5.4	2.0	2.3	2.0	1.9	2.1
Si	20.2	0.5	0.7	20.5	20.0	0.8	0.8	0.7	0.6	0.8
S	0.2	0	0	0.2	0.1	0.1	0.1	0	0	0
K	0	0	0	0.1	0.1	0	0	0	0	0
Ca	2.2	0.1	0	2.2	1.8	0.1	0.1	0.1	0.1	0
Ti	0	0	0	0	0	0	0	0	0	0
Cr	0	1.7	7.8	0.1	0.1	9.4	12.4	11.2	6.6	1.0
Mn	0.9	3.8	3.3	0.8	0.6	3.6	3.5	3.1	2.8	3.8
Fe	3.1	24.3	17.9	2.6	2.0	13.3	11.8	13.6	18.8	24.3
Ni	1.1	12.3	10.3	0.1	0	8.0	7.5	6.4	10.4	12.3
Zn	0.1	0	0.2	0.1	0.1	0.4	0.4	0.3	0.1	0
O	53.8	55.4	56.9	54.6	54.5	62.3	61.2	60.7	58.0	55.6

faces. This spinel layer prevents convective mass transport at the refractory face, thereby reducing the rate of alumina transport. Because this layer is composed of discrete crystals suspended in a high-Al glass phase (higher Al content in glasses implies increased viscosity at constant temperature), the temperature of this layer is critical to the corrosion rate. Should the temperature of this glass phase rise, thereby reducing the viscosity to the point that the convective motion of the bulk glass could sweep it from the refractory face, the corrosion rate will be significantly increased. This effect would also be magnified as both the diffusion rate and the velocity of the convective currents present in the melter are strong functions of temperature.

#### 7.1.2 Alfrax 66

During the melter disassembly the Alfrax 66 castable refractory was found to contain many glass-filled cracks. Alfrax 66 corrosion was expected because

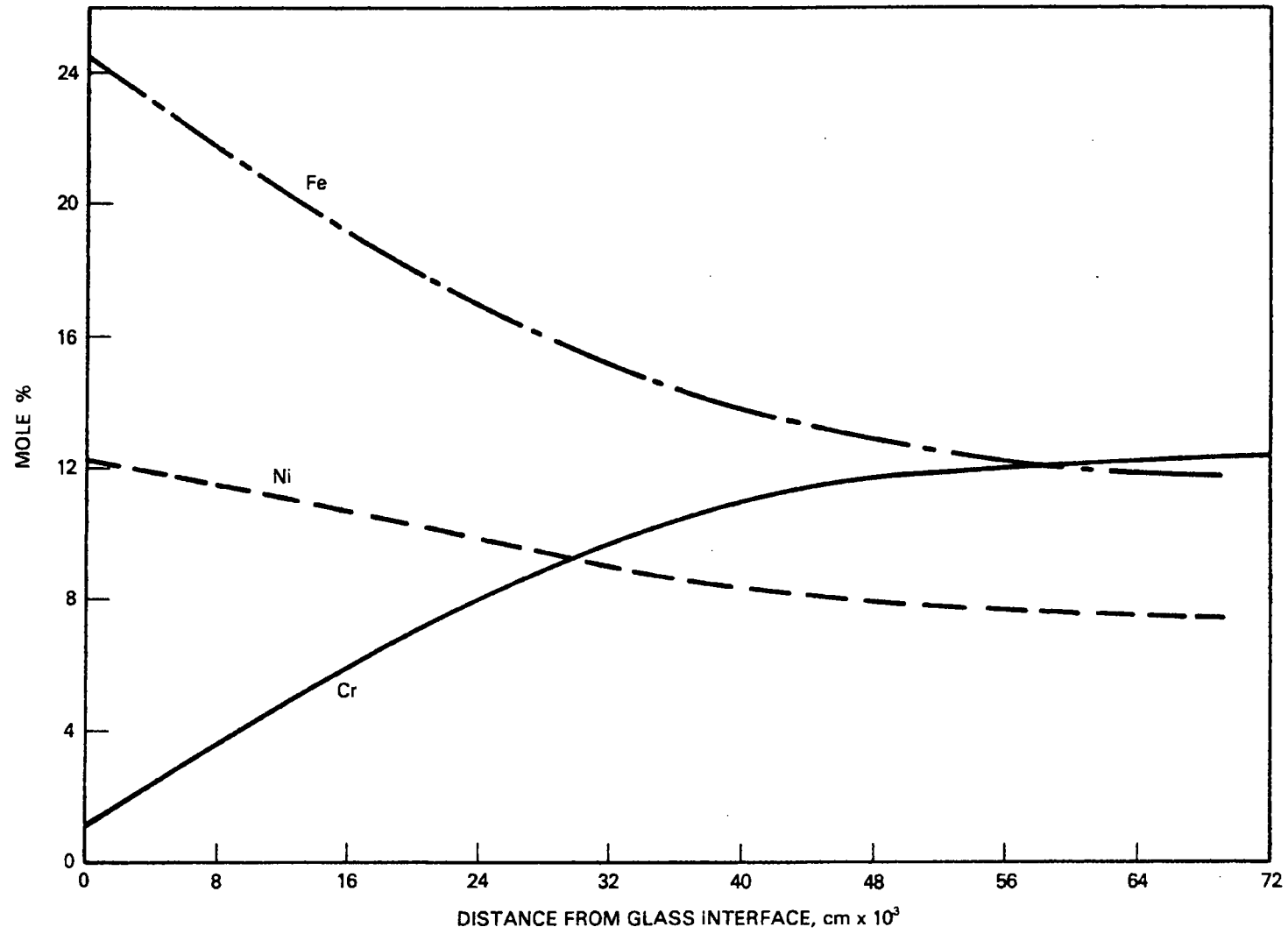


FIGURE 80. Cr-Ni-Fe Gradient Across the Spinel Layer

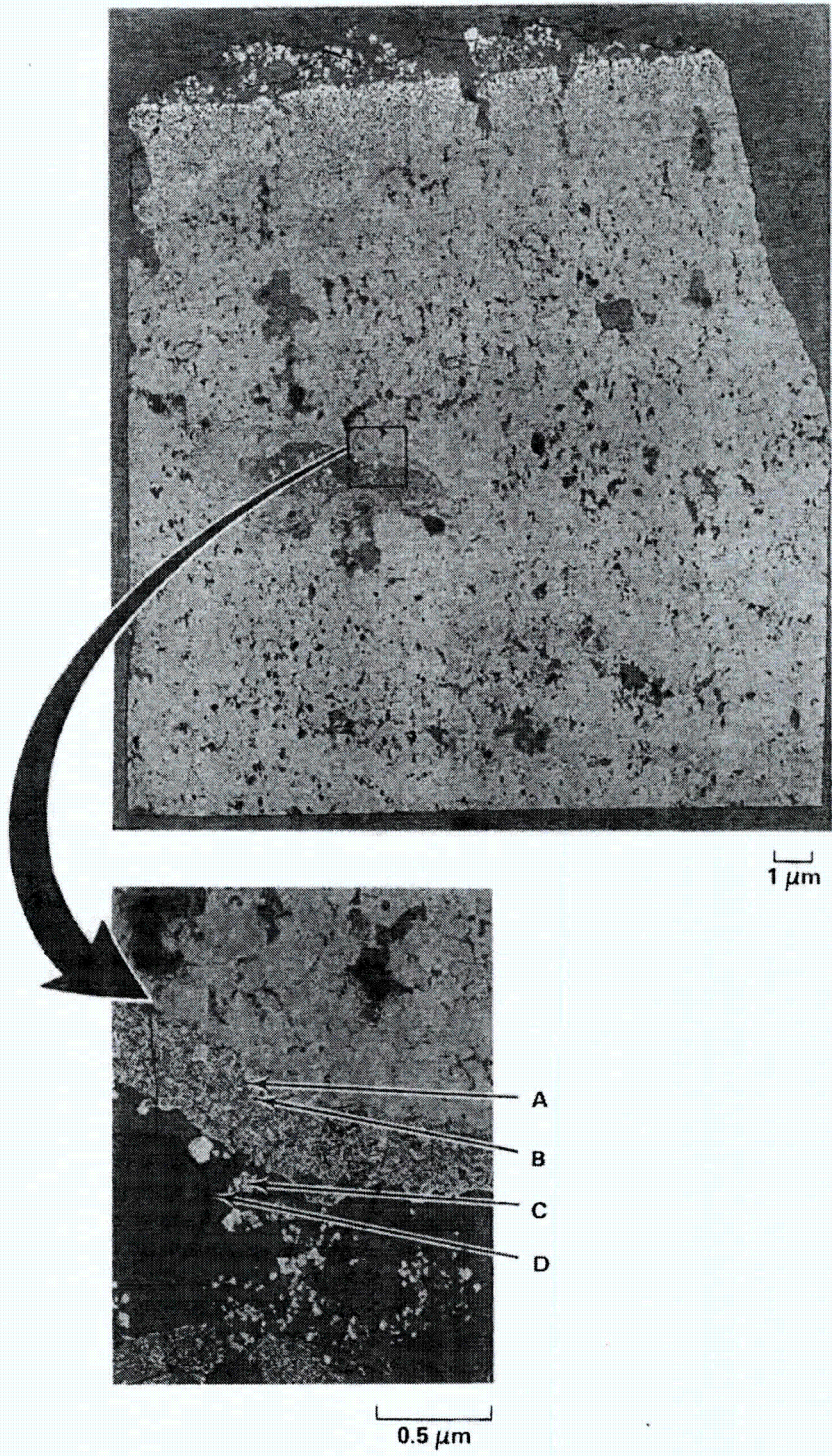


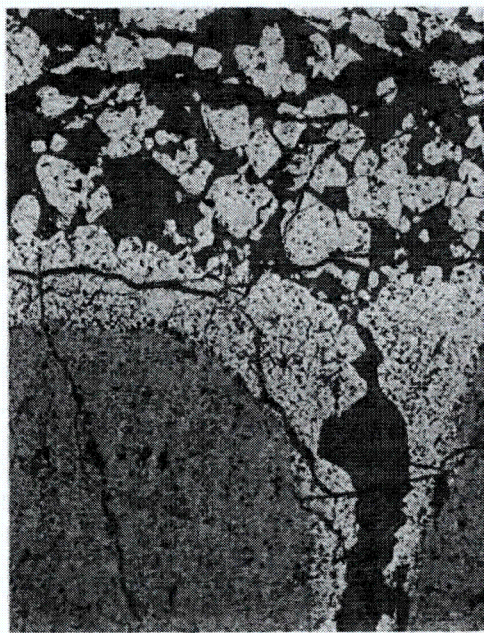
FIGURE 81. Pore in Monofrax K-3 Core

TABLE 7. Composition of Phases Identified in Monofrax K-3  
Pore of Figure 81

Element	Mole%			
	Phase			
	A	B	C	D
Na	0	13.3	0	13.3
Mg	0	0	2.6	0
Al	3.2	5.5	4.0	5.0
Si	0.4	17.8	0.4	17.8
S	6	0.3	0	0.1
K	0	0.1	0	0.1
Ca	0.1	1.7	0.1	1.8
Ti	0.1	0.1	0.2	0.1
Cr	14.7	0.2	17.5	0.1
Mn	3.2	0.3	1.8	0.4
Fe	9.6	1.9	6.9	2.2
Ni	1.0	0	0.9	0
Zn	5.1	0.5	6.9	0.5
O	62.6	58.6	58.7	58.5

Alfrax 66 is almost entirely alumina ( $Al_2O_3$ ) and alumina solubility in the glass has been demonstrated. The expected alumina dissolution of the Alfrax 66, combined with the decreasing temperature profile with distance from the bulk glass, suggests that this refractory could stop glass penetrations, if the glass is in contact with the Alfrax 66 long enough for alumina saturation.

Because glass migration through the Alfrax 66 layer was observed in the LFCM (possibly due to development of the cracks early in the operating history or due to cracking large enough for fresh (not Al-saturated) glass to flow into the crack), samples of the fractured Alfrax 66 were removed from the riser block region and from near the glass pool (discovered on the north wall) to study the nature of the Alfrax 66 and the glass in the cracked regions.



A

0.5  $\mu\text{m}$



B

0.5  $\mu\text{m}$



C

0.5  $\mu\text{m}$



D

0.5  $\mu\text{m}$

FIGURE 82. Enlargement of Areas A, B, C, and D on Figure 81

These samples were examined by SEM techniques to determine the magnitude of the corrosion and the origin of the glass in the cracks.

The Alfrax 66 refractory is composed of a pure, crystalline  $Al_2O_3$  phase suspended in a continuous phase of aluminum and calcium oxides. Figure 83 shows the Alfrax 66 microstructure. The light-gray region in the center is a glass-filled crack. The glass phases in the samples investigated contained

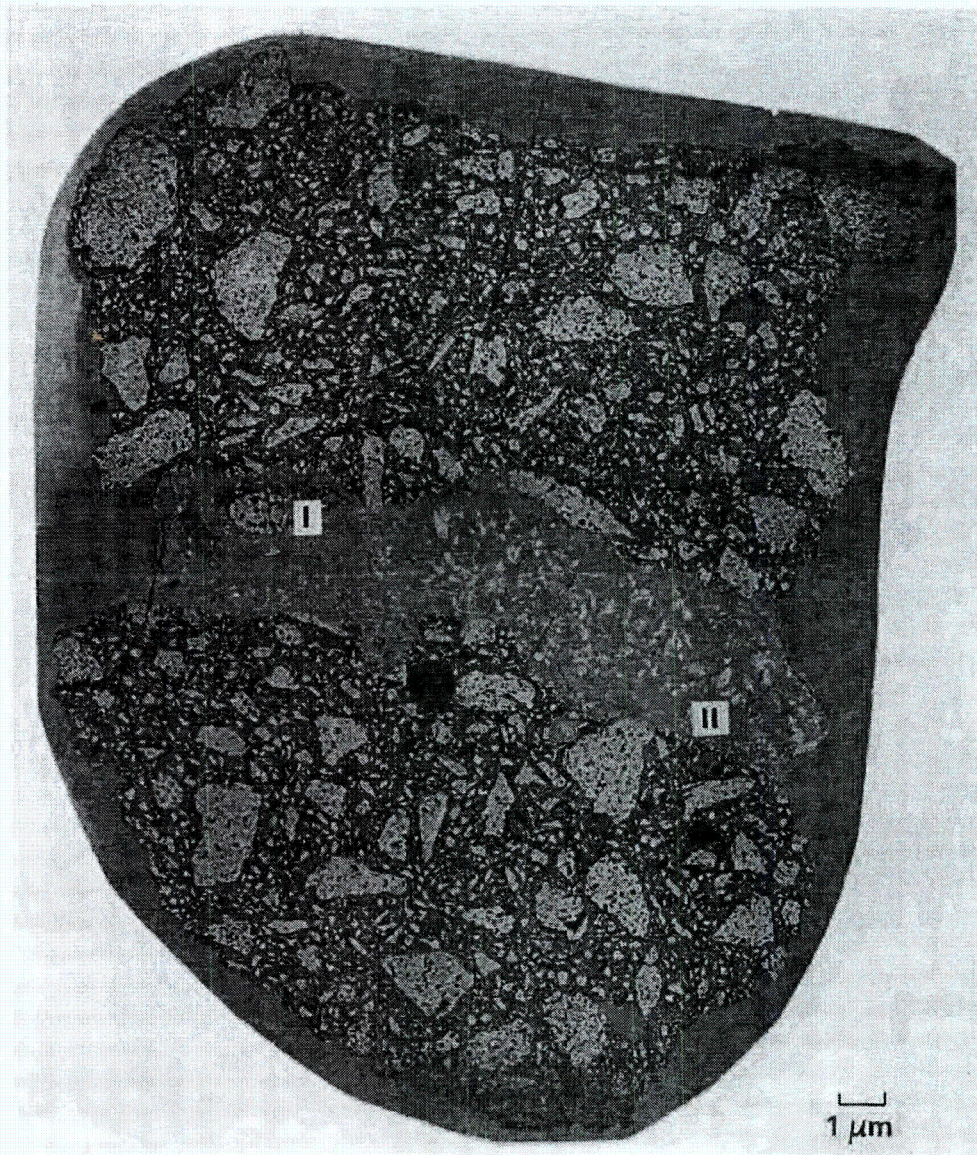


FIGURE 83. Glass-Filled Crack in the Alfrax 66 from North Wall

considerable quantities of Al, Zn, and devitrification products. The high Zn concentration supports the early crack formation hypothesis; therefore, the glass would not have had sufficient time for alumina saturation, thus precluding the crack plugging mechanism predicted.

From examination of Figure 83 it is apparent that the Ca phase is attacked more severely than are the alumina crystals. This can be seen by comparing the fracture surfaces at the edge of the sample to the surfaces exposed to the glass. At the sample edges, the majority of the alumina crystal surfaces retain some of the continuous calcium oxide phase. The alumina crystals at the glass-crack interface do not have this coating. Also, the continuous phase appears to have been dissolved away from several of the crystals, leaving the aluminum oxide phases jutting out into the glass. This effect is more clearly seen in Figure 84 where a section of the Alfrax 66 has

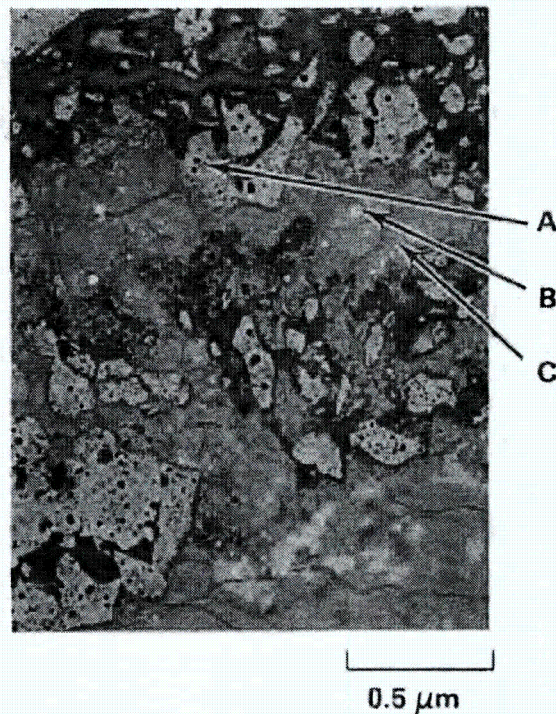
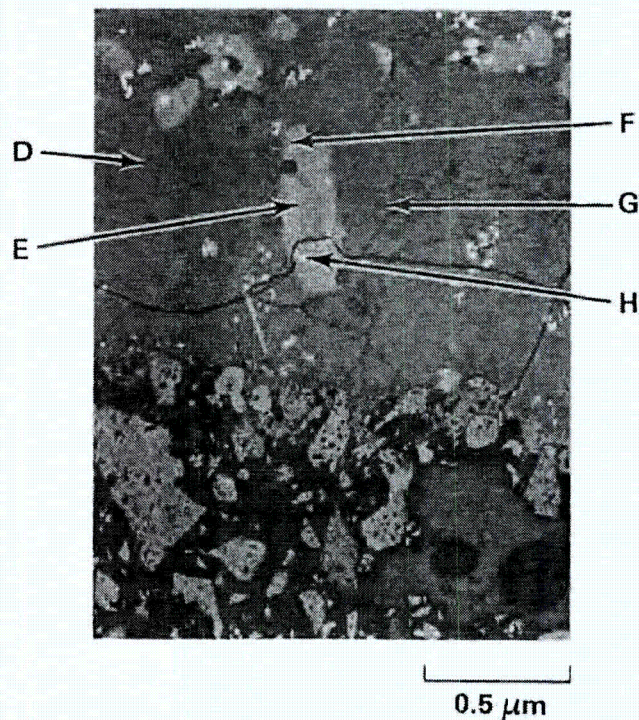


FIGURE 84. Enlargement of Zone I, Figure 83

apparently broken away from the main body of the refractory. The glass has preferentially dissolved the darker, Ca phase, leaving the alumina phase behind. The major devitrification products found in the glass phase are labeled in Figure 85, and the compositional data of the refractory, glass, and devitrification phases are listed in Table 8.

This examination of the cracked Alfrax 66 does reveal corrosion of the refractory. Based on the absence of significant quantities of alumina crystals in the glass phase, which would result from substantial dissolution of the continuous calcia phase, Alfrax 66 demonstrated good resistance to glass corrosion. Therefore, Alfrax 66 can provide excellent long-term services as a backup refractory, especially if the Alfrax 66 installation is designed with the crack-reducing techniques described in Section 5.3.2.



**FIGURE 85.** Typical Devitrification Phases in Alfrax 66 Crack, Zone II of Figure 83

TABLE 8. Composition of Refractory, Glass, and Devitrification Phases of Figures 84 and 85

Element	Mole% Phase							
	A	B	C	D	E	F	G	H
Na	0	1.1	0	14.5	0	9.2	18.8	0
Mg	0	0.5	0	0	0	1.2	0	0
Al	44.7	2.8	25.7	4.2	2.5	1.5	11.5	7.9
Si	0.5	11.4	0.3	17.6	1.1	21.7	14.4	2.4
S	0	0	0	0	0	0	3.0	0
K	0	0.1	0	0.1	0.1	0.1	0	0
Ca	0	2.1	2.2	1.8	0.1	3.1	0.4	0
Ti	0	6.8	0	0.2	2.2	0.2	0	0
Cr	0	0	0	0	8.0	0	0.2	0
Mn	0	0.7	0	0.6	3.8	0.8	0	0
Fe	0	1.9	0	2.0	8.6	7.7	0.6	0.8
Ni	0	0.3	0	0	3.2	0.5	0	0.1
Zn	0	0.4	0	0.4	3.2	0.1	0	0
Zr	0	0.7	0	0.1	0	0.1	0	1.7
La	0	4.3	0	0	0	0.5	0.1	0
Ce	0	0	0	0	0	0	0.1	26.7
Nd	0	1.3	0	0	0	0	0	0
O	54.8	65.5	71.8	58.4	66.4	53.9	50.9	60.4

## 7.2 CORROSION OF METALLIC MELTER COMPONENTS

Samples from the melter electrodes, riser plate, pouring tip, ionic booster electrode and bellows, and a section of offgas ducting were studied to determine the mechanisms producing the corrosion observed.

### 7.2.1 Electrodes

The LFCM electrodes were fabricated from the Inconel 690 nickel-chromium-iron alloy. Following their removal from the melter, the east primary and secondary electrodes were sectioned near the centerline and a sample was

removed from each for detailed examination. Figures 86 and 87 are these polished and etched samples.

Chromium is alloyed with steels to improve the oxidation resistance of the alloy by allowing selective oxidation of the  $\text{Cr}^{+3}$  ion at the corrosion interface. The  $\text{Cr}_2\text{O}_3$  layer thus produced at the interface is relatively stable and impermeable to oxygen diffusion. This precludes further degradation of the material. At high temperatures the formation of the oxide layer creates a region in the alloy that is chromium-depleted. This leads to diffusion of chromium from the body of the material to the surface. This chromium diffusion process continues until the chromium content of the alloy is depleted to 12 to 14 wt% (11 to 13 mole%) and the formation of a passivating layer is no longer possible (Cowan and Tedmon, Jr. 1973).

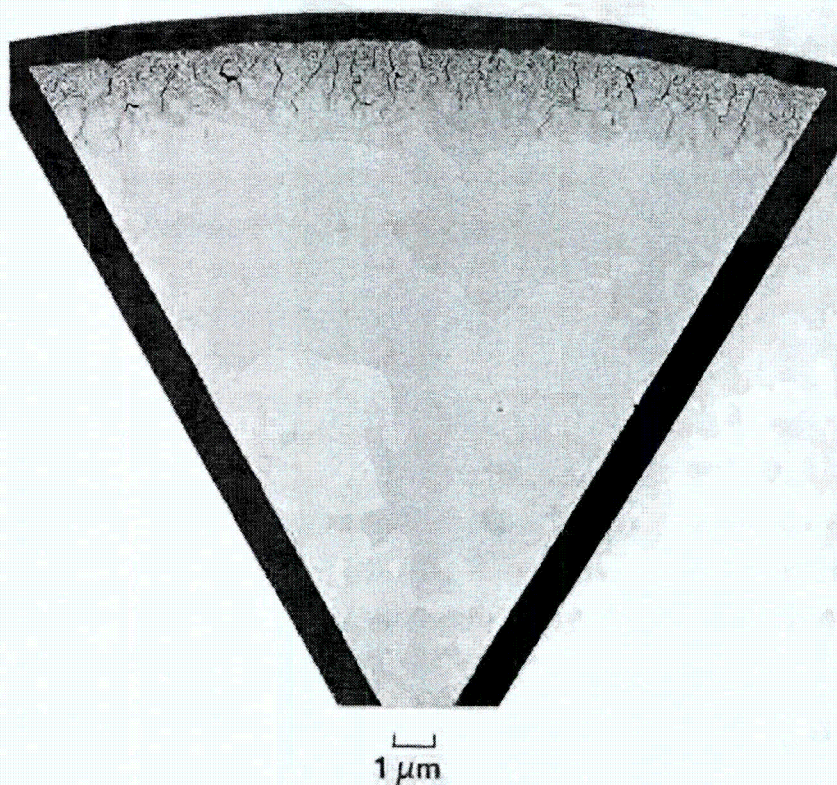


FIGURE 86. East Primary Electrode Reaction Zone

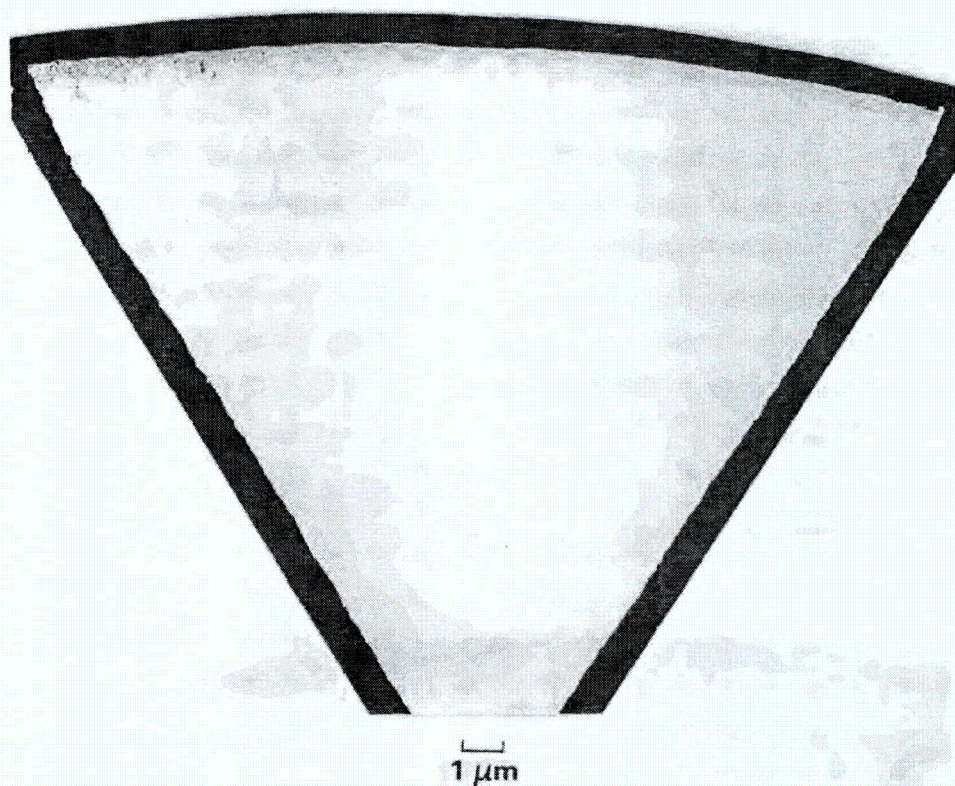
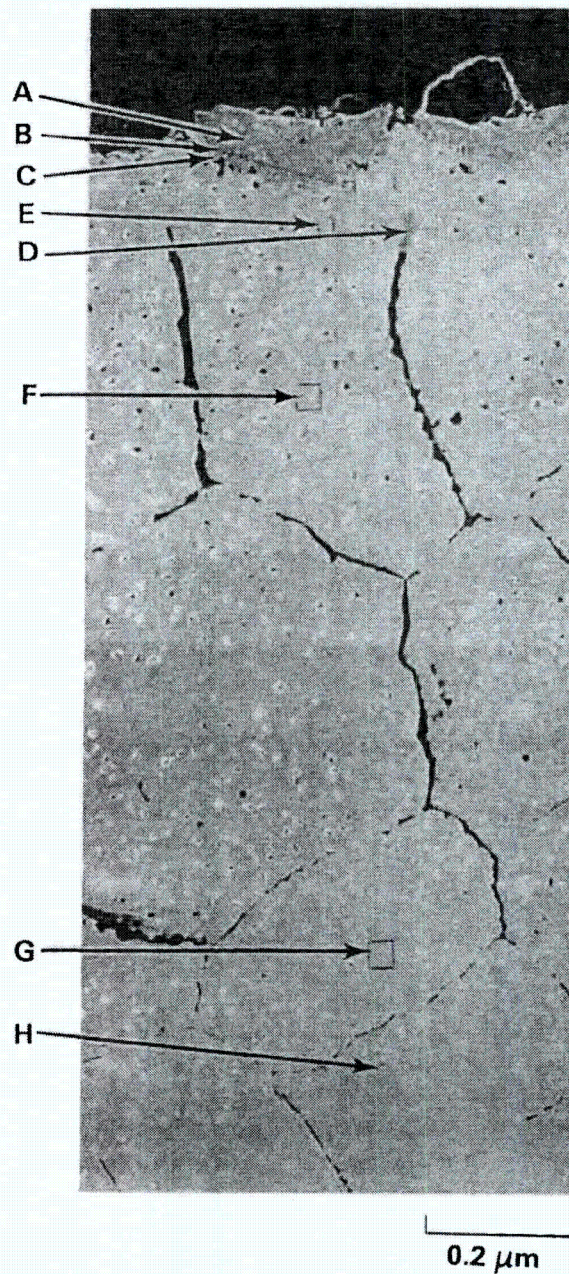


FIGURE 87. East Secondary Electrode Reaction Zone

To examine in detail the performance of the electrodes, the samples removed from the east set of electrodes were analyzed by SEM techniques. As the corrosion process is the same for the primary and secondary electrodes, only the primary electrode is discussed here.

The effects of three years of exposure to borosilicate glasses are apparent in Figure 88. The elemental composition of the areas marked on the figure are listed in Table 9, along with the manufacturer's published composition for Inconel 690.

As noted in earlier descriptions, the electrodes were found to be covered with a layer of material that contained spinel crystals on the surfaces exposed to the glass. Remnants of this layer are evident in Figure 88 and are labeled as Area A. Based on the compositional data, this phase is primarily composed



**FIGURE 88.** Enlargement of East Primary Electrode Reaction Zone

of  $(\text{Mn,Ni})(\text{Cr,Fe})_2\text{O}_4$  spinels. Also, as Mn was detected only in trace quantities in the electrode base alloys, the presence of Mn indicates that this phase was in contact with the molten glass.

**TABLE 9.** Composition of Zones Labeled in Figure 88

Elemental Composition	Base Alloy (Appendix A)	Mole%								Metal far from Reaction Zone
		A	B	C	D	E	F	G	H	
Al	0.5	0.2	0.3	4.4	0.8	0.6	1.0	0.4	0.2	0.6
C	0.14	---	---	---	---	---	---	---	---	---
Cr	32.3	2.8	38.0	32.5	14.9	14.8	19.0	27.6	3.5	29.6
Fe	9.5	26.7	1.3	0.0	8.6	8.8	9.0	8.9	1.01	8.7
Mn	---	1.2	0.8	0.2	0.0	0.0	0.0	0.0	0.0	0.3
Ni	57.3	12.6	0.5	0.4	66.7	66.4	62.0	55.0	5.4	54.6
O	---	55.9	58.9	58.8	7.0	7.7	7.3	6.7	48.1	4.0
Si	---	0.6	0.4	0.4	1.9	1.5	1.7	1.3	0.7	1.9
Ti	0.3	0.1	0.6	3.3	0.6	0.1	0.0	0.1	41.0	0.3
Fe/Ni	0.2	2.1	2.8	0	0.1	0.1	0.1	0.2	0.2	0.2
Cr/Ni	0.6	0.2	80.8	81.3	0.2	0.2	0.3	0.5	0.6	0.5

Area B of Figure 88 is composed of  $(\text{Fe,Ni})\text{Cr}_2\text{O}_4$  and  $\text{Cr}_2\text{O}_3$ . In this region, the Fe exists only in the ferrous state. The most interesting aspect of this layer is the decrease of the Mn concentration and the high Fe/Ni ratio relative to the base metal. The high Fe/Ni ratio implies that the FeO present in the glass diffuses across the outer layer and slowly forms the  $\text{FeCr}_2\text{O}_4$  spinel. This observation is supported by the large value of the diffusion coefficient,  $52 \text{ cm}^2/\text{s}$ , for diffusion of iron through  $\text{NiFe}_2\text{O}_4$  over the temperature range of 850 to  $1190^\circ\text{C}$  (Kubaschewski and Hopkins 1962). This data indicates that the Fe, Mn, and Ni present in this layer came from the glass rather than from the base metal. (The early formulations contained much greater quantities of iron than of nickel or manganese; see Appendix B.) The high Cr/Ni ratio shows that this is the passive chrome oxide layer predicted by corrosion theory. This layer varies in depth from  $\sim 30$  to  $50 \mu\text{m}$ .

The presence of phase C is also predicted by corrosion theory. In austenitic metals (face-centered cubic-crystalline structure), the solubility of carbon is low ( $<0.03\%$  for an 18-8 stainless steel). The solubility limit

of carbon decreases with increasing Ni content (Cowan and Tedmon, Jr. 1973); therefore, for a 60-wt% Ni austenitic alloy, the solubility limit can be expected to be very low. In alloys such as Inconel 690, where carbon is present as an impurity, the excess carbon above the solubility limit accumulates at the grain boundaries. Chromium, very reactive with carbon, tends to diffuse to the boundaries and form carbides ( $\text{Cr}_{23}\text{C}_6$ ). Formation of the chrome carbides can leave a chromium-depleted zone near the grain boundary. This process is termed "sensitization" and can lead to disastrous consequences if the Cr content of the metal at the grain boundaries falls below the 12 to 14 wt% required for passivation. To prevent the formation of chromium carbides ( $\text{Cr}_{23}\text{C}_6$  does not provide corrosion passivation), Inconel 690 includes 0.25 wt% titanium. The free-energy of formation of titanium carbide is more negative than chromium carbide; therefore, the Ti phase forms preferentially.

This carbide model explains the high Ti concentration in phase C. Because of the nature of the SEM, elements lighter than sodium are very difficult to detect; therefore, the oxygen concentration is obtained by subtraction, and trace quantities of other light elements are probably present. Proceeding with the assumption that all of the Ti is present as the carbide, and readjusting the mole percentages to reflect this, phase C composition is  $\text{TiC}$ ,  $\text{MnO}_2$ ,  $\text{Al}_2\text{O}_3$ ,  $\text{NiO}$ ,  $\text{SiO}_2$ , and  $\text{Cr}_2\text{O}_3$ . The Al present in the Inconel 690 alloy is added to increase the corrosion resistance of the alloy, most notably to  $\text{SO}_2$  attack; therefore, increased  $\text{Al}_2\text{O}_3$  formation at the grain boundaries is not surprising (Kubaschewski and Hopkins 1962).

Regions D, E, F, and G of Figure 88 indicate the composition of the base metal away from the reaction zone. The most notable features of these zones are the randomly arranged voids and large gaps at the grain boundaries. These voids arise from the diffusion of the Cr atoms to the reaction zones faster than the austenitic lattice can fill the resulting vacancies. The vacancies coalesce at the grain boundaries and lattice imperfections and form the voids. This mechanism of subsurface void formation is the Kirkendall effect (Kroger

1974). The assumption on which this effect is based is that different atomic species can move at different velocities in an alloy. This difference in species-diffusivity can be seen by comparing the Cr concentration in the alloy with respect to position, Figure 89, to the constant Fe/Ni ratio for these regions (Table 9).

The remaining phase, H (in Figure 88), is the alloy formed by the Ti inclusions in the alloy. These inclusions are distributed throughout the grains and are probably the nucleation sites for the in-grain Kirkendall voids.

#### 7.2.2 Riser Plate

An Inconel 690 structural member, termed the riser plate, was placed above the melter drain to reinforce the castable refractory (Alfrax 66) in the region. This member was exposed to the ambient conditions above the melt for the entire operating period. This component was selected for analysis because the corrosion experienced at this location is probably representative of all the Inconel components above the melt, such as the externally insulated lid.

A section of the riser plate was removed and examined by optical and SEM techniques. Figure 90 is a picture of this sample. The swelling at the bottom and the rough edge are broken weldmelts.

The presence of the internal voids in the sample resembles the corrosion of the electrodes, but a fundamental difference exists in the corrosion mechanisms. It is apparent from inspection of Figure 91 that a continuous layer of  $\text{Cr}_2\text{O}_3$  is not present and that base metal is exposed to the melter environment. This is due to the low Cr concentration at the metal/gas interface. Examination of the compositional data presented in Table 10 reveals that the Cr content at the interface is very near the lower limit required for formation of the passivating layer. Figure 92 illustrates the concentration of Cr versus depth into the riser plate.

Because the metal near the interface is deficient in Cr, and only isolated pockets of  $\text{Cr}_2\text{O}_3$  formation are evident, a mechanism for the removal of Cr species must exist. This phenomenon is almost certainly tied to the temperature

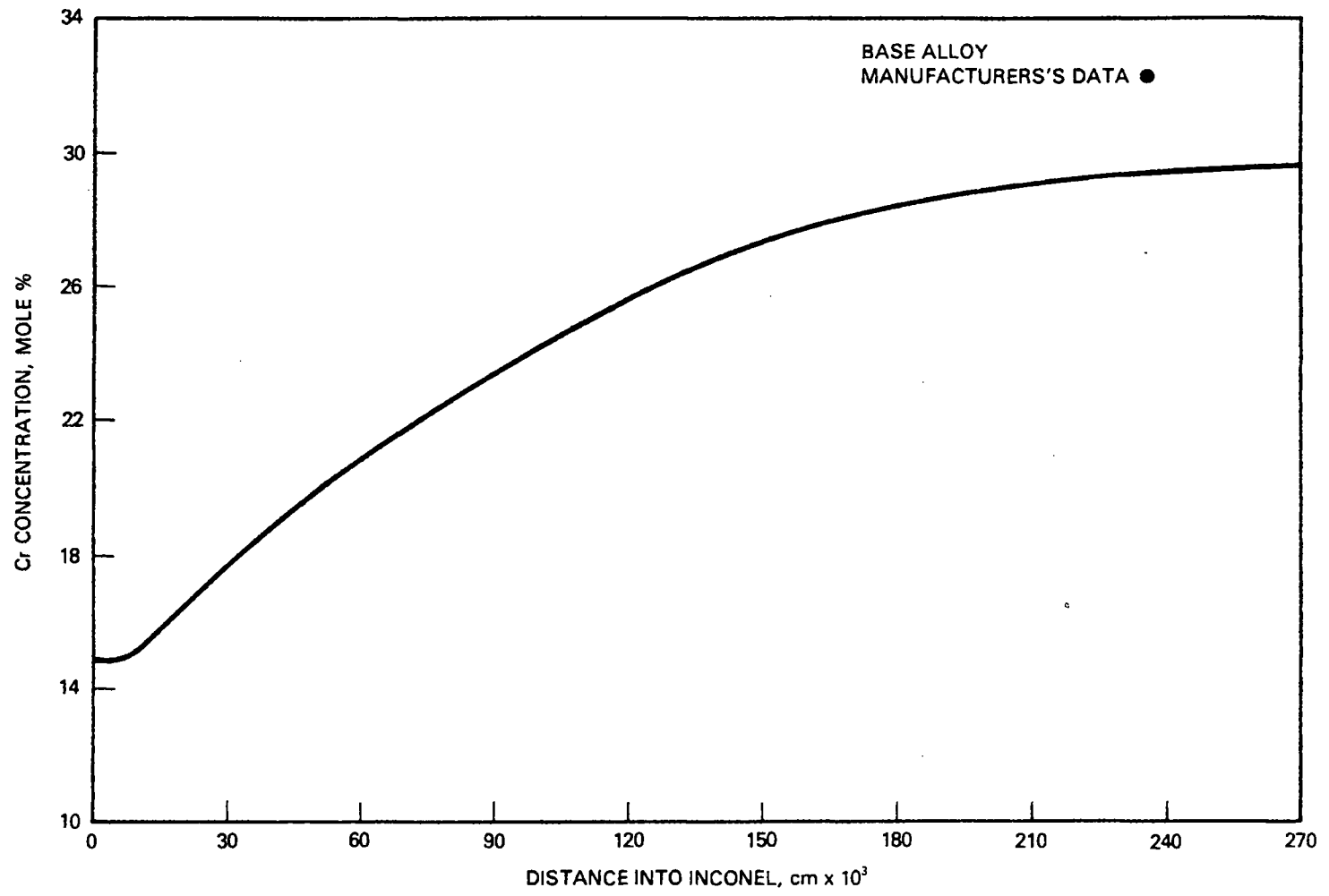


FIGURE 89. Chromium Gradient in East Primary Electrode

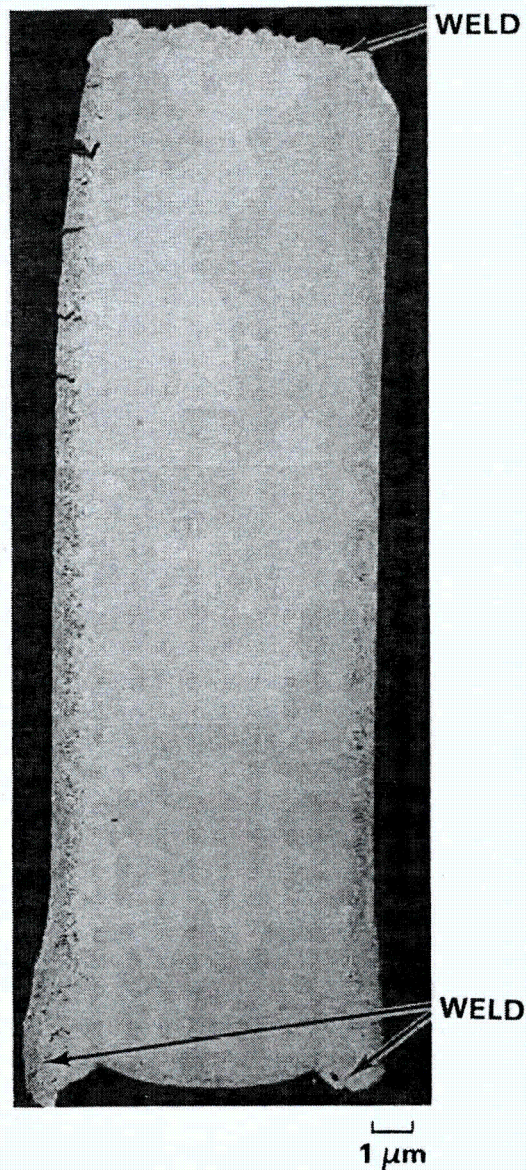


FIGURE 90. Section from LFCM Riser Plate

cycling inherent to the melter plenum. In this region, the nominal temperature range is 850<sup>o</sup> to 950<sup>o</sup>C, but during glass processing tests, the temperature varies from about 100<sup>o</sup> to 1000<sup>o</sup>C.

Among the possible chromium removal mechanisms are chromium dissolution in condensed nitric acid during slurry feeding, formation of volatile chrome

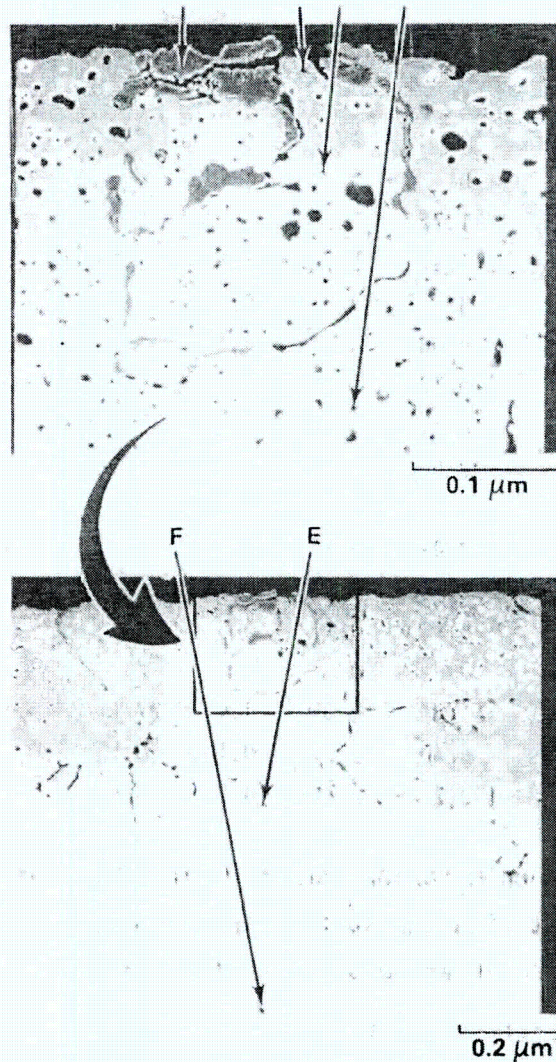


FIGURE 91. Enlargement of Riser Plate Reaction Zone

chlorides, and formation of chromium carbonyl. Condensed water vapor forming on the riser plate during fully flooded slurry feeding tests would react with  $\text{NO}_x$  (assuming an acid-feed solution) to form nitric acid. Chromium could be leached from the alloy by this acid solution and then could drip onto the cold cap surface. Chloride impurities are found in the  $\text{Fe}(\text{OH})_2$  compound used in the HLW simulation. This chlorine could react with the chromium, producing a

TABLE 10. Compositions of Riser Plate Reaction Zone Locations

Elemental Composition	Base Alloy (Appendix A)	Mole%						Metal far from Reaction Zone
		A	B	C	D	E	F	
Na	---	0	0	0	0	0	0	---
Mg	---	0	0	0	0	0	0	---
Al	0.5	1.72	1.98	1.80	2.45	2.36	2.37	0.5
Si	---	0.31	1.90	1.58	1.57	1.46	1.58	---
S	---	0	0	0	0	0	0	---
K	---	0.08	0	0.1	0	0	0	---
Ca	---	0.14	0.22	0	0.11	0.23	0.12	---
Ti	0.3	0.61	0	0	0.009	0.19	0	0.3
Cr	32.3	33.97	11.71	11.13	18.01	21.62	27.37	29.6
Mn	---	0	0	0	0	0.08	0.18	0.3
Fe	---	0.42	6.77	6.16	6.73	7.10	7.59	9.5
Ni	57.3	0.30	49.37	41.29	43.42	42.79	46.64	57.3
Zr	---	0.09	0	0	0	0	0	---
Mo	---	0	0	0	0	0	0	---
O	---	62.37	28.05	37.93	27.61	24.17	14.16	4.0
Fe/Ni	0.2	1.40	0.14	0.15	0.15	0.17	0.16	0.2
Cr/Ni	0.6	113.2	0.24	0.27	0.41	0.51	0.59	0.5

volatile species. Carbon monoxide formed during carbonate feed decomposition potentially could react with the surface chromium to form chromium carbonyl ( $\text{Cr}(\text{Co})_6$ ), which is also known to be a volatile chromium compound.

To test these hypotheses, several x-ray maps of the riser-plate samples were completed (see Figure 93). In Figure 93, several localized Cr phases can be seen near the surface. An x-ray map was performed for chlorine, but the results were inconclusive. This was expected as metal chlorides generally have high vapor pressures. If volatile Cr/Cl compositions were created, they certainly would have vaporized during the idling period before the melter shutdown. Also, analysis of the high Cr phase does not predict  $\text{Cr}_2\text{O}_3$ , but an alloy with a higher  $\text{O}_2/\text{Cr}$  ratio. This is probably due to the residual oils (the samples were polished using a light oil solution before the photomicroscopy)

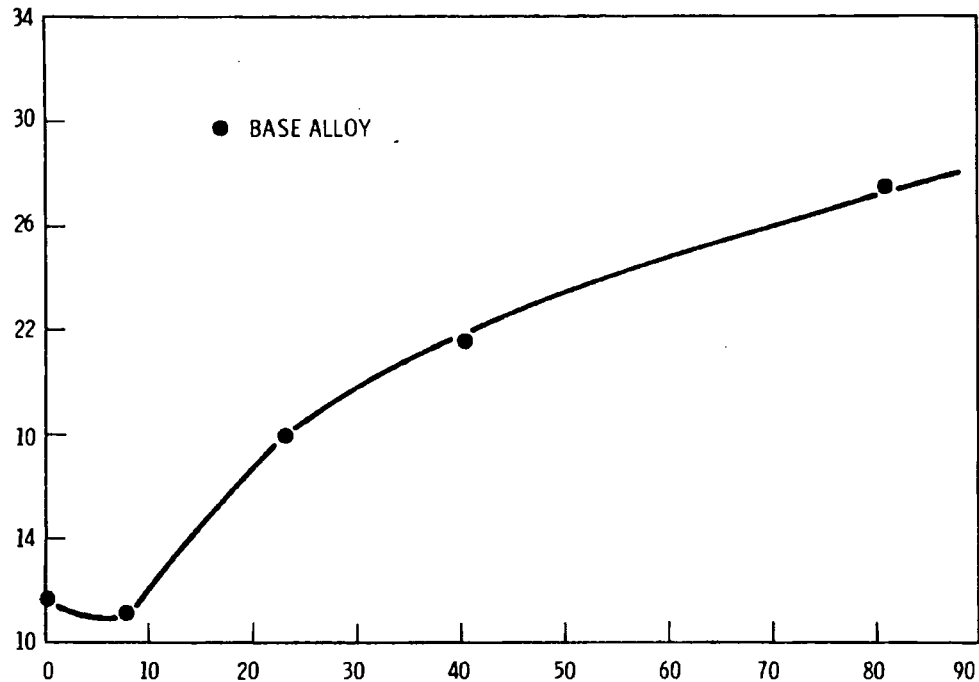


FIGURE 92. Chromium Gradient in Riser Plate Sample

present in this sample from the polishing process. As outlined earlier, the oxygen concentration reported from SEM analyses is obtained from subtraction of the total concentration of elements heavier than Ne from 100%. Therefore, any residual hydrocarbons would be included in the oxygen concentration.

### 7.2.3 Pouring Tip

The melter pouring tip (the point at which the glass falls from the melter drain to the canister) was fabricated from Inconel 690. The glass is poured down the face of the pouring tip along a machined groove. A sample of the pouring tip was removed and then examined using the same methods as the electrodes and the riser plate. Figure 94 shows the appearance and design of the pouring tip. Some residual glass is evident in the notched section.

The actual corrosion of the base metal is similar to that found in the electrodes and riser plate. The Kirkendal voids are evident in Figure 94, and

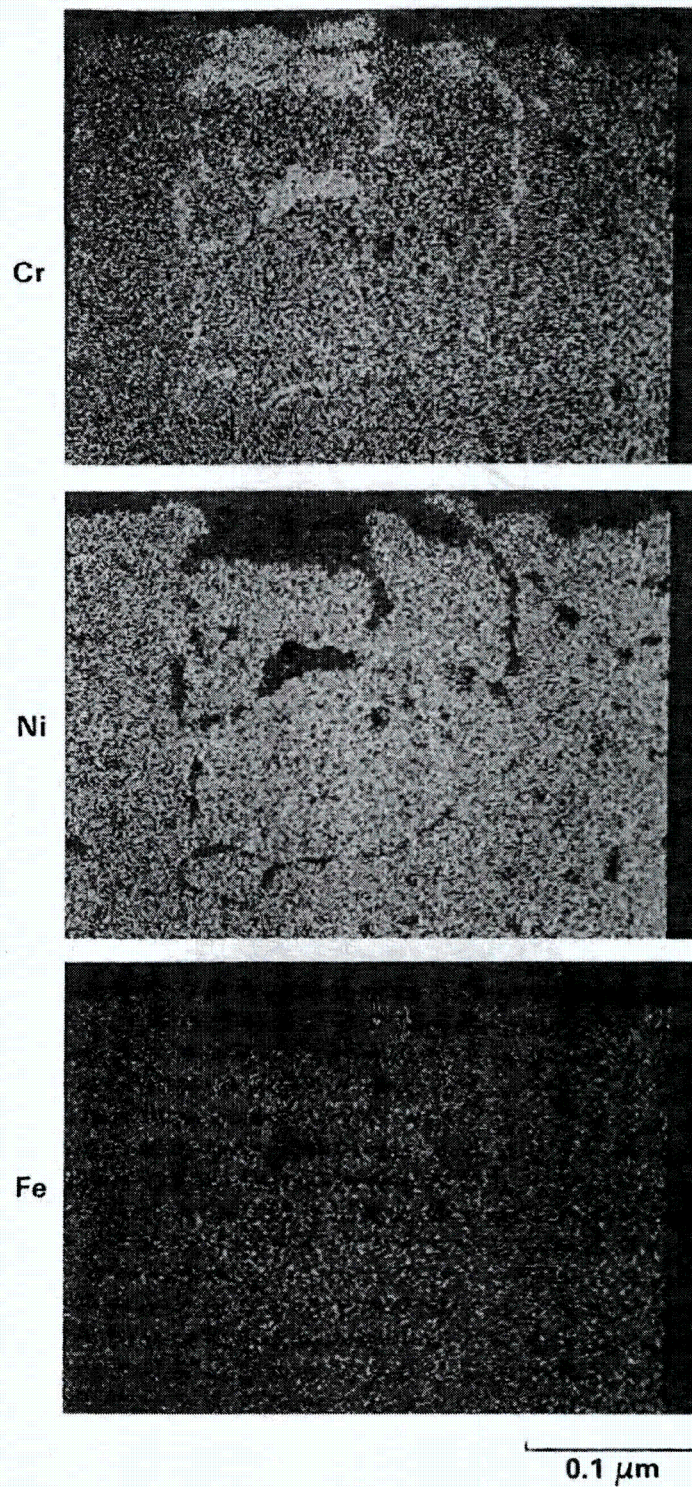


FIGURE 93. X-Ray Maps of Riser Plate Reaction Zone

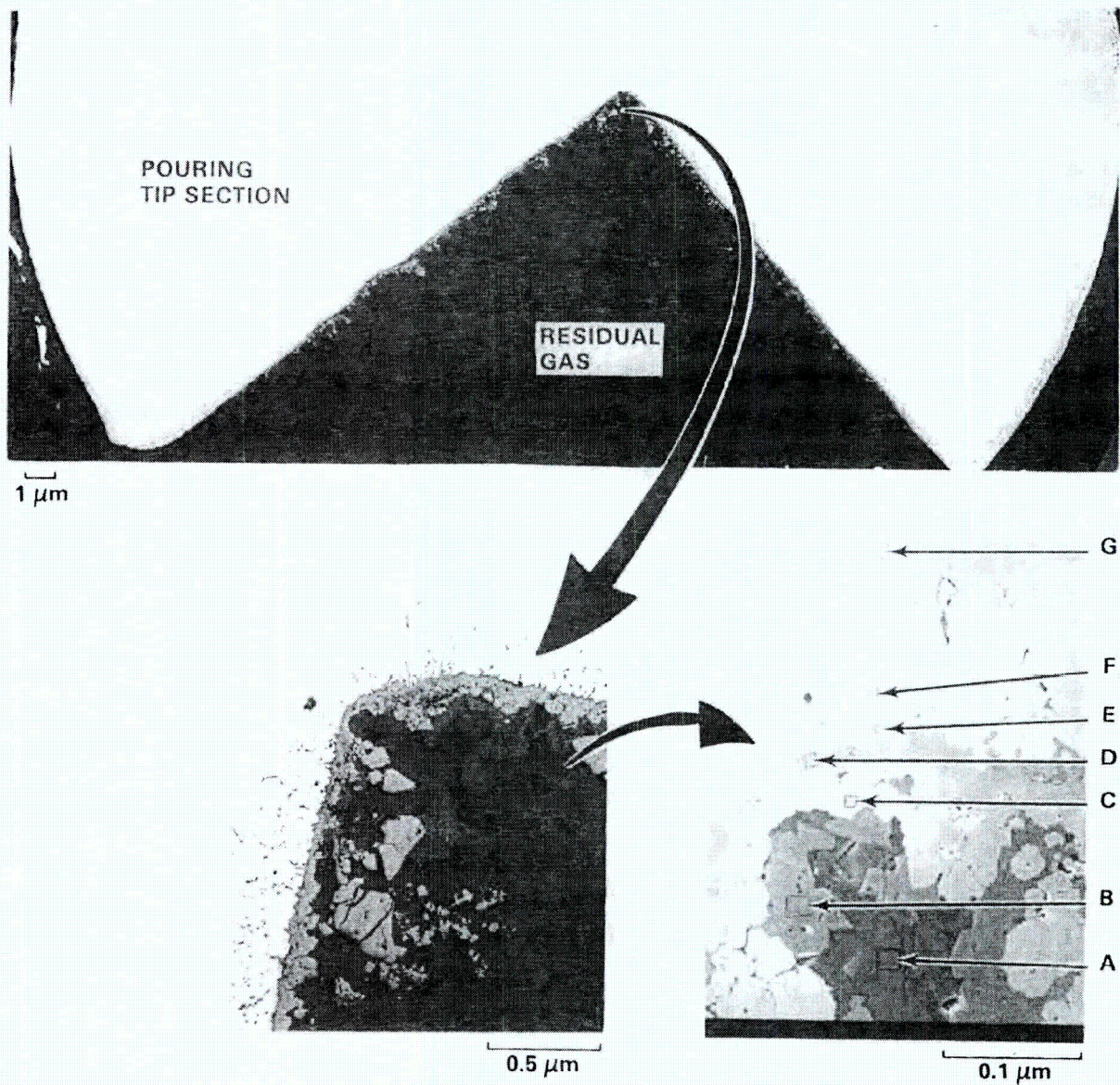


FIGURE 94. Section of LFCM Pouring Tip

the metal displays a similar Cr-concentration profile as detected in the previous samples. The elements present in the various zones indicated in Figure 94 are compiled in Table 11.

As with the electrode, the pouring tip forms a protective layer of Cr oxide at the surface of the metal. On this layer, the familiar (Ni,Mn)

TABLE 11. Composition of Phases in Pouring-Tip Reaction Zone

Elemental Composition	Mole% in Reaction Zone:							Metal far from Reac- tion Zone	Base Alloy (Inconel 690) (Appendix A)
	A	B	C	D	E	F	G		
Na	15.2	8.9	0	0	0	0	0	---	---
Mg	0	1.7	0	0	2.37	0	0	---	---
Al	3.5	0.6	1.0	1.12	3.49	2.13	2.15	0.6	0.5
Si	18.3	22.6	0.96	0.54	2.05	1.86	2.06	1.9	---
S	0.1	0	0	0	0	0	0.33	---	---
K	0.1	0	0	0.08	0.13	0	0	---	---
Ca	2.2	3.7	0	0.15	0.13	0.13	0.26	---	---
Ti	0	0	0	0.57	0	0	0	0.3	0.3
Cr	0.21	0.3	1.36	36.36	21.14	19.64	24.02	29.6	32.3
Mn	0.8	1.1	3.37	1.65	0	0	0	0.3	---
Fe	1.8	7.0	25.75	0.60	8.63	8.91	7.65	8.7	9.5
Ni	0.1	0.9	12.67	0.72	57.15	59.14	57.27	54.6	57.3
Zn	0.1	0	0	0.14	0	0	0	---	---
Mo	0	0	0	0	0	0	0	---	---
O	57.6	54.89	54.89	59.56	4.91	8.18	6.26	1.9	---
Fe/Ni	18	7.78	2.03	0.83	0.15	0.15	0.13	0.2	0.2
Cr/Ni	2.1	0.33	0.11	50.50	0.37	0.33	0.42	0.5	0.6

(Fe,Cr)<sub>2</sub>O<sub>4</sub> spinel zone has formed. Attached to this phase, as well as precipitating in the glass phase, is a crystalline material very similar to acmite [(Na,Ce)(Fe,Mg,Mn,Ni)Si<sub>2</sub>O<sub>6</sub>].

#### 7.2.4 Ionic Booster Electrode

The ionic booster electrodes were fabricated from 304L stainless steel pipe. The electrodes were designed to be water-cooled, but pinholes (probably in a failed weld) in the electrodes prompted forced-air cooling during the final three months of operation.

Samples from one of the booster electrodes were removed and examined by x-ray fluorescence. The samples were removed from two locations on the electrode. The first sample was cut from a section of the stainless steel piping and the second was removed from the weld zone where the piping was sealed.

The welded zone was of particular interest as this area was especially brittle following the electrode removal.

The probable corrosion mechanism for this specimen involves sensitization, sigma ( $\sigma$ ) phase formation, and accelerated oxidation along the grain boundaries. This mechanism is indicated by the analysis and also explains the brittle failure of one of the electrodes at the weld zone on removal. The course of events for this corrosion sequence is believed to be the following:

1. During the initial coolant failure the electrode remains in the sensitization temperature range ( $500^{\circ}$  to  $800^{\circ}\text{C}$ ) long enough for  $\text{Cr}_{23}\text{C}_6$  to form at the grain boundaries. As significant sensitization can occur in less than an hour (Fontana and Greene 1978), it is likely that the electrodes were largely affected in the time required to vaporize the remaining coolant and climb to the plenum temperature.
2. The electrodes idled at ambient plenum temperatures ( $\sim 1000^{\circ}\text{C}$ ) for several days. This temperature is too high for sulphate attack, but encourages intergranular oxidation. Oxygen cracking in sensitized 304L stainless steel is also encouraged by minimal amounts of chloride (Sedricks 1979). Tracers of Cl were found on the metal surface. This temperature is also too low to encourage rapid diffusion of Cr back into the sensitized alloy.
3. Cooling was restarted and the metal was quenched, retaining the sensitization.
4. A second cooling failure occurred, same events as #1, #2, and #3.
5. Cracking sufficient to produce visible cooling water leaks was observed and the electrode coolant was changed to air. The air cooling produced electrode temperatures of  $\sim 400^{\circ}\text{C}$ . This temperature is too low for sulfide attack, but extended periods produce  $\sigma$  phase precipitate at the grain boundaries (Kubaschewski and Hopkins

1962). The oxidized grain boundaries and  $\alpha$  precipitates (a complex chromium-iron compound) would produce the observed brittle failure.

This scenario is supported by the experimental results. The samples examined are pictured in Figure 95. The results of the SEM analysis of Areas A and B of Figure 95 are presented in Figure 96. These results show the

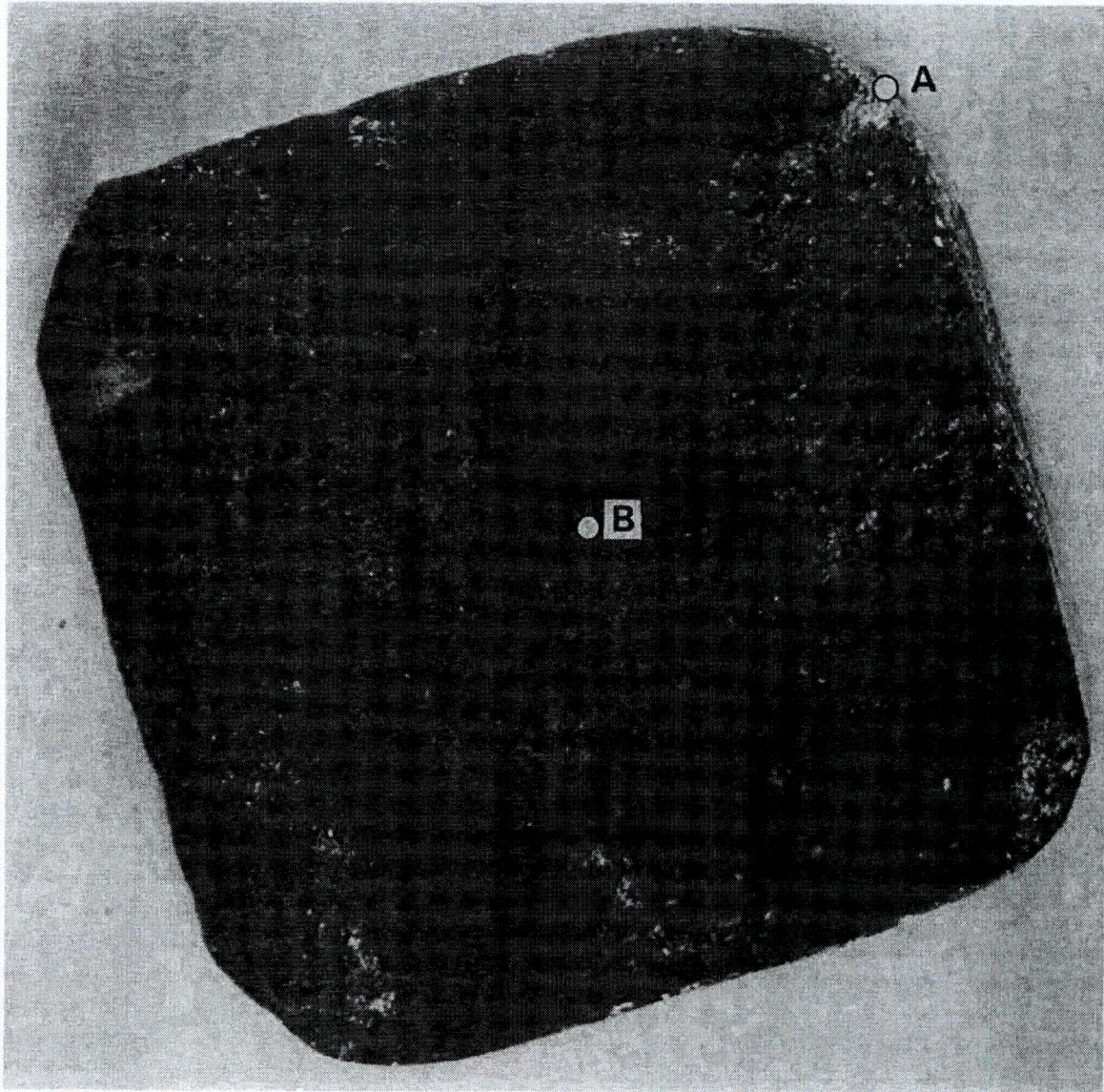
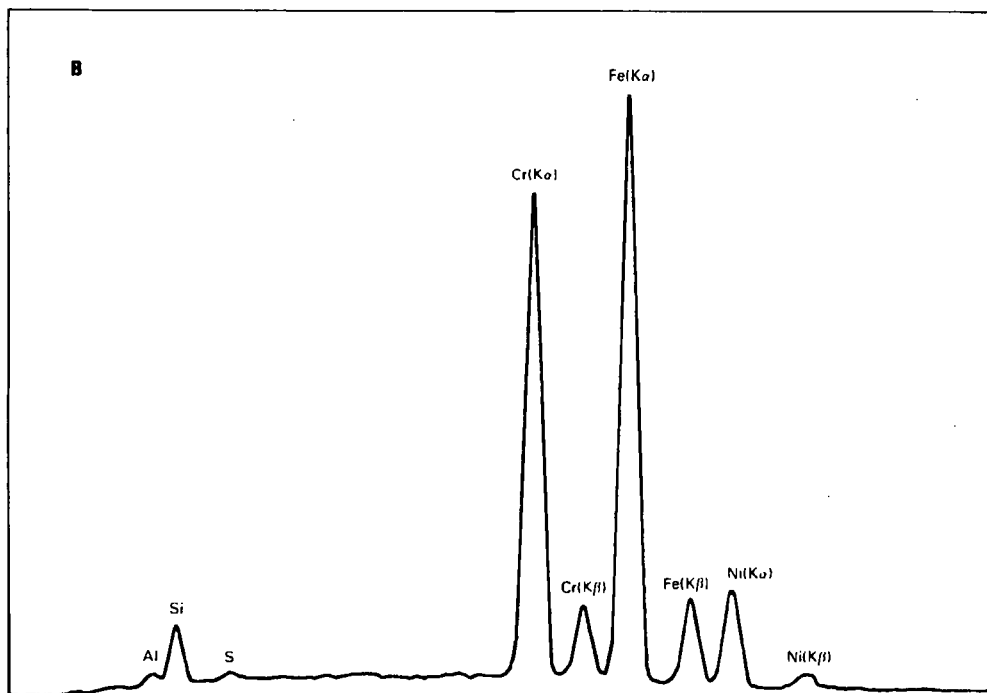
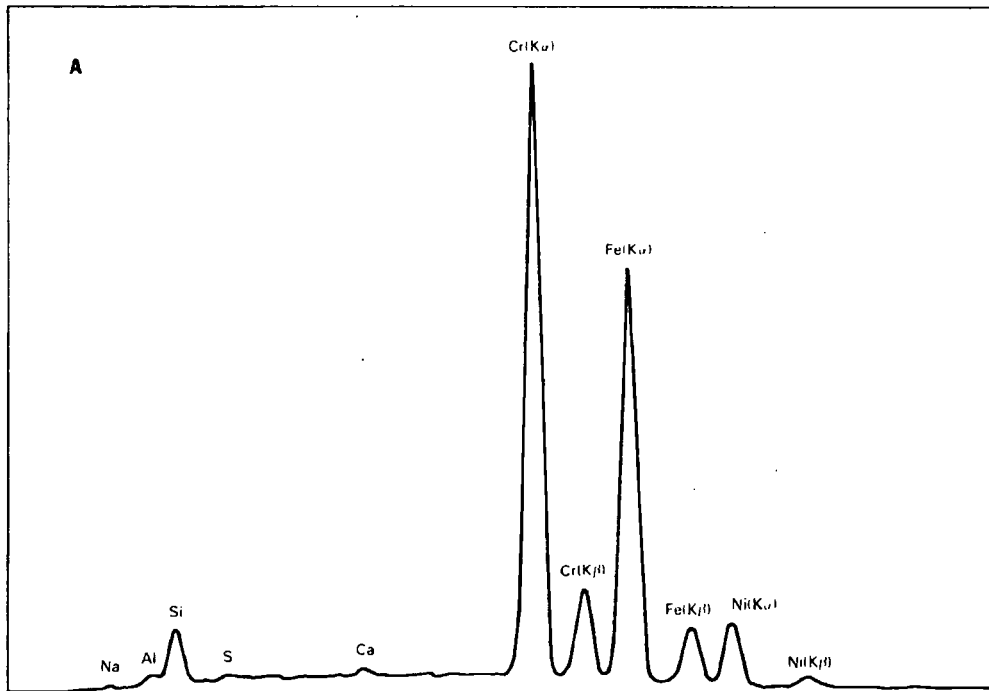


FIGURE 95. Corroded Ionic Booster Electrode



**FIGURE 96.** Microprobe Analysis of Zones Identified on Figure 95

high concentration of Cr relative to Fe (the elemental composition 304L is presented in Appendix A). The high concentration of Cr at the surface is indicative of severe sensitization.

The results of the weld zone sample analysis is plotted in Figure 97. This analysis also shows very high Cr concentration, but Cl and many of the melter feed chemicals (Si, Al, Ca, etc.) were also detected. The action of the Cl is outlined above. The presence of the feed chemicals in abundance at this location relative to the other sample suggests that this surface retained traces of glass from some glass-foaming period.

#### 7.2.5 Ionic Booster Bellows

The flexible metal bellows, designed to seal the ionic booster penetrations in the melter containment, were corroded by a sulphidation mechanism, as opposed to the high-temperature oxidation detected in the booster electrodes. The bellows were exposed to the same operating temperature as the melter cover plate (800<sup>o</sup> to 900<sup>o</sup>C during idling, variable during operation) at the hot end, with the temperature decreasing with distance away from the melter. The bellows were also constructed of stainless steel 304L. On removal from the LFCM the bellows had lost all elasticity and were partially covered with a yellow/green precipitate.

Because the ionic booster penetrations were in the extreme northeast and west corners of the cover plate, the bellows would have experienced relatively cool temperatures during feeding periods. This low temperature would have encouraged the condensation of melter volatiles, notably NaCl. Because of the low temperatures, however, little corrosion would have occurred until the melter was returned to idling. Given these observations, most of the bellows' corrosion would have occurred under dry, oxidizing ambient conditions.

Type 304L stainless steel generally exhibits good corrosion resistance to sulphates at 800<sup>o</sup>C (Sedricks 1979) in the absence of a "triggering" species (Donachie, Jr. et al. 1967). In this case, the corrosion is triggered by the presence of the chlorine compounds. Sodium chloride that has condensed on the alloy surface can react with SO<sub>2</sub> to form Na<sub>2</sub>SO<sub>4</sub>. These two salts (NaCl,

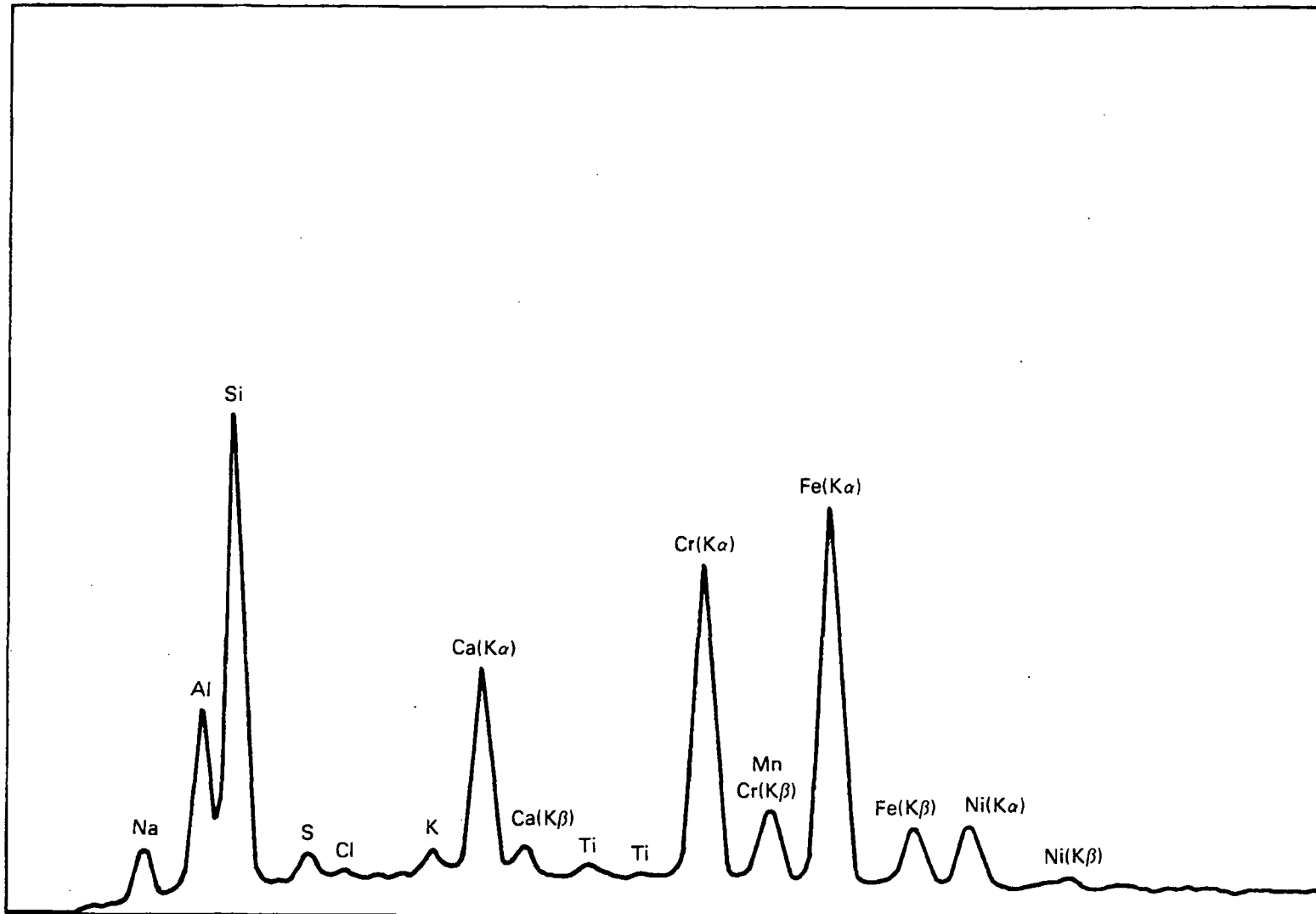


FIGURE 97. Microprobe Analysis of Failed Ionic Booster Weld Zone

$\text{Na}_2\text{SO}_4$ ) then fuse to form a eutectic, and flux the protective  $\text{Cr}_2\text{O}_3$  film from the metal surface. After the protective film has been breached, the base metal is exposed to the combined chlorine and sulfur attack. The action of the chlorine is largely catalytic (McKay and Worthington 1946) and because the metal chlorides that form have relatively high vapor pressures (Shrier 1976), chlorine is generally not detected among the oxides. Chlorine also prevents the formation of new passivating chromium phases (Speller 1951). The Ni reacts with the sulfate forming NiO and NiS. Because sulfates do not form protective films, the reactions continue until the entire base metal is consumed. Complete reaction of the bellows accounts for the presence of  $\text{Na}_2\text{SO}_4$  on the exterior and the noted loss of elastic behavior.

Examination of the sample removed from the bellows, pictured in Figure 98, revealed no general corrosion pattern. The deposits found on the bellows exterior were determined to be mixed  $\text{Na}_2\text{SO}_4$ ,  $\text{Cr}_2\text{S}_3$ , and  $\text{Fe}_2\text{O}_3$ . The results of the SEM investigation of areas A, B, and C of Figure 98 are plotted in Figure 99. Figure 99 shows nearly complete depletion of Cr and Ni in area A, nickel depletion and  $\text{Na}_2\text{SO}_4$  deposits in area B, and chromium enrichment with respect to the Fe concentration in area C. The only common feature of each of the areas analyzed was the high iron concentration. This observation also suggests sulfate attack, as the Ni and Cr will preferentially form sulfates. Also, chromium chloride is more volatile than the iron chloride (Shrier 1976), which would account for elevated Fe concentration.

#### 7.2.6 Offgas Piping

The flexible sections of offgas piping connected to the original LFCM were fabricated from various austenitic stainless steel alloys (generally 304L or 316) and provided many months of satisfactory service. These pipe sections were replaced because of mechanical damage from the removal of glass or because of entrained feed material blockages caused by corrosion.

The initial extended liquid feeding test with the rebuilt LFCM, however, resulted in rapid failure of the offgas piping. The flexible length of Type

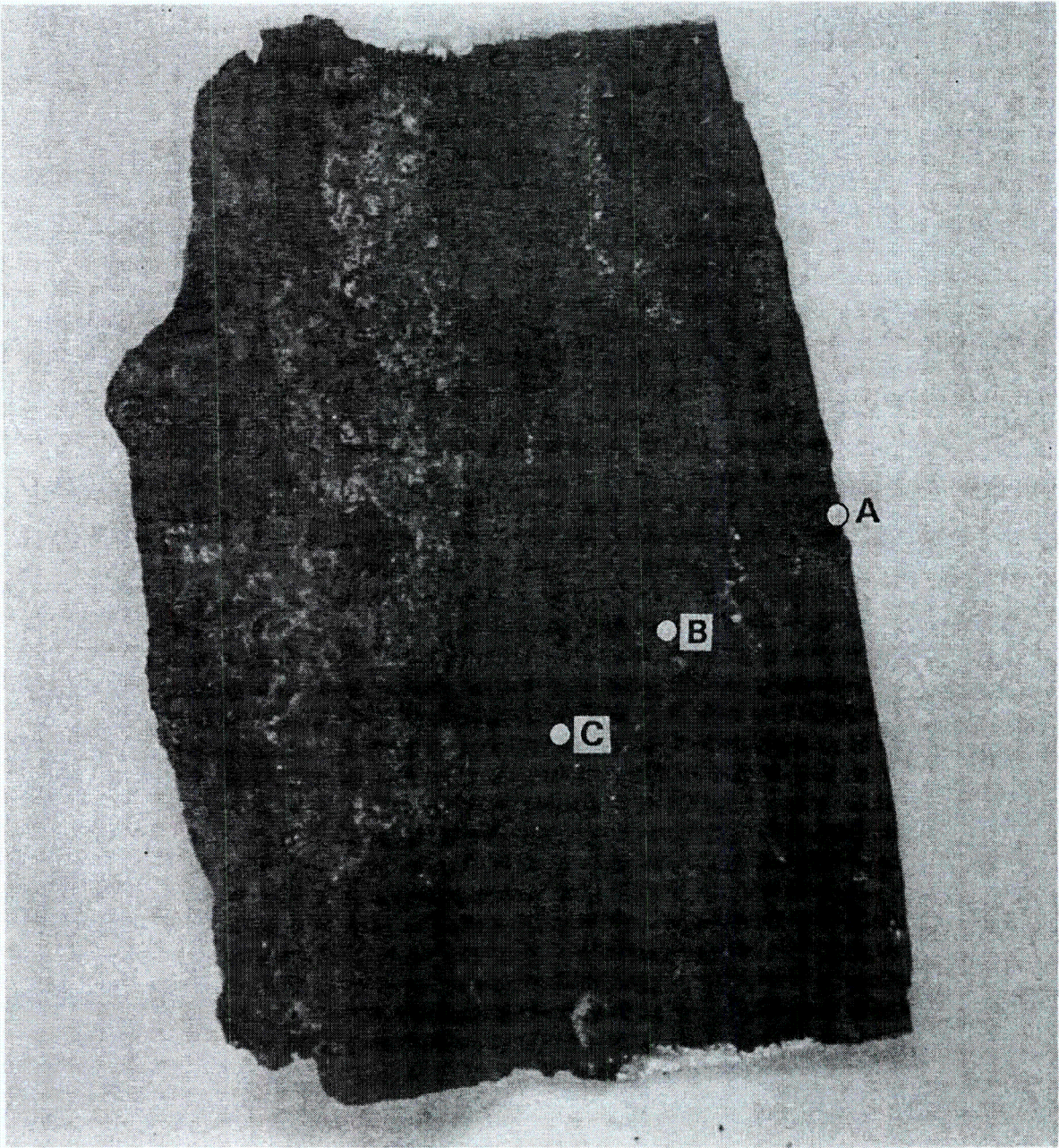


FIGURE 98. Sample of Corroded Ionic Booster Bellows

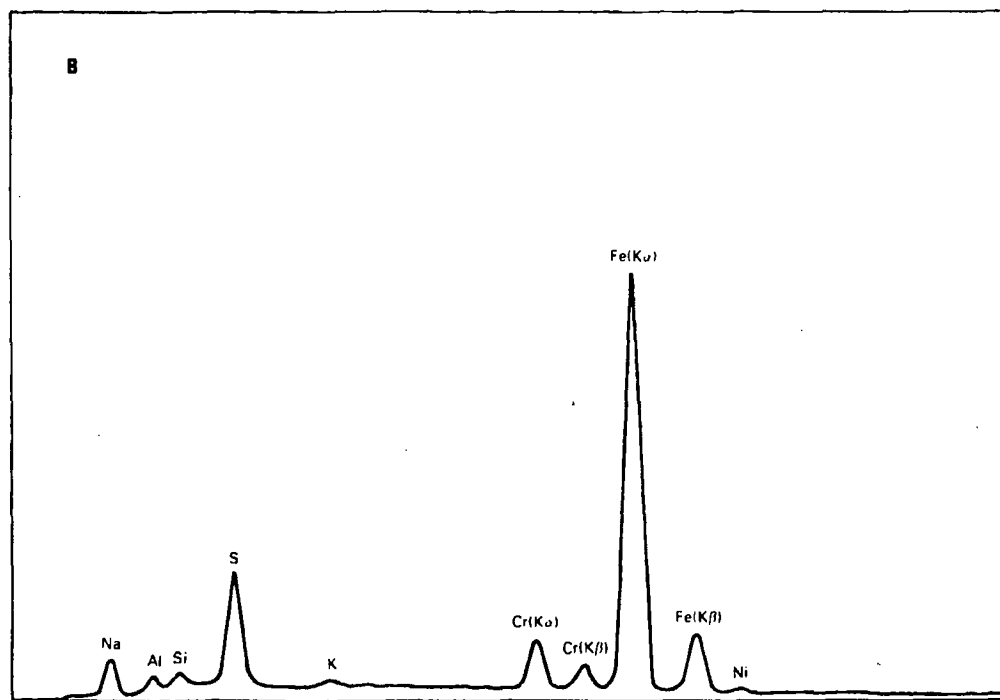
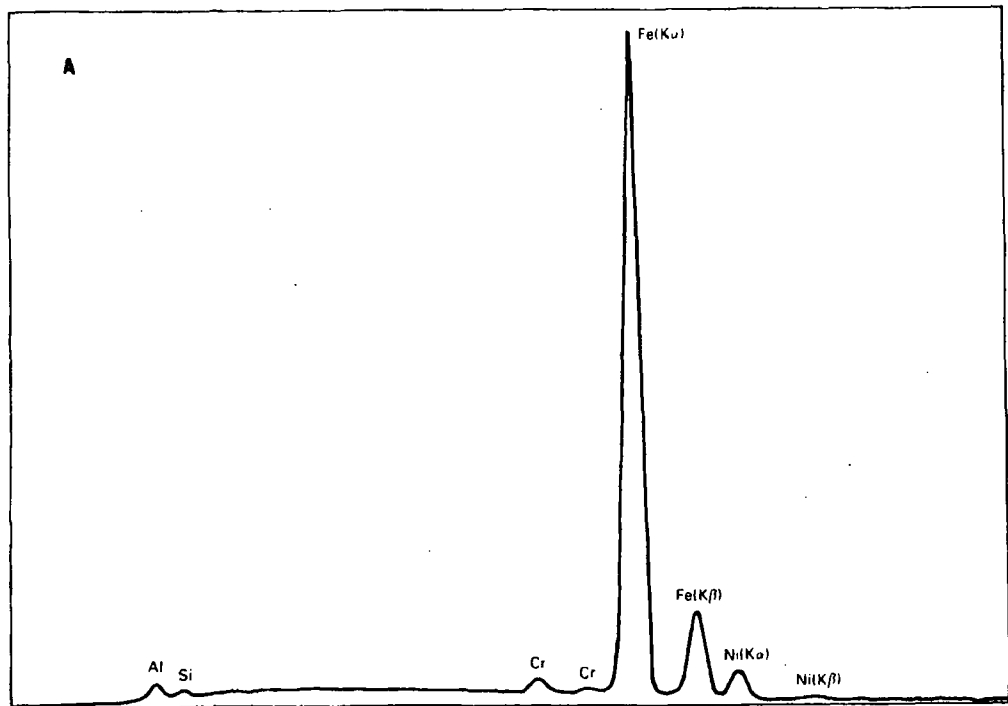


FIGURE 99. Microprobe Analysis of Areas Indicated on Figure 98

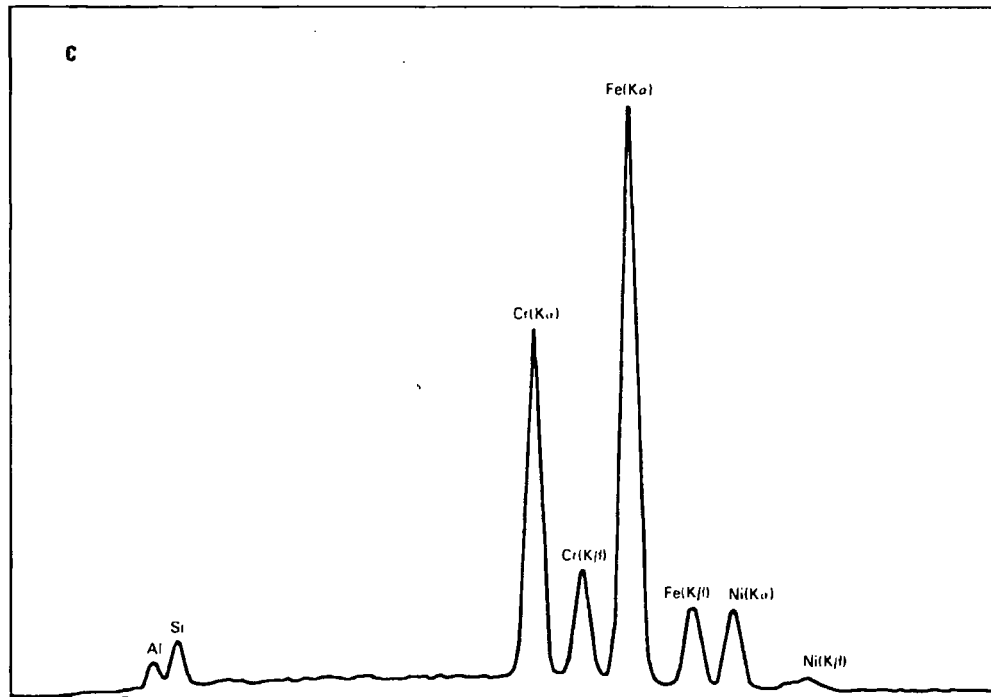


FIGURE 99. (contd)

304 stainless steel piping failed after 168 h of exposure to idling conditions and 106 h of liquid feeding. This failure was also caused by combined chlorine and sulfur attack.

The major change in operating conditions for this melting test was the use of the LFCM lid heaters to aid in evaporation of the liquid feed. This resulted in offgas temperatures ranging up to  $\sim 650^{\circ}\text{C}$  instead of the  $100^{\circ}$  to  $300^{\circ}\text{C}$  offgas temperatures of previous liquid fed tests.

Samples removed from the failed ductwork contain measurable concentration of both chlorine and sulfur. Figure 100 is a photograph of a typical section of the corroded piping. The results of the SEM analysis of regions A, B, and C of Figure 100 are presented in Figure 101. Each of these analyses show the Cr and Ni concentrations considerably enriched relative to the Fe concentration. This result is expected for the following reasons: 1) as outlined in Section 7.2.5, Cr and Ni are preferentially attacked by sulfur and chlorine, 2) under reducing conditions the exposed Fe would form  $\text{FeO}$ , and 3) thermal

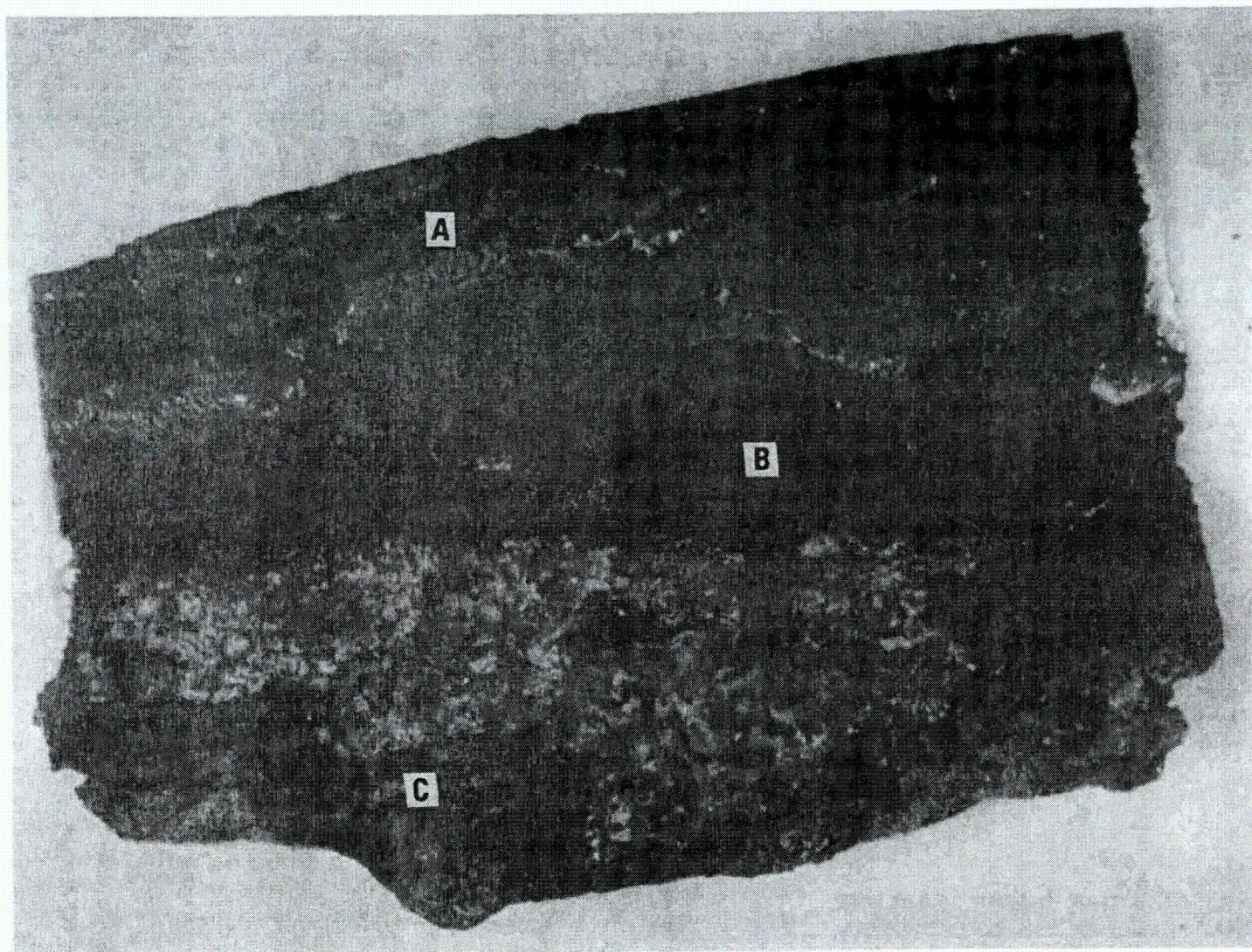
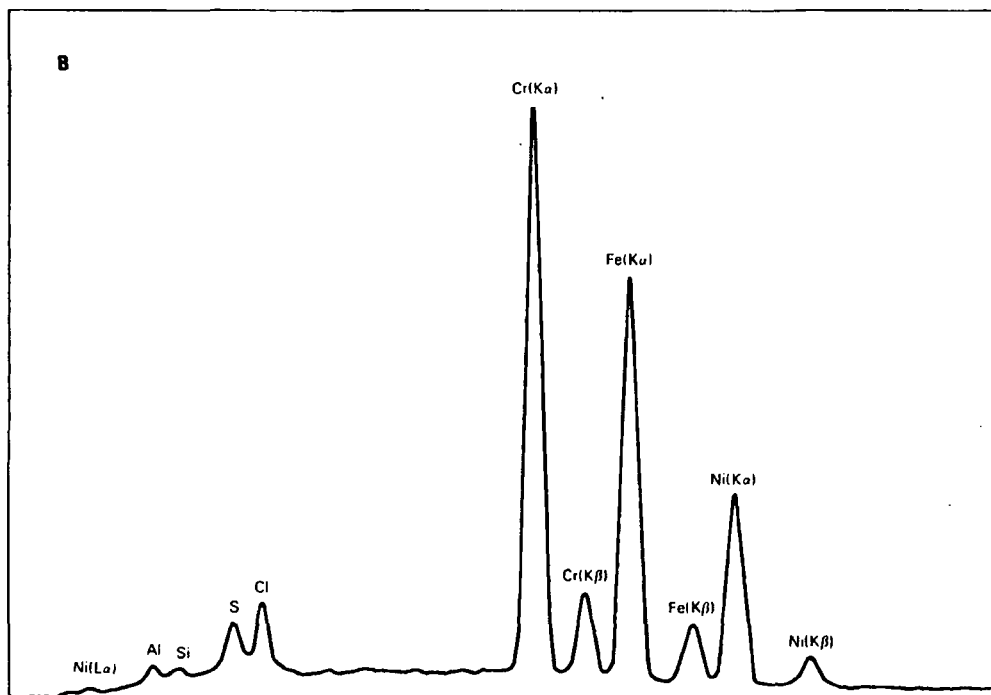
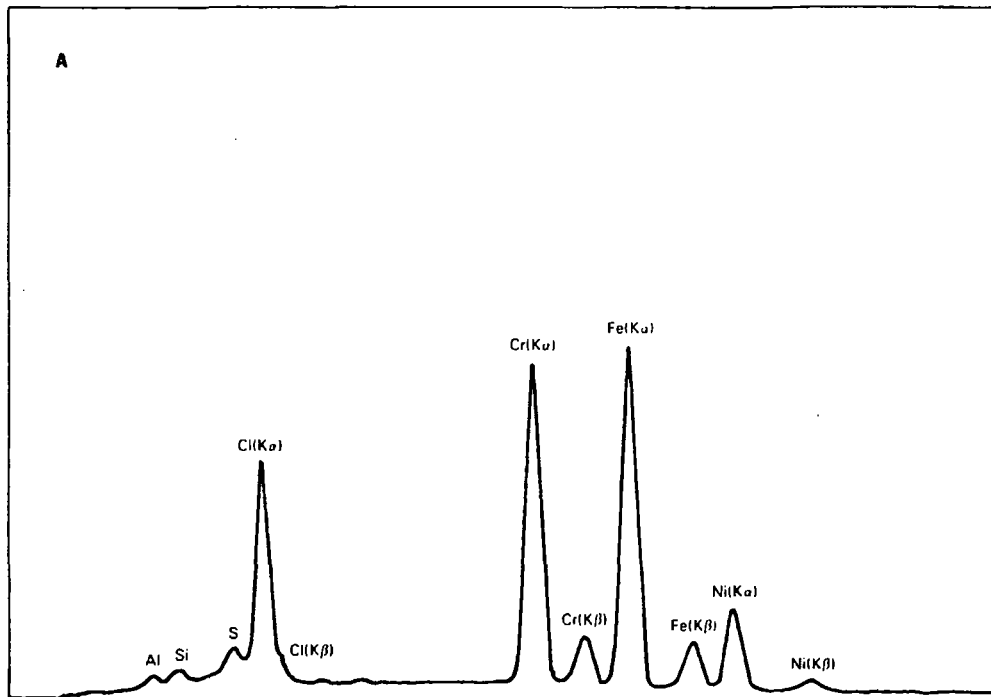


FIGURE 100. Sample of Corroded Offgas Ducting



**FIGURE 101.** Microprobe Analysis of Areas Indicated on Figure 100

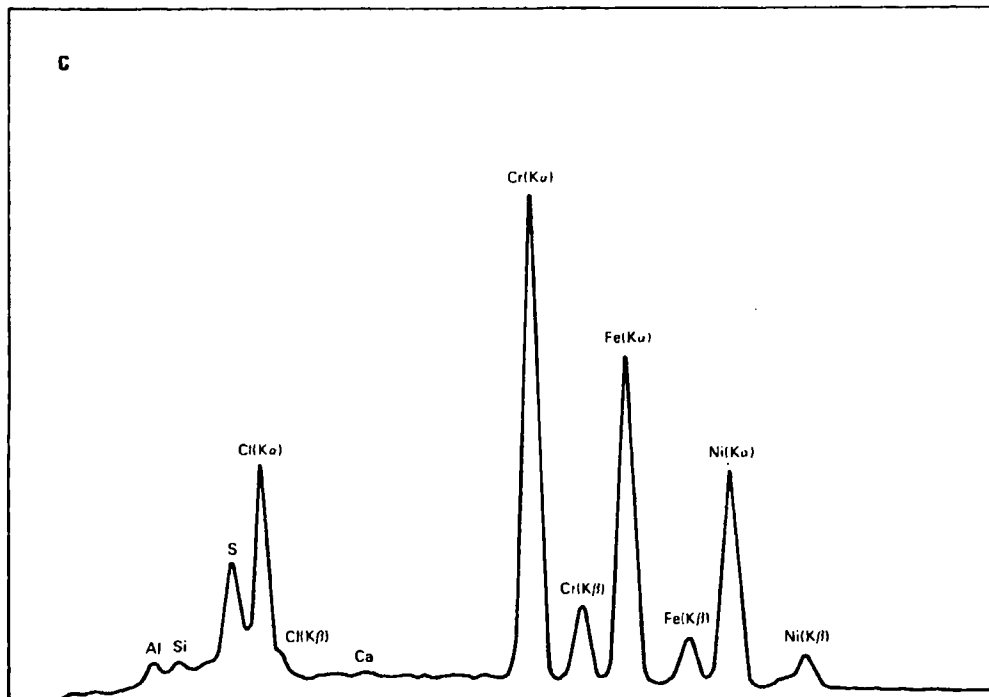


FIGURE 101. (contd)

cycling of the corroded alloy would result in spalling of the FeO because of the difference in thermal expansion coefficients between FeO and Type 304L stainless steel. The thermal expansion coefficient for 304L is 17.3 to 20.0  $\text{cm/cm}^{\circ}\text{C}$  (see Appendix A) and is 12.2  $\text{cm/cm}^{\circ}\text{C}$  for FeO (Hancock and Hurst 1974).

The corrosion mechanism for the offgas ducting is slightly different from the ionic booster bellows because the active corrosion for the former is occurring under reducing conditions. Under these conditions and the relatively high operating temperatures, nickel alloys are susceptible to accelerated sulphate attack. In this case, the  $\text{Cr}_2\text{O}_3$  layer is reduced to form  $\text{Cr}_2\text{SO}_3$ . The sulfate layer formed is less protective than the original oxide film, and tends to form globules rather than films in a corroded alloy (Kubaschewski and Hopkins 1962). This exposes the chromium-depleted region behind the original chromate layer to corrosion by sulfur and chlorine species.

The chlorine tends to react with the freshly exposed chromium metal to further inhibit the formation of a continuous passivating chromium phase.

Under reducing conditions, the nickel in the alloy reacts with sulfur to produce a  $\text{Ni}_3\text{S}_2$  eutectic. This compound melts at  $645^\circ\text{C}$  (Sedricks 1979) and is very active at the grain boundaries, exposing metal far from the metal/gas interface to corrosion. This eutectic nickel sulfide also attacks the remaining  $\text{Cr}_2\text{O}_3$  phases, producing new corrosion sites at the interface. Type 304 stainless steel is known to be prone to severe degradation under these conditions.

### 7.3 STRUCTURAL INTEGRITY

The results of the refractory stress analysis do not predict the magnitude of cracking observed in the LFCM Monofrax K-3. The discrepancy between the predicted and observed cracking is due to several factors, including unavailable refractory fracture mechanics properties, difficulty in determining the degree to which the Monofrax K-3 is restrained from free thermal expansion, and the two- versus three-dimensional modeling of the refractory.

The north and south melting cavity walls, pictured in Figures 30 and 31, are extensively cracked, yet the only stress prediction to indicate stresses above the 20,000 psi ultimate strength of the Monofrax K-3 is the stress profile of Figure 62. The low stress profiles predicted may be due to the assumed values for Young's Modulus and Poisson's ratio. Also, the effect of the operating temperature on these and other material characteristics were not considered. Inadequate data may affect not only the calculated stresses, but also the calculated stress required to cause refractory cracking.

The effect of restraining the thermal expansion of the refractory in the vertical direction can be clearly seen by comparing the predicted stress in Figure 62 to the other stresses predicted in that section. All of the other predictions are based on free vertical expansion. Clearly, with the Alfrax 66 cast above the Monofrax K-3 and the lid installed above the Alfrax 66, no vertical restraint is an invalid assumption. Although the actual degree of

restraint may be difficult to model, predictions closer to Figure 62 are probable. This would account for much of the observed cracking.

The assumption (required for the calculations performed) that the thermal gradients are constant in the third dimension is another source of error in the predicted stresses. This is especially true for stresses caused by the heated riser region calculated for the south wall. This heat source located in the middle of the south wall and above the glass level produces thermal profiles significantly different from those produced in the north wall. The most important change in the prediction from including this temperature gradient would be a change in the direction of the isotherms. With this addition, the isotherms for Cuts #1 and #2 would tend to intersect the refractory/glass interface at some vertical angle rather than parallel, as the current model predicts.

This change in the thermal profile has profound effects. This is the explanation for the destructive cracking evident on the south wall, whereas the north wall is also extensively cracked but remained intact. Norton (1949) discusses at length the tendency for refractories to propagate cracks along the directions of the principal stress when undergoing rapid cooling. The principal stresses are parallel and perpendicular to the isotherms. Therefore, the cracks in the south wall would tend to create sections of the bricks that would fall out of the wall, but the cracked brick sections would remain in position in the north wall. This effect is diagrammed in Figure 102.

Two other results are predicted by the stress analysis. The various stress predictions presume relatively high stresses in the Alfrax 66 layer around the base of the riser blocks. This accounts for the extensive cracking in this region. The analyses also predict large tensile stresses in the Zirmul layer, yet this region was found to be intact. This contradiction is due to the fact that the Zirmul layer is not continuous, but is composed of many discrete bricks. Therefore, under tensile stresses, the bricks would separate and negate the effects of the stresses.

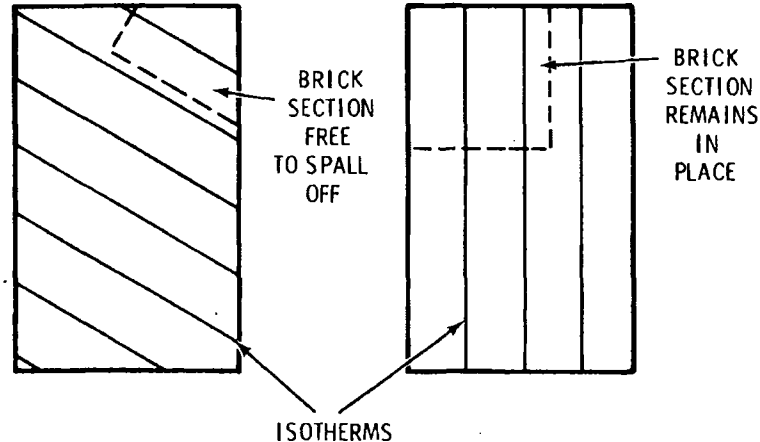


FIGURE 102. Relationship Between Isotherm Orientation and Direction of Crack Propagation

#### 7.4 COMPARISON WITH OTHER MELTER CORROSION EXPERIENCE AT PNL

This section compares the results of this investigation with published results of similar studies.

##### 7.4.1 Electrode Corrosion

Corrosion of Inconel 690 electrodes installed in the Calcine-Fed Ceramic Melter (CFCM) at PNL (Dierks et al. 1980) and in a melter at the Idaho National Engineering Laboratory (INEL) (Gombert and Dong 1980) were compared with this study. The electrodes in the CFM were reported to have demonstrated excellent overall service. These electrodes were found to exhibit slight rounding of machined edges at the metal line, but this was the only deleterious effect observed. Weld zones of these electrodes were not visually affected by the exposure to glass attack for about two years.

The electrodes of the INEL melter were reported to have experienced more severe attack than was observed in the LFCM. These electrodes were reported to demonstrate a 0.88 mm/mo metal loss. The higher corrosion rate of the electrodes is probably due to several differences in operating procedures such as using glasses with different wastes and higher waste loadings, higher electrode current density ( $0.62 \text{ A/cm}^2$  compared with typical idling current density of  $0.34 \text{ A/cm}^2$  for the LFCM primary electrodes), higher operating

temperatures (1100°C compared to the LFCM limit of 1050°C), and several complete operating to ambient temperature cycles that may have caused spalling of the protective film produced on the electrode faces. Each of these variables could increase the electrode corrosion rate. This report describes a similar corrosion mechanism as detected in the LFCM.

#### 7.4.2 Metals Exposed to Glass Vapor Attack

Dierks et al. (1980) reports corrosion of the CFCM Inconel 601 lid by sulfur and chlorine. Examination of the photomicrographs of the corroded Inconel 601 lid reveals similar corrosive action as detected in the LFCM ionic booster bellows. The corrosion photomicrographs show classic sulfidation. The chromium present at the outer edge of the corroded specimen indicates that a protective film existed at some time. The metal behind the outer layer was depleted in Cr and was readily attacked by the sulfur. The most important feature of the micrographs is the Ni and Fe zones in the corroded zone with no sulfur present. This indicates that this is likely a spinel ( $\text{NiFe}_2\text{O}_4$ ) and therefore shows oxidative attack.

The lid of the LFCM does not show signs of this corrosion mechanism, nor does the riser plate. This is because the LFCM lid was insulated on the outside, whereas the CFCM was internally insulated. Therefore, during idling the LFCM lid operated at  $\sim 900^\circ\text{C}$ , which is too hot for significant sulfide attack. Conversely, certain locations on the CFCM lid were at temperatures that promoted sulfide corrosion.

#### 7.4.3 Refractories

Two major differences between the condition of the Monofrax K-3 in the LFCM and CFCM are immediately apparent. The first is the extent to which the LFCM refractory was cracked. Only minor cracking was observed in the CFCM.

Varying construction and operational procedures may account for this difference. The Monofrax K-3 blocks in the CFCM design were not restricted from expanding vertically. The stress analysis section of this report shows the low refractory stresses created with this design concept. Another construction difference between the melters is the course of Zirmul blocks in the

walls of the CFCM. This additional layer of insulation would have produced smaller thermal gradients in the Monofrax K-3, which would lead to reduced cracking.

Two major differences in the operating histories of the melter would also produce lower refractory stresses in the CFCM and thereby cracking. The simulated HLW was always added to the CFCM as a calcined product. Thus the CFCM was not subjected to the thermal shock of liquid-feeding initiation. The second operational difference was the respective melter startups. The CFCM was heated to operating temperature over a period of approximately 75 h compared to roughly 22 h for the LFCM. This also would produce lower thermal stresses in the CFCM refractories.

The other major difference in the melter conditions is the extent that the CFCM bricks were corroded compared to those the LFCM. The CFCM was severely corroded in the region of the riser drain inlet nozzle, and the Monofrax K-3 was generally corroded to a greater extent than the LFCM. The CFCM riser was corroded by a mechanism known as upward drilling (Dierks et al. 1980). Because the LFCM rise design was based on an inclined riser inlet, no surface that could trap gas bubbles was present; therefore, upward drilling corrosion was precluded.

Although the respective analyses have shown similar mechanisms for the dissolution of the Monofrax K-3, the CFCM displayed considerably more general corrosion of the glass-contact faces. This is almost certainly due to the period that the CFCM was operated with  $>1200^{\circ}\text{C}$  glass temperatures. At this elevated temperature, the protective spinel layer that forms on the bricks would be removed by convective glass motion and enhanced Monofrax K-3 dissolution would be expected.

The CFCM examination document also indicated good resistance to glass attack by the Zirmul and Alfrax 66 refractories. The CFCM design also used Zirmul as the refractory installed behind the Monofrax K-3 and no major corrosion was reported. The Alfrax 66 cast in the CFCM contained much less cracking than it did in the LFCM. This is probably the result of the more conservative melter startup procedure of the CFCM described above.



## 8.0 REFERENCES

- Blair, H. T., and I. M. Lukacs. 1980. Investigation of Foaming During Nuclear Defense-Waste Solidification by Electric Melting. PNL-3552, Pacific Northwest Laboratory, Richland, Washington.
- Brouns, R. A., et al. 1980. Immobilization of High Level Defense Waste in a Slurry-Fed Electric Glass Melter. PNL-3372, Pacific Northwest Laboratory, Richland, Washington.
- Buelt, J. L., and C. C. Chapman. 1978. Liquid-Fed Ceramic Melter: A General Description Report. PNL-2735, Pacific Northwest Laboratory, Richland, Washington.
- Buelt, J. L., and C. C. Chapman. 1979. Slurry Feeding of Nuclear Waste to an Electric Glass Melter. PNL-SA-7571, Pacific Northwest Laboratory, Richland, Washington.
- Buelt, J. L., et al. 1979. A Review of Continuous Ceramic-Lined Melters and Associated Experience at PNL. PNL-SA-7590, Pacific Northwest Laboratory, Richland, Washington.
- Carborundum Company. 1980. "Advanced Refractories--A Complete Spectrum of High-Performance Materials." Carborundum Company Form A-2380.
- Chan, W. Y., and P. S. Nicholson. 1978. "Effects of Glassy Phase on the Thermal Cycling Resistance of Fusion Cast Refractories." Ceramic Bulletin, Vol. 57, No. 2.
- Chapman, C. C., et al. 1979. Vitrification of Hanford Wastes in a Joule-Heated Ceramic Melter and Evaluation of Result and Canisterized Product. PNL-2904, Pacific Northwest Laboratory, Richland, Washington.
- Cowan, R. L., II, and C. S. Tedmon, Jr. 1973. "Intergranular Corrosion of Iron-Nickel-Chromium Alloys." In Advances in Corrosion Science and Technology, Vol. 3, eds. M. G. Fontana and R. W. Staehle, Plenum Press, New York.
- Dierks, R. D. 1980. The Design and Performance of a 100-kg/h, Direct Calcine-Fed Electric-Melter System for Nuclear-Waste Vitrification. PNL-3387, Pacific Northwest Laboratory, Richland, Washington.
- Dierks, R. D., et al. 1980. Investigation of Corrosion Experienced in a Spray Calciner/Ceramic Melter System. PNL-3406, Pacific Northwest Laboratory, Richland, Washington.

- Donachie, M. J., Jr., et al. 1967. "Sulfidation of Hot Section Alloys in Gas Turbine Engines." In Hot Corrosion Problems Associated with Gas Turbines, ASTM STP 421, ASTM, Philadelphia, Pennsylvania.
- Fontana, M. G., and N. B. Greene. 1978. Corrosion Engineering, 2nd ed. McGraw-Hill, New York.
- Gombert, D., and M. Y. Dong. 1980. Operation of a Laboratory-Scale Glass Melter to Vitrify ICPP Zirconia Calciner. ENICO-1050.
- Hancock, P. and R. C. Hurst. 1974. "The Mechanical Properties and Breakdown of Surface Films at Elevated Temperatures." In Advances in Corrosion Science and Technology, Vol. 4, eds. M. G. Fontana and R. W. Staehle, Plenum Press, New York.
- Hjelm, R. L., and T. E. Donovan. 1979. Numerical Modeling of Liquid Feeding in the Liquid-Fed Ceramic Melter. PNL-3137, Pacific Northwest Laboratory, Richland, Washington.
- Kroger, J. W. 1974. "Chromium Depletion and Void Formation in Fe-Ni-Cr Alloys During Molten Salt Corrosion and Related Processes." In Advances in Corrosion Science and Technology, Vol. 4, eds. M. G. Fontana and R. W. Staehle, Plenum Press, New York.
- Kubaschewski, D., and B. E. Hopkins. 1962. Oxidation of Metals and Alloys, 2nd ed., Academic Press, New York.
- McKay, R. J., and R. W. Worthington. 1946. Corrosion Resistance of Metals and Alloys. Reinhold, New York.
- Norton, F. H. 1949. Refractories. McGraw-Hill, New York.
- Quigley, M. S., and D. K. Kreid. 1979. Physical Modeling of Joule-Heated Ceramic Melters of High-Level Waste Immobilization. PNL-2809, Pacific Northwest Laboratory, Richland, Washington.
- Sedricks, A. J. 1979. Corrosion of Stainless Steel. Wiley, New York.
- Shrier, L. L. 1976. Corrosion, 2nd ed., Newness-Butterworths, Boston.
- Speller, F. N. 1951. Corrosion, Causes and Prevention, 3rd ed., McGraw-Hill, New York.
- Van Vlack, L. M. 1964. Physical Ceramics for Engineers. Addison Wesley, Reading, Massachusetts.

APPENDIX A

LFCM CONSTRUCTION MATERIALS,  
COMPOSITIONS, AND PROPERTIES

TABLE A.1. Composition of LFCM Construction Materials

Element	Oxide	Alfracx 66	Typical Incone] 601, wt%(a)	Typical Incone] 690, wt%(a)	Typical 316 SS wt%(a)	Typical 321 SS wt%(a)	Typical 304L SS wt%(a)	Monofrax K-3, wt%	Duraboard	Zirmul Refractory, wt%
Al	Al <sub>2</sub> O <sub>3</sub>	96	0.48	0.25	---	---	---	44.0	51.7	70.0
C	CaO	4	0.15	---	---	---	---	0.18	---	---
B	B <sub>2</sub> O <sub>3</sub>	---	---	---	---	---	---	---	0.15	---
Cr	Cr <sub>2</sub> O <sub>3</sub>	0.1	16.8	30.0	16-18	17-19	18-20	19.0	Trace	---
Fe	Fe <sub>2</sub> O <sub>3</sub>	---	14.1	9.5	Balance	Balance	Balance	5.85	---	---
Li	Li <sub>2</sub> O	---	---	---	---	---	---	---	0.3	---
Na	Na <sub>2</sub> O	---	---	---	---	---	---	0.20	---	---
Ni	NiO	---	60.0	60.0	10-14	9-12	8-12	---	---	---
Mn	MnO <sub>2</sub>	---	0.20	---	2.0	2.0	2.0	0.06	---	---
Mg	MgO	Trace	---	---	---	---	---	3.71	47.6	---
Si	SiO <sub>2</sub>	---	0.16	---	1.0	1.0	1.0	0.60	---	10.2
Ti	TiO <sub>2</sub>	---	0.34	0.25	---	---	---	0.16	---	---
Zn		---	0.20	---	---	---	---	---	---	---
P		---	---	---	0.045	0.045	0.045	---	---	---
S	Na <sub>2</sub> SO <sub>4</sub>	---	---	---	0.03	0.03	0.03	---	---	---
Mo		---	---	---	2-3	3-4	---	---	---	---
Cu		---	0.30	---	---	---	---	---	---	---
C		---	0.03	0.03	0.08	0.08	0.03	---	---	---
Zr	ZrO <sub>2</sub>	---	---	---	---	---	---	---	---	19.5
Total		---	92.7	100.03	---	---	---	71.8	---	99.8

(a) Metallic wt%.

TABLE A.2. Properties of the LFCM Construction Materials

	Density, g/cc	Porosity, %	Thermal Expansion, cm/cm <sup>o</sup> K			Thermal Conductivity, W/m <sup>o</sup> K			Electrical Resistivity, -cm		
			100 <sup>o</sup> C	500 <sup>o</sup> C <small>x 10<sup>6</sup></small>	1000 <sup>o</sup> C	100 <sup>o</sup> C	500 <sup>o</sup> C	1000 <sup>o</sup> C	100 <sup>o</sup> C	500 <sup>o</sup> C	1000 <sup>o</sup> C
Monofrax K-3	3.9	4	5	6.2	10.0	4.19	3.77	3.69	---	20,000	300
Alfrax 66	2.72	---(a)	8	8	8	0.26	0.19	0.16	---	---	3000
Zirmul	3.14	10-15 <sup>(a)</sup>	5	6	7	0.20	0.18	0.17	10,000	10,000	10,000
Duraboard	0.46	86							---	---	
Inconel 690	8.19	0	14.1	15.2	17.4	13.5	21.0	30.1	1.16 x 10 <sup>-4</sup>	1.24 x 10 <sup>-4</sup>	1.27 x 10 <sup>-4</sup>
Inconel 601		0	13.8	15.2	17.8	12.7	19.5	27.8	1.23 x 10 <sup>-4</sup>	1.20 x 10 <sup>-4</sup>	1.30 x 10 <sup>-4</sup>
Stainless Steel 304L	7.34	0	17.3	18.4	20.0 <sup>(b)</sup>	15.5	22.5	32.0 <sup>(b)</sup>	0.79 x 10 <sup>-4</sup>	1.06 x 10 <sup>-4</sup>	1.25 x 10 <sup>-4</sup>

(a) Alfrax 66 is a castable refractory, therefore porosity will vary from application to application.

(b) Extrapolated value.

APPENDIX B

LFCM RUN SUMMARY

LFCM RUN SUMMARY (1)

Run No.	Date	Feed		Glass Poured, kg	Duration of Run
		Composition	Amount		
	2/9/77	Cullet	815 kg		Startup
	2/9/77	NaOH	45 kg		Startup
	2/11/77	Cullet	442 kg		
	3/8/77	76-101 4% Na and 4% Ca (see Run 1)	45 kg		45 kg Test Run
1	3/10/77	76-101 Premelted Frit, wt% :	74 kg		Run Aborted, Feeder Failure
		SiO <sub>2</sub> 54.9	} 92 wt%		
		B <sub>2</sub> O <sub>3</sub> 13.1			
		Na <sub>2</sub> O 10.3			
		ZnO 6.85			
		CaO 2.76			
		TiO <sub>2</sub> 4.09			
		<u>Additives, wt%</u>			
		Na <sub>2</sub> O(Na <sub>2</sub> CO <sub>3</sub> ) 4.0			
		CaO(CaO <sub>3</sub> ) 4.0			
	3/15/77	76-101 Frit +4% Na, +4% Ca (see Run 1)	~91 kg		33 kg, Tilt Pouring Test
	3/16/77	76-101 + 4% Na + 4% Ca (see Run 1)			
	3/18/77		---	} 22 kg	
	3/29/77		---		
2	4/8/77	76-101 Premelted Frit, wt% :	366 kg--Remainder in the Feeder		205 kg
		SiO <sub>2</sub> 32.7	} 54.8 wt%		
		B <sub>2</sub> O <sub>3</sub> 7.78			
		Na <sub>2</sub> O 6.14			
		ZnO 4.08			
		CaO 1.64			
		TiO <sub>2</sub> 2.44			

B.1

LFCM RUN SUMMARY (2)

<u>Run No.</u>	<u>Date</u>	<u>Composition</u>	<u>Amount</u>	<u>Glass Poured, kg</u>	<u>Duration of Run</u>
2 (contd)		<u>Additives, wt%</u>			
		B <sub>2</sub> O <sub>3</sub> (H <sub>3</sub> BO <sub>3</sub> )	13.8	} 20.2 wt%	
		CaO (lime)	3.45		
		Na <sub>2</sub> O(NaNO <sub>3</sub> )	2.99		
		<u>PW-4b Synthetic, wt%</u>			
		P <sub>2</sub> O <sub>5</sub> (Na <sub>3</sub> PO <sub>4</sub> ·12H <sub>2</sub> O?)	0.45	} 25 wt%	
		K <sub>2</sub> O	1.05		
		Cr <sub>2</sub> O <sub>3</sub>	0.24		
		Fe <sub>2</sub> O <sub>3</sub>	2.27		
		Co <sub>2</sub> O <sub>3</sub>	0.22		
		NiO	0.72		
		SrO(Sr(NO <sub>3</sub> ) <sub>2</sub> )	0.73		
		ZrO <sub>2</sub>	3.56		
		MoO <sub>3</sub>	4.41		
		CdO	0.07		
		TeO <sub>2</sub>	0.50		
		BaO	1.08		
		RE <sub>2</sub> O <sub>3</sub>	9.80		
	4/12/77	See Run 2	Remainder in Feeder	93 kg	
3	4/22/77	<u>1M HNO<sub>3</sub> Liquid Slurry @ 378 L/MTU</u>	195 L	~363 kg ?	
		<u>76-101 Premelted Frit, wt%</u>	50 L/h		
		SiO <sub>2</sub>	33.1	} 75 wt%	
		B <sub>2</sub> O <sub>3</sub>	7.88		
		Na <sub>2</sub> O	6.21		
		ZnO	4.13		
		CaO	1.66		
		TiO <sub>2</sub>	2.47		
		<u>Additives, wt%</u>			
		B <sub>2</sub> O <sub>3</sub> (H <sub>3</sub> BO <sub>3</sub> )	13.7		
		CaO (lime)	3.0		
		Na <sub>2</sub> O(NaNO <sub>3</sub> )	3.0		

B.2

### LFCM RUN SUMMARY (3)

Run No.	Date	Feed		Glass Poured, kg	Duration of Run
		Composition	Amount		
3 (contd)		<u>PW-4b Waste</u>			
		<u>PW-0</u>	<u>wt%</u>		
		Ag <sub>2</sub> O(AgNO <sub>3</sub> )	0.06	} 25 wt%	
		BaO(Ba(NO <sub>3</sub> ) <sub>2</sub> )	1.02		
		CdO(Cd(NO <sub>3</sub> ) <sub>2</sub> ·4H <sub>2</sub> O)	0.06		
		CoO(Co(NO <sub>3</sub> ) <sub>2</sub> ·6H <sub>2</sub> O)	0.20		
		Cr <sub>2</sub> O <sub>3</sub> (Cr(NO <sub>3</sub> ) <sub>3</sub> ·9H <sub>2</sub> O)	0.23		
		Fe <sub>2</sub> O <sub>3</sub> (Fe(NO <sub>3</sub> ) <sub>3</sub> ·9H <sub>2</sub> O)	2.14		
		K <sub>2</sub> O(KNO <sub>3</sub> )	0.74		
		Na <sub>2</sub> O(NaNO <sub>3</sub> )	0		
		NiO(Ni(NO <sub>3</sub> ) <sub>2</sub> ·6H <sub>2</sub> O)	0.68		
		SrO(Sr(NO <sub>3</sub> ) <sub>2</sub> )	0.69		
		ZrO <sub>2</sub> (ZrO(NO <sub>3</sub> ) <sub>2</sub> ·2H <sub>2</sub> O)	3.22		
		Ce <sub>2</sub> O <sub>3</sub>	2.45		
		RE <sub>2</sub> O <sub>3</sub>	6.86		
		MoO <sub>3</sub>	4.08		
		Te <sub>2</sub> O	0.45		
		P <sub>2</sub> O <sub>3</sub> (12.1M H <sub>3</sub> PO <sub>4</sub> )	0.40		
		K <sub>2</sub> O(KNO <sub>3</sub> )	1.16		
4	4/26/77	<u>1M HNO<sub>3</sub> Slurry @ 378 L/MTU</u>		~140 L @ 117 L/h	34 kg
		<u>Frit, wt%</u>			
		76-101 Premelted Frit	58.1	} 79 wt%	
		B <sub>2</sub> O <sub>3</sub> (H <sub>3</sub> BO <sub>2</sub> )	14.4		
		CaO (lime)	3.14		
		Na <sub>2</sub> O(NaNO <sub>3</sub> )	3.14		
		<u>Waste, wt%</u>			
		PW-0	20.6	} 21 wt%	
		TeO <sub>2</sub>	0.43		
		P <sub>2</sub> O <sub>5</sub> (12.1M H <sub>3</sub> PO <sub>4</sub> )	0.38		

LFCM RUN SUMMARY (4)

Run No.	Date	Feed		Glass Poured, kg	Duration of Run
		Composition	Amount		
5	5/3/77	PW-4b Calcine and Frit (see Run 2)	183 kg--Remainder in Feeder	~227 kg	
	5/13/77	PW-4b Calcine and Frit (see Run 2 + about 75 lb Cullet)	Remainder in Feeder + ~34 kg	None	
	5/14/77	---	---	Demonstration for Vienna TV ~32 kg?	
6	5/18/77	<u>1M HNO<sub>3</sub> Slurry</u>	~500 L @ 100 L/H	~200 kg	5 h
		<u>Frit, wt%</u>			
		SiO <sub>2</sub>	32.3	} 76 wt%	
		Na <sub>2</sub> O(NaNO <sub>3</sub> )	11.8		
		B <sub>2</sub> O <sub>3</sub> (H <sub>3</sub> BO <sub>3</sub> )	21.1		
		ZnO	4.03		
		TiO <sub>2</sub>	2.41		
		<u>Waste, wt%</u>			
		PW-0	22.9	} 24 wt%	
		TeO <sub>2</sub>	0.48		
P <sub>2</sub> O <sub>5</sub> (12.1M H <sub>3</sub> PO <sub>4</sub> )	0.42				
5/27/77	76-101 + NaNO <sub>3</sub> + H <sub>3</sub> BO <sub>3</sub> + CaO (see Run 2) + PW-7a Calcine	~54 kg	None		
6/1/77	76-101 + NaNO <sub>3</sub> + H <sub>3</sub> BO <sub>3</sub> + CaO (see Run 2) + PW-7a Calcine	~45 kg	~5 kg		
6/6/77	76-101 + NaNO <sub>3</sub> + H <sub>3</sub> BO <sub>3</sub> + CaO (see Run 2) + PW-7a Calcine	~45 kg			
7	6/8/77	<u>1M HNO<sub>3</sub> Liquid Slurry</u> (see Run 6)	420 L @ 84 L/h	~136 kg	5 h
	6/17/77	76-101 + NaNO <sub>3</sub> + H <sub>3</sub> BO <sub>3</sub> + CaO (see Run 2) + PW-7a Calcine	~23 kg		1/2 h
	6/18/77			9 kg	
	6/21/77	76-101 + NaNO <sub>3</sub> + H <sub>3</sub> BO <sub>3</sub> + CaO (see Run 2) + PW-7a Calcine	~14 kg	9 kg	

B.4

LFCM RUN SUMMARY (5)

Run No.	Date	Feed		Glass Poured, kg	Duration of Run	
		Composition	Amount			
1-H	7/7/77	Hanford Waste With Radionuclide Removal-- Chemical Form Undefined		454 kg @ 220 lb/h	454 kg	4-1/2 h
		<u>Glass, wt</u>	<u>Composition, wt%</u>	<u>Glass Formers, wt%</u>		
		CeO <sub>3</sub> 1.0	Fe <sub>2</sub> O <sub>3</sub> 4.1	SiO <sub>2</sub> 47.53		
		P <sub>2</sub> O <sub>5</sub> 1.99	Ni <sub>2</sub> O <sub>3</sub> 0.82	B <sub>2</sub> O <sub>3</sub> 9.92		
		Bi <sub>2</sub> O <sub>5</sub> 1.17	Cr <sub>2</sub> O <sub>3</sub> 0.47			
		MnO <sub>2</sub> 0.70	SrO 2.58			
		TiO <sub>2</sub> 0.23	CaO 0.70			
		Al <sub>2</sub> O <sub>3</sub> 8.20	Na <sub>2</sub> O 16.29			
2-H	7/11-7/15	Hanford Waste With Radionuclide Removal (see Run 1-h)		8765 kg @ 93 kg/h	6804 kg	86 h
	7/26/77-7/29/77	Hanford Waste With Radionuclide Removal		545 kg @	~45 kg	
3-H	8/1/77-8/2/77	Hanford Waste Without Radionuclide Removal		~499 kg @ ~32 kg/h	531 kg	15 h
		SiO <sub>2</sub>	55.0	CaO	0.73	
		Na <sub>2</sub> O(NaNO <sub>3</sub> )	20.0	Cr <sub>2</sub> O <sub>3</sub>	0.13	
		B <sub>2</sub> O <sub>3</sub>	7.0	Fe <sub>2</sub> O <sub>3</sub>	0.25	
		Al <sub>2</sub> O <sub>3</sub> (Al(OH) <sub>3</sub> )	6.3	CeO	0.08	
		Li <sub>2</sub> O	4.25	MnO <sub>2</sub>	0.08	
		TiO <sub>2</sub>	4.25	Ni <sub>2</sub> O <sub>3</sub>	0.08	
		P <sub>2</sub> O <sub>5</sub> (Na <sub>3</sub> PO <sub>4</sub> 12H <sub>2</sub> O)	1.7	ZrO <sub>2</sub>	0.08	
	8/11/77	Hanford Waste w/o RR (see Run 3-H)		~91 kg	---	2 h
DLF-8	8/15/77	1M HNO <sub>3</sub> Liquid Slurry (see Run 6)		731 L @ 73 L/h	103 kg	10 h
	8/19/77	Hanford Waste w/o RR (see Run 3-H)		~91 kg	Very Little	?
	8/22-9/1	Savannah River Waste		2455 kg @ 22 kg/h	2280 kg	113 h

B.5

LFCM RUN SUMMARY (6)

Run No.	Date	Feed		Glass Poured, kg	Duration of Run
		Composition	Amount		
DLF-8 (contd)		Calcine, wt%	Frit (Pre-melted), wt%		
		Fe <sub>2</sub> O <sub>3</sub> 13.47	SiO <sub>2</sub> 38.1		
		Al <sub>2</sub> O <sub>3</sub> 7.97	Na <sub>2</sub> O 2.0		
		MnO <sub>2</sub> 3.59	B <sub>2</sub> O <sub>3</sub> 7.25		
		NiO(NiCO <sub>3</sub> ) 1.57	TiO <sub>2</sub> 7.25		
		CaO(CaCO <sub>3</sub> ) 0.9	Li <sub>2</sub> O 2.9		
		Na <sub>2</sub> O(Na <sub>2</sub> CO <sub>3</sub> ) 11.4	CaO 3.6		
	SRL-2	9/8/77	Savannah River Waste	399 kg	241 kg
		Calcine, wt%	Frit (Unreacted), wt%		
		Fe <sub>2</sub> O <sub>3</sub> 13.47	SiO <sub>2</sub> 38.1		
		Al <sub>2</sub> O <sub>3</sub> 7.97	Na <sub>2</sub> O(Na <sub>2</sub> CO <sub>3</sub> ) 2.0		
		MnO <sub>2</sub> 3.59	B <sub>2</sub> O <sub>3</sub> (H <sub>3</sub> BO <sub>3</sub> ) 7.25		
		NiO 1.57	TiO <sub>2</sub> 7.25		
		CaO(CaCO <sub>3</sub> ) 0.9	Li <sub>2</sub> O(LiOH·H <sub>2</sub> O) 2.9		
		Na <sub>2</sub> O(Na <sub>2</sub> CO <sub>3</sub> ) 11.4	CaO(CaCO <sub>3</sub> ) 3.6		
	10/5/77	76-199 Frit (see Run LF-11)	91 kg	98 kg	---
DLF-9	10/6/77	132 lb of Savannah River Waste (see Run SRL-1) + 18 L of 55.5 wt% HNO <sub>3</sub> + Water for Every 100 L of Liquid Feed	190 L @ 114 L/h	147 lb	1 h, 40 min
DLF-10	10/10/77	Composition of DLF-9, Except the Last 110 L had 9.1 L of 55.5 wt% HNO <sub>3</sub> Added to Every 100 L of Feed, for a 1M HNO <sub>3</sub> Solution	273 L @ 67 L/h	None	4.1 h
	10/11/77	---	---	85 kg	---
	10/12/77	---	---	16 kg	---
	10/13/77	---	---	10 kg	---
	10/25/77	76-199 Frit	45 kg	65 kg	---

B.6

LFCM RUN SUMMARY (7)

Run No.	Date	Feed		Glass Poured, kg	Duration of Run
		Composition	Amount		
LF-11	11/2/77	2M HNO <sub>3</sub> Liquid Slurry of PW-7a Waste and Mesh 76-199 Frit	81 L @ 54 L/h	None	1.5 h
		76-199 Premelted Frit			
		<u>Oxide</u>	<u>wt%</u>		
		SiO <sub>2</sub>	35.4	} 67 wt%	
		B <sub>2</sub> O <sub>3</sub>	9.3		
		TiO <sub>2</sub>	6.0		
		Al <sub>2</sub> O <sub>3</sub>	1.0		
		Na <sub>2</sub> O	8.0		
		K <sub>2</sub> O	2.0		
		CaO	2.0		
		CuO	3.0		
		<u>PW-7a Liquid Waste</u>			
		<u>PW-0 + PW-7a-2m</u>	<u>wt%</u>		
		Ag <sub>2</sub> O(AgNO <sub>3</sub> )	0.04	} 33 wt%	
		BaO(Ba(NO <sub>3</sub> ) <sub>2</sub> )	0.76		
		CdO(Cd(NO <sub>3</sub> ) <sub>2</sub> ·4H <sub>2</sub> O)	0.05		
		CoO(Co(NO <sub>3</sub> ) <sub>2</sub> ·6H <sub>2</sub> O)	0.14		
		Cr <sub>2</sub> O <sub>3</sub> (Cr(NO <sub>3</sub> ) <sub>3</sub> ·9H <sub>2</sub> O)	0.17		
		Fe <sub>2</sub> O <sub>3</sub> (Fe(NO <sub>3</sub> ) <sub>3</sub> ·9H <sub>2</sub> O)	2.38		
		K <sub>2</sub> O(KNO <sub>3</sub> )	0.55		
		Na <sub>2</sub> O(NaNO <sub>3</sub> )	3.33		
		NiO(Ni(NO <sub>3</sub> ) <sub>2</sub> ·6H <sub>2</sub> O)	0.50		
		SrO(Sr(NO <sub>3</sub> ) <sub>2</sub> )	0.51		
		ZrO <sub>2</sub> (ZrO(NO <sub>3</sub> ) <sub>2</sub> ·2H <sub>2</sub> O)	3.01		
		Ce <sub>2</sub> O <sub>3</sub>	4.97		
		RE <sub>2</sub> O <sub>3</sub>	10.28		
		MoO <sub>3</sub>	3.07		
		P <sub>2</sub> O <sub>5</sub> (12.1M H <sub>3</sub> PO <sub>4</sub> )	3.15		
		TeO <sub>2</sub>	0.36		
	11/3/77	76-199 Frit	45 kg	26 kg	---

B.7

LFCM RUN SUMMARY (8)

Run No.	Date	Feed		Glass Poured, kg	Duration of Run																					
		Composition	Amount																							
LF-12	11/4/77	See Run LF-11	460 L @ 98 L/h	224 kg	4.7 h																					
LF-13	11/8/77- 11/11/77	See Run LF-11	1050 L @ 97 L/h	447 kg	10.9 h run time over period of 3 days																					
	11/17/77		---	1 kg	---																					
	11/18/77		---	72 kg	---																					
LF-14	11/22/77	Glass Formers	130 L @ 110 L/h	158 lb	1.2 h																					
		<table border="0" style="margin-left: 20px;"> <tr> <td style="border-bottom: 1px solid black;">Oxide (Form)</td> <td style="border-bottom: 1px solid black;">wt%</td> <td rowspan="8" style="font-size: 3em; vertical-align: middle; padding-left: 10px;">}</td> <td rowspan="8" style="vertical-align: middle;">67 wt%</td> </tr> <tr> <td>SiO<sub>2</sub>(SiO<sub>2</sub>)</td> <td>35.4</td> </tr> <tr> <td>B<sub>2</sub>O<sub>3</sub>(H<sub>3</sub>BO<sub>3</sub>)</td> <td>9.3</td> </tr> <tr> <td>TiO<sub>2</sub>(TiO<sub>2</sub>)</td> <td>6.0</td> </tr> <tr> <td>Al<sub>2</sub>O<sub>3</sub>(Al<sub>2</sub>O<sub>3</sub>)</td> <td>1.0</td> </tr> <tr> <td>Na<sub>2</sub>O(NaNO<sub>3</sub>)</td> <td>8.0</td> </tr> <tr> <td>K<sub>2</sub>O(KNO<sub>3</sub>)</td> <td>2.0</td> </tr> <tr> <td>CaO(CaCO<sub>3</sub> + Ca(NO<sub>3</sub>)<sub>2</sub>)</td> <td>2.0</td> </tr> <tr> <td>CuO</td> <td>Not Available</td> <td></td> <td></td> </tr> </table>	Oxide (Form)	wt%	}	67 wt%	SiO <sub>2</sub> (SiO <sub>2</sub> )	35.4	B <sub>2</sub> O <sub>3</sub> (H <sub>3</sub> BO <sub>3</sub> )	9.3	TiO <sub>2</sub> (TiO <sub>2</sub> )	6.0	Al <sub>2</sub> O <sub>3</sub> (Al <sub>2</sub> O <sub>3</sub> )	1.0	Na <sub>2</sub> O(NaNO <sub>3</sub> )	8.0	K <sub>2</sub> O(KNO <sub>3</sub> )	2.0	CaO(CaCO <sub>3</sub> + Ca(NO <sub>3</sub> ) <sub>2</sub> )	2.0	CuO	Not Available				
Oxide (Form)	wt%	}	67 wt%																							
SiO <sub>2</sub> (SiO <sub>2</sub> )	35.4																									
B <sub>2</sub> O <sub>3</sub> (H <sub>3</sub> BO <sub>3</sub> )	9.3																									
TiO <sub>2</sub> (TiO <sub>2</sub> )	6.0																									
Al <sub>2</sub> O <sub>3</sub> (Al <sub>2</sub> O <sub>3</sub> )	1.0																									
Na <sub>2</sub> O(NaNO <sub>3</sub> )	8.0																									
K <sub>2</sub> O(KNO <sub>3</sub> )	2.0																									
CaO(CaCO <sub>3</sub> + Ca(NO <sub>3</sub> ) <sub>2</sub> )	2.0																									
CuO	Not Available																									
		PW-7a Liquid Waste (see Run LF-11, 11/2/77)																								
	11/28/77	---		31 lb	---																					
LF-15	11/28/77	Batch Chemical Glass Formers and PW-7a Liquid Waste (see Run LF-14)	60 L @ 100 L/h		35 min																					
	11/77	---		5 kg	---																					
	11/77	---		4 kg	---																					
	11/77	---		463 kg	---																					
	11/77	76-199 Frit (see Run LF-11)	215 kg	---	---																					
	11/77	76-199 Frit	227 kg																							

LFCM RUN SUMMARY (9)

Run No.	Date	Feed		Glass Poured, kg	Duration of Run	
		Composition	Amount			
LF-15 (contd)	11/77	76-199 Frit	34 kg			
	11/77	---	---	8 kg		
	11/77	---	---	24 kg		
LF-16	12/13/77	Batch Chemical Glass Formers and PW-7a Liquid Waste (see Run LF-14)	~60 L @ 65 L/h	---	55 min	
LF-17	12/28/77	76-199 + PW-7a in 2/1 Ratio	133 L @ 30 L/h	62 kg	4.4 h	
	1/3/78	---	---	41 kg	---	
	1/6/78	76-199 Frit	159 kg	79 kg	---	
	1/28/78	76-199 Frit	45 kg	---	---	
	1/30/78	---	---	29 kg	---	
	2/1/78	---	---	~10 kg	---	
	2/13/78	---	---	159 kg	1.1 h	
	2/14/78	---	---	142 kg	1.9 h	
	2/21/78	---	---	56 kg	1.1 h	
	2/22/78	---	---	67 kg	1.0 h	
	3/6/78	Washout Frit	1719 kg @ 66 kg/h	1200 kg	26 h	
	3/13/78	76-101 - 87 wt% (see Run 2)				
			Na <sub>2</sub> O(Na <sub>2</sub> CO <sub>3</sub> )	4 wt%		
			CaO(CaCO <sub>3</sub> )	4 wt%		
		B <sub>2</sub> O <sub>3</sub> (H <sub>3</sub> BO <sub>3</sub> )	5 wt%			
3/14/78	Washout Frit (see 3/6 to 3/13/78)	286 kg @ 119 kg/h	146 kg	2.4 h		

LFCM RUN SUMMARY (10)

Run No.	Date	Feed		Glass Poured, kg	Duration of Run
		Composition	Amount		
SRL-3	3/15/78- 3/22/78	Savannah River	4140 kg @ 47 kg/h	3430 kg	89 h
		<u>Composite Glass Composition in Chemical Form, wt%</u>			
	SiO <sub>2</sub>	39.4			
	Na <sub>2</sub> O(Na <sub>2</sub> CO <sub>3</sub> )	13.8			
	TiO <sub>2</sub>	7.5			
	B <sub>2</sub> O <sub>3</sub> (H <sub>3</sub> BO <sub>3</sub> )	7.5			
	CaO(CaCO <sub>3</sub> )	4.6			
	Li <sub>2</sub> O(Li <sub>2</sub> CO <sub>3</sub> )	3.0			
	Fe <sub>2</sub> O <sub>3</sub>	8.4			
	Al <sub>2</sub> O <sub>3</sub>	12.3			
	MnO <sub>2</sub>	2.8			
	NiO	0.6			
	Na <sub>2</sub> O(Na <sub>2</sub> SO <sub>4</sub> )	0.1			
	SRL-4	3/31/78	<u>Glass Formers, wt%</u>		
		SiO <sub>2</sub>	39.4		
		TiO	7.5		
		Na <sub>2</sub> O(Na <sub>2</sub> CO <sub>3</sub> )	4.1		
		B <sub>2</sub> O <sub>3</sub> (H <sub>3</sub> BO <sub>3</sub> )	7.5		
		CaO(CaCO <sub>3</sub> )	3.7		
		Li <sub>2</sub> O(Li <sub>2</sub> CO <sub>3</sub> )	3.0		
		<u>Spray Calcined Waste, wt%</u>			
		Na <sub>2</sub> O(Na <sub>2</sub> CO <sub>3</sub> )	9.8		
		CaO(CaCO <sub>3</sub> )	0.9		
		Fe <sub>2</sub> O <sub>3</sub> (Fe(OH) <sub>3</sub> )	8.4		
		Al <sub>2</sub> O <sub>3</sub> (Al(OH) <sub>3</sub> )	12.3		
		MnO <sub>2</sub>	2.8		
		NiO(Ni(OH) <sub>2</sub> )	0.6		
		Na <sub>2</sub> O(Na <sub>2</sub> SO <sub>4</sub> )	0.1		

B.10

LFCM RUN SUMMARY (11)

Run No.	Date	Feed		Glass Poured, kg	Duration of Run	
		Composition	Amount			
SRL-5	4/4/78	<u>Glass Formers, wt%</u>		435 kg @ 75 kg/h	372 kg (401 kg theoretical)	5.8 h
		SiO <sub>2</sub> (SiO <sub>2</sub> +CaSiO <sub>3</sub> )	39.4			
		TiO	7.5			
		Na <sub>2</sub> O(Na <sub>2</sub> B <sub>4</sub> O <sub>7</sub> +Na <sub>2</sub> CO <sub>3</sub> )	4.1			
		B <sub>2</sub> O <sub>3</sub> (Na <sub>2</sub> B <sub>4</sub> O <sub>7</sub> )	7.5			
		CaO(CaSiO <sub>3</sub> )	3.7			
		Li <sub>2</sub> O(LiOH·H <sub>2</sub> O)	3.0			
		<u>Spray-Calcined Waste, wt%</u>				
		See Run SRL-4	34.9			
		SRL-6	4/5/78			
<u>218-Premelted Frit, wt%</u>						
SiO <sub>2</sub>	39.4					
TiO	7.5					
Na <sub>2</sub> O	4.1					
B <sub>2</sub> O <sub>3</sub>	7.5					
CaO	3.7					
Li <sub>2</sub> O	3.0					
<u>Spray-Calcined Waste, wt%</u>						
See Run SRL-4	39.4					
SRL-7	4/6/78	<u>Glass Formers</u>		461 kg @ 88 kg/h	451 kg (455 kg theoretical)	5.2 h
		<u>21-Premelted Frit, wt%</u>				
		SiO <sub>2</sub>	39.4			
		TiO	7.5			
		Na <sub>2</sub> O	13.9			
		B <sub>2</sub> O <sub>3</sub>	7.5			
		CaO	3.7			
		Li <sub>2</sub> O	3.0			

B.11

LFCM RUN SUMMARY (12)

Run No.	Date	Composition	Amount	Glass Poured, kg	Duration of Run
SRL-7 (contd)		<u>Spray-Calcined Waste, wt%</u>			
		CaO(CaCO <sub>3</sub> )	0.9		
		Fe <sub>2</sub> O <sub>3</sub> (Fe(OH) <sub>3</sub> )	8.4		
		Al <sub>2</sub> O <sub>3</sub> (Al(OH) <sub>3</sub> )	12.3		
		MnO <sub>2</sub>	2.8		
		NiO(Ni(OH) <sub>2</sub> )	0.6		
		Na <sub>2</sub> O(Na <sub>2</sub> SO <sub>4</sub> )	0.1		
SRL-8 & 9	4/11/78	<u>Glass Formers</u>	800 kg @ 91 kg/h	794 kg (773 kg theoretical)	8.8 h
		<u>21-BX-Premelted Frit, wt%</u>			
		SiO <sub>2</sub>	39.4		
		Na <sub>2</sub> O	4.1		
		B <sub>2</sub> O <sub>3</sub>	7.5		
		CaO	3.7		
		Li <sub>2</sub> O	3.0		
Eliminated in Run SRL-9	→	<u>Chemicals, wt%</u>			
		TiO	7.5		
		<u>Spray-Calcined Waste, wt%</u>			
		See Run SRL-4	39.4		
SRL-10	4/12/78	<u>Glass Formers</u>	457 kg @ 80 kg/h	460 kg (441 kg theoretical)	5.7 h
		<u>218-Premelted Frit, wt%</u>			
		See Run SRL-6			
		<u>Spray-Calcined Waste (TNX), wt%</u>			
		Awaiting Chemical Analysis			
	4/13/78	76-199 Premelted Frit	91 kg	---	---

B.12

LFCM RUN SUMMARY (13)

Run No.	Date	Feed		Glass Poured, kg	Duration of Run	
		Composition	Amount			
76-101 Flushout Run	4/19/78- 4/20/78	76-101 Premelted Frit	87 wt%	2877 kg @ 85 kg/h	2914 kg	33.5 h (Includes 4 h Shutdown)
		Na <sub>2</sub> O(Na <sub>2</sub> CO <sub>3</sub> )	4 wt%			
	CaO(CaCO <sub>3</sub> )	4 wt%				
	B <sub>2</sub> O <sub>3</sub> (H <sub>3</sub> BO <sub>3</sub> or B <sub>2</sub> O <sub>3</sub> )	5 wt%				
	5/26/78	76-199 Premelted Frit		136 kg	64 kg	---
	6/2/78	76-199 Premelted Frit				
	6/6/78	76-199 Premelted Frit				
LF-21	6/9/78	73-1 Premelted Frit +PW-4b (2M HNO <sub>3</sub> ) Waste in a Glass Weight Ratio of 2.75/1.0		~450 L @ ~54 L/h	137 kg	8.4
		<u>73-1 Premelted Frit</u>	<u>wt%</u>	} 73 wt%		
			<u>Oxide</u>			
		SiO <sub>2</sub>	27.1			
		ZnO	21.2			
		B <sub>2</sub> O <sub>3</sub>	11.1			
		CaO	1.5			
		MgO	1.5			
		K <sub>2</sub> O	4.0			
		Na <sub>2</sub> O	4.073			
		SrO	1.5			
		BaO	1.5			
		<u>PW-4b Waste (2M HNO<sub>3</sub>)</u>				
		<u>PW-0</u>	<u>wt%</u>	}		
			<u>Oxide</u>			
		Ag <sub>2</sub> O(AgNO <sub>3</sub> )	0.06			
		BaO(Ba(NO <sub>3</sub> ) <sub>2</sub> )	1.11			
		CdO(Cd(NO <sub>3</sub> ) <sub>2</sub> ·4H <sub>2</sub> O)	0.07			
		CoO(Co(NO <sub>3</sub> ) <sub>3</sub> ·6H <sub>2</sub> O)	0.20			

B.13

LFCM RUN SUMMARY (14)

Run No.	Date	Feed		Glass Poured, kg	Duration of Run	
		Composition	Amount			
LF-21		Cr <sub>2</sub> O <sub>3</sub> (Cr(NO <sub>3</sub> ) <sub>3</sub> · 9H <sub>2</sub> O)	0.24	} 27 wt%		
		Fe <sub>2</sub> O <sub>3</sub> (Fe(NO <sub>3</sub> ) <sub>3</sub> · 9H <sub>2</sub> O)	2.34			
		K <sub>2</sub> O(KNO <sub>3</sub> )	0.81			
		NiO(Ni(NO <sub>3</sub> ) <sub>2</sub> · 6H <sub>2</sub> O)	0.74			
		SrO(Sr(NO <sub>3</sub> ) <sub>2</sub> )	0.75			
		ZrO <sub>2</sub> (ZrO(NO <sub>3</sub> ) <sub>2</sub> · 2H <sub>2</sub> O)	3.52			
		Ce <sub>2</sub> O <sub>3</sub>	2.7			
		RE <sub>2</sub> O <sub>3</sub>	7.65			
		MoO <sub>3</sub>	4.51			
		<u>Additives</u>				
		TeO <sub>2</sub>	0.53			
		P <sub>2</sub> O <sub>5</sub> (12.1M H <sub>3</sub> PO <sub>4</sub> )	0.51			
	6/13/78	---	---	3 kg	---	
LF-22	6/15/78	73-1 Premelted Frit + PW-4b Waste + Full Cs and 20% Ru Concentration in a Frit/Waste Ratio of 2.4/1		505 L @ 68 L/h	72 kg	7.4 h
		<u>73-1 Premelted Frit</u>	<u>wt% Oxide</u>			
		SiO <sub>2</sub>	26.1	} 71 wt%		
		ZnO	20.4			
		B <sub>2</sub> O <sub>3</sub>	10.7			
		CaO	1.4			
		MgO	1.4			
		K <sub>2</sub> O	3.9			
		Na <sub>2</sub> O	3.9			
		SrO	1.4			
		BaO	1.4			

B.14

LFCM RUN SUMMARY (15)

Run No.	Date	Composition	Feed	Amount	Glass Poured, kg	Duration of Run
LF-22 (contd)		PW-4b Waste (2M HNO <sub>3</sub> )				
		<u>PW-0</u>	<u>wt%</u>			
		Ag <sub>2</sub> O(AgNO <sub>3</sub> )	Oxide			
		BaO(Ba(NO <sub>3</sub> ) <sub>2</sub> )				
		CdO(Cd(NO <sub>3</sub> ) <sub>2</sub> ·4H <sub>2</sub> O)				
		CoO(Co(NO <sub>3</sub> ) <sub>2</sub> ·6H <sub>2</sub> O)				
		Cr <sub>2</sub> O <sub>3</sub> (Cr(NO <sub>3</sub> ) <sub>3</sub> ·9H <sub>2</sub> O)				
		Fe <sub>2</sub> O <sub>3</sub> (Fe(NO <sub>3</sub> ) <sub>3</sub> ·9H <sub>2</sub> O)				
		K <sub>2</sub> O(KNO <sub>3</sub> )				
		NiO(Ni(NO <sub>3</sub> ) <sub>2</sub> ·6H <sub>2</sub> O)				
		SrO(Sr(NO <sub>3</sub> ) <sub>2</sub> )				
		ZrO <sub>2</sub> (ZrO(NO <sub>3</sub> ) <sub>2</sub> ·2H <sub>2</sub> O)				
		Ce <sub>2</sub> O <sub>3</sub>				
		RE <sub>2</sub> O <sub>3</sub>				
		MoO <sub>3</sub>				
		<u>Additives</u>				
		TeO <sub>2</sub>				
		P <sub>2</sub> O <sub>5</sub> (12.1M H <sub>3</sub> PO <sub>4</sub> )				
		Cs <sub>2</sub> O(CsNO <sub>3</sub> )				
		RuO <sub>2</sub> (RU(NO <sub>3</sub> ) <sub>2</sub> )				
			29 wt%			
	6/22/78	---		---	3 kg	---

B.15

LFCM RUN SUMMARY (16)

Run No.	Date	Feed		Glass Poured, kg	Duration of Run	
		Composition	Amount			
LF-23	7/7/78	73-1 Frit + PW-4b Waste in a 2/1 Oxide Ratio		703 L @ 81 L/h	324 kg	8.7 h
	7/7/78	---		---	321 kg	
	7/25/78- 7/26/78	Flushout Glass	wt% Oxide	1360 kg @ 65 kg/h	643 kg	21 h
		76-101 Frit	87			
		Na <sub>2</sub> O(Na <sub>2</sub> CO <sub>3</sub> )	4			
		CaO(CaCO <sub>3</sub> )	4			
		B <sub>2</sub> O <sub>3</sub> (H <sub>3</sub> BO <sub>3</sub> )	5			
	8/1/78- 8/2/78	76-101	87	2040 kg @ 92 kg/h	2040 kg	22.3 h
		Na <sub>2</sub> O(Na <sub>2</sub> CO <sub>3</sub> )	4			
		CaO(CaCO <sub>3</sub> )	4			
		B <sub>2</sub> O <sub>3</sub> (H <sub>3</sub> BO <sub>3</sub> )	5			
	8/11/78	---		---	8 kg	---
	8/14/78	---		---	14 kg	---
	8/15/78- 8/16/78	76-199 Frit		2050 kg @ 104 kg/h	1951 kg	19.7 h
				6560 L, 33, 800 kg	31,000. kg	At Temp. 18 mo 592 h
Reboil Test	8/28/78(a)	76-199 Frit		~50 kg @ ~9 kg/h	41 kg	5.6 h(a)
	9/12/78	76-199		~360 kg @ 113 kg/h	362 kg	3.2 h
	9/12/78- 10/12/78	---		---	70 kg	
	10/16/78	Frit 21A (SRL) + Soda Ash Fed Through Independent Feeders to Get Frit 21 (SRL Composition)		179 kg Frit + ~50 kg Soda Ash	273 kg	1.8 h

(a) Because feedrate was intentionally kept low, operating time not included in total.

LFCM RUN SUMMARY (17)

Run No.	Date	Feed		Glass Poured, kg	Duration of Run
		Composition	Amount		
	10/16/78	<u>Frit 21A</u>	178 kg + ~45 kg Soda Ash	127 kg	1.5 h
		<u>wt%</u> SiO <sub>2</sub>			
		Na <sub>2</sub> O			
		B <sub>2</sub> O <sub>3</sub>			
		TiO <sub>2</sub>			
		Li <sub>2</sub> O			
		CaO			
		Na <sub>2</sub> O(Na <sub>2</sub> CO <sub>3</sub> )			
			100.0		
	10/18/78	Frit 21A + Soda Ash Through Separate Feeders	240 kg Frit + ~57 kg Soda Ash	194 kg	1.9 h
	10/18/78	Frit 21A + Soda Ash Through Separate Feeders	152 kg Frit + ~45 kg Soda Ash	143 kg	1.5 h
	10/19/78	Frit 21A + Soda Ash Through Separate Feeders	205 kg Frit + ~47 kg Soda Ash	218 kg	1.6 h
	10/20/78	Frit 21A + Soda Ash Through Separate Feeders	56 kg Frit + ~15 kg Soda Ash	43 kg	0.5 h
	10/25/78	Frit 21A + Soda Ash Through Separate Feeders	308 kg Frit (150 kg-- remaining kg Soda Ash <sup>(a)</sup> )	163 kg	
	10/30/78	Frit 21A + Soda Ash Through Separate Feeders	308 kg Frit (150 kg-- remaining kg Soda Ash <sup>(a)</sup> )	35 kg	
Flushout	11/1/78	PEMCO Frit <u>SC-2234-P</u>	~900 kg @ 96.4 kg/h	904 kg	9.3 h
		<u>wt%</u> SiO <sub>2</sub>			
		B <sub>2</sub> O <sub>3</sub>			
		CaO			
		Na <sub>2</sub> O			
			99.7		

B.17

(a) For all Frit 21A fed to melters from 10/16 to 10/30, the feed was sodium-deficient by (remaining) kg.

LFCM RUN SUMMARY (18)

Run No.	Date	Feed		Glass Poured, kg	Duration of Run																	
		Composition	Amount																			
LF-24	11/3/78	73-1 Frit + PW-4b Waste in 2.5/1 Oxide Ratio Including 20% Ru and 100% Cs Loading	415 L	86 kg	7.0 h																	
	11/9/78	---	---	18 kg	---																	
LF-25	11/14/78	73-1 Frit + PW-4b Waste in ~3.0/1 Oxide Ratio. No Cs Added	840 L @ 68 L/h	289 kg	12.3 h																	
		<table style="margin-left: 20px;"> <tr> <td></td> <td style="text-align: center;"><u>wt%</u></td> <td></td> </tr> <tr> <td></td> <td style="text-align: center;"><u>Oxide</u></td> <td></td> </tr> <tr> <td>PW-0</td> <td rowspan="3" style="vertical-align: middle;">}</td> <td rowspan="3" style="vertical-align: middle;">23.6</td> </tr> <tr> <td>H<sub>3</sub>PO<sub>4</sub></td> </tr> <tr> <td>TeO<sub>2</sub></td> </tr> <tr> <td>73-1 Frit</td> <td></td> <td>76.4</td> </tr> <tr> <td>2M HNO<sub>3</sub></td> <td></td> <td></td> </tr> </table>		<u>wt%</u>			<u>Oxide</u>		PW-0	}	23.6	H <sub>3</sub> PO <sub>4</sub>	TeO <sub>2</sub>	73-1 Frit		76.4	2M HNO <sub>3</sub>					
	<u>wt%</u>																					
	<u>Oxide</u>																					
PW-0	}	23.6																				
H <sub>3</sub> PO <sub>4</sub>																						
TeO <sub>2</sub>																						
73-1 Frit		76.4																				
2M HNO <sub>3</sub>																						
LF-26	11/16/78	73-1 Frit + PW-4b Waste in ~3.0/1 Oxide Ratio; No Cs; 2M HNO <sub>3</sub> Solution	430 L @ 65 L/h	90 kg	6.6 h																	
SRL-11	12/10/78- 12/15/78	SRL Composite Synthetic Calcine + Glass Former 411	6140 kg @ 52 kg/h	4962 kg @ 42 kg/h	119 h																	

Glass Formers

Oxide	Form	wt% Oxide	
SiO <sub>2</sub>	(-200 Mesh Silica)	43.72	} 75 wt%
B <sub>2</sub> O <sub>3</sub>	(Na <sub>2</sub> B <sub>4</sub> O <sub>7</sub> Anhydrous)	8.32	
CaO	(CaSiO <sub>3</sub> Wollastanite)	4.20	
Li <sub>2</sub> O	(Li <sub>2</sub> CO <sub>3</sub> )	9.37	
Na <sub>2</sub> O	(Na <sub>2</sub> CO <sub>3</sub> + Anhydrous Borax)	3.72	

Synthetic Calcine

Oxide	Form	wt% Oxide	
Al <sub>2</sub> O <sub>3</sub>	(Alumina)	12.31	} 25 wt%
Fe <sub>2</sub> O <sub>3</sub>	(Red Iron Powder)	8.47	
MnO <sub>2</sub>		2.73	
CaO	(CaCO <sub>3</sub> )	0.84	
NiO	(NiO)	0.63	

B.18

LFCM RUN SUMMARY (19)

Run No.	Date	Feed		Glass Poured, kg	Duration of Run
		Composition	Amount		
SRL-12	1/10/79	SRL Composite Synthetic Calcine + Premelted Frit 411. Glass Former Same as that in SRL-11 but Premelted.	733 kg @ 96 kg/h	753 kg	7.75 h
LF-27	1/15/79- 1/16/79	PW-4b Liquid Waste + 73-1 Frit in 3/1 Ratio	1090 L @ 51 L/h	278 kg	21.1 h
LF-28	1/23/79	PW-4b Liquid Waste + 73-1 Frit in a 2.8/1 Ratio.	430 L @ 46 L/h	90 kg	8.9 h
SRL-13	7/23/79	SRL TDS Calcine Premixed With Premelted Frit-211	4900 kg	4490 kg	114.5 h

Premelted Frit-211  
(-20 + 80 Mesh)

Oxide	wt%
SiO <sub>2</sub>	58.3
Na <sub>2</sub> O	20.6
B <sub>2</sub> O <sub>3</sub>	11.1
CaO	5.6
Li <sub>2</sub> O	4.4

} 72 wt% of  
Total  
Oxides

Commercially Dried TDS Calcine

Oxide	Form	wt% Oxide
Fe <sub>2</sub> O <sub>3</sub>	(Fe(OH) <sub>3</sub> )	14.6
Al <sub>2</sub> O <sub>3</sub>	(Al(OH) <sub>3</sub> )	3.2
MnO <sub>2</sub>		3.9
CaO	(CaCO <sub>3</sub> )	1.0
NiO	(Ni(OH) <sub>2</sub> )	1.7
Na <sub>2</sub> O	(NaNO <sub>3</sub> )	0.3
Na <sub>2</sub> SO <sub>4</sub>		0.4
Zeolite	Linde Ion Siv IE-95	2.9

} 28 wt% of  
Total  
Oxides

B.19

LFCM RUN SUMMARY (20)

Run No.	Date	Feed		Glass Poured, kg	Duration of Run
		Composition	Amount		
Marble Machine Run	8/30/79	See Run SRL-13	~140 kg	~125 kg	5.7 h
Marble Machine Run	9/6/79-9/7/79	See Run SRL-13	~90	~80	9.6 h
SRL-14	10/1/79-10/4/79	See Run SRL-13 Except Between 0.5 to 1 wt% Cornstarch on a Total Oxide Basis was Added		~2400 kg	64.5 h
SRL-LF-1	1/14/80-1/17/80	SRL TDS Waste + Premelted Frit-211	2900 L	1050 kg	65.5 h

Oxide	wt%
Fe(OH) <sub>3</sub>	17.5
Al(OH) <sub>3</sub>	4.38
MnO <sub>2</sub>	3.5
Ni(OH) <sub>2</sub>	1.88
CaCO <sub>3</sub>	1.6
NaNO <sub>3</sub>	0.73
Na <sub>2</sub> SO <sub>4</sub>	0.35
Zeolite	2.6
RuNO(NO <sub>3</sub> ) <sub>3</sub>	0.51
Sb <sub>2</sub> O <sub>3</sub>	0.020
TeO <sub>2</sub>	0.006
Cs <sub>2</sub> CO <sub>3</sub>	0.059
Sr(NO <sub>3</sub> ) <sub>2</sub>	0.042
Cornstarch	1.8
Bentonite	1.95
Frit-211 (see SRL-13)	64.5

DISTRIBUTION

No. of  
Copies

No. of  
Copies

OFFSITE

A. A. Churm  
DOE Chicago Patent Group  
9800 South Cass Avenue  
Argonne, IL 60439

R. Y. Lowrey  
DOE Albuquerque Operations  
Office  
P.O. Box 5400  
Albuquerque, NM 87185

A. L. Taboas  
DOE Albuquerque Operations  
Office  
P.O. Box 5400  
Albuquerque, NM 87185

S. A. Mann  
DOE Chicago Operations and  
Region Office  
Argonne, IL 60439

J. O. Neff  
Department of Energy  
Columbus Program Office  
505 King Avenue  
Columbus, OH 43201

W. E. Mott  
DOE Division of Environmental  
Control Technology  
Washington, DC 20545

J. P. Hamric  
DOE Idaho Operations Office  
550 2nd St.  
Idaho Falls, ID 83401

J. W. Peel  
DOE Idaho Operations Office  
550 2nd St.  
Idaho Falls, ID 83401

J. B. Whitsett  
DOE Idaho Operations Office  
550 2nd St.  
Idaho Falls, ID 83401

C. R. Cooley  
DOE Nuclear Waste Management  
Programs  
NE-331, GTN  
Washington, DC 20545

G. H. Daly  
DOE Nuclear Waste Management  
Programs  
NE-322, GTN  
Washington, DC 20545

J. E. Dieckhoner  
DOE Nuclear Waste Management  
Programs  
NE-321, GTN  
Washington, DC 20545

C. H. George  
DOE Nuclear Waste Management  
Programs  
NE-330, GTN  
Washington, DC 20545

C. A. Heath  
DOE Nuclear Waste Management  
Programs  
NE-330, GTN  
Washington, DC 20545

M. L. Lawrence  
DOE Nuclear Waste Management  
Programs  
NE-340, GTN  
Washington, DC 20545

No. of  
Copies

D. J. McGoff  
DOE Nuclear Waste Management  
Programs  
NE-320, GTN  
Washington, DC 20545

S. Meyers/R. Romatowski  
DOE Nuclear Waste Management  
Programs  
NE-30, GTN  
Washington, DC 20545

G. Oertel  
DOE Nuclear Waste Management  
Programs  
NE-320, GTN  
Washington, DC 20545

A. F. Perge  
DOE Nuclear Waste Management  
Programs  
NE-30, GTN  
Washington, DC 20545

R. W. Ramsey, Jr.  
DOE Nuclear Waste Management  
Programs  
NE-301, GTN  
Washington, DC 20545

V. Trice  
DOE Nuclear Waste Management  
Program  
NE-30, GTN  
Washington, DC 20545

D. L. Vieth  
DOE Nuclear Waste Management  
Programs  
NE-332, GTN  
Washington, DC 20545

S. W. Ahrends  
DOE Oak Ridge Operations Office  
P.O. Box E  
Oak Ridge, TN 37830

No. of  
Copies

D. E. Large  
DOE Oak Ridge Operations Office  
P.O. Box E  
Oak Ridge, TN 37830

S. G. Harbinson  
DOE San Francisco Operations  
Office  
1333 Broadway  
Oakland, CA 94612

W. B. Wilson  
DOE Savannah River Operations  
Office  
P.O. Box A  
Aiken, SC 29801

R. P. Whitfield  
DOE Savannah River Operations  
Office  
P.O. Box A  
Aiken, SC 29801

J. B. Martin  
Division of Waste Management  
Nuclear Regulatory Commission  
Washington, DC 20555

D. B. Rohrer  
Division of Waste Management  
Nuclear Regulatory Commission  
Washington, DC 20555

R. D. Smith  
Division of Waste Management  
Nuclear Regulatory Commission  
Washington, DC 20555

R. E. Cunningham  
Office of Nuclear Safety  
Materials and Safeguards  
Nuclear Regulatory Commission  
Room 562, 7915 Eastern Avenue  
Silver Springs, MD 20910

27 DOE Technical Information Center

No. of  
Copies

J. A. Buckham  
Allied-General Nuclear Services  
P.O. Box 847  
Barnwell, SC 29812

A. Williams  
Allied-General Nuclear Services  
P.O. Box 847  
Barnwell, SC 29812

J. H. Kittel  
Argonne National Laboratory  
Office of Waste Management  
Programs  
9700 South Cass Avenue  
Argonne, IL 60439

M. J. Steindler/L. E. Trevorrow  
Argonne National Laboratory  
9700 South Cass Avenue  
Argonne, IL 60439

W. Carbiener  
Battelle Memorial Institute  
Office of Nuclear Waste  
Isolation  
505 King Avenue  
Columbus, OH 43201

Beverly Rawles  
Battelle Memorial Institute  
Office of Nuclear Waste  
Isolation  
505 King Avenue  
Columbus, OH 43201

Research Library  
Battelle Memorial Institute  
505 King Avenue  
Columbus, OH 43201

R. Maher, Program Manager  
Waste Management Programs  
Savannah River Plant  
E. I. Du Pont de Nemours & Co.  
Aiken, SC 29801

No. of  
Copies

M. D. Boersma  
E. I. Du Pont de Nemours & Co.  
Savannah River Laboratory  
Aiken, SC 29801

R. G. Garvin  
E. I. Du Pont de Nemours & Co.  
Savannah River Laboratory  
Aiken, SC 29801

D. L. McIntosh  
E. I. Du Pont de Nemours & Co.  
Savannah River Laboratory  
Aiken, SC 29801

A. L. Ayers  
EG & G Idaho  
P.O. Box 1625  
Idaho Falls, ID 83415

R. Williams  
Electric Power Research  
Institute  
3412 Hillview Avenue  
Palo Alto, CA 94304

Environmental Protection Agency  
Technological Assessment  
Division (AW-559)  
Office of Radiation Programs  
U.S. Environmental Protection  
Agency  
Washington, DC 20460

J. R. Berreth  
Exxon Nuclear Idaho  
P.O. Box 2800  
Idaho Falls, ID 83401

G. L. Ritter  
Exxon Nuclear Idaho  
P.O. Box 2800  
Idaho Falls, ID 83401

File Copy  
Exxon Nuclear Idaho  
P.O. Box 2800  
Idaho Falls, ID 83401

No. of  
Copies

J. Campbell  
Lawrence Livermore Laboratory  
P.O. Box 808  
Livermore, CA 94550

R. Roy  
202 Materials Research  
Laboratory  
Pennsylvania State University  
University Park, PA 16802

R. E. Blanco  
Oak Ridge National Laboratory  
P.O. Box Y  
Oak Ridge, TN 37830

A. L. Lotts  
Oak Ridge National Laboratory  
P.O. Box X  
Oak Ridge, TN 37830

A. B. Martin  
Rockwell International  
Energy Systems Group  
8900 DeSoto Avenue  
Canoga Park, CA 91304

Paul Hagen  
Chemical Operations  
Rockwell International  
Rocky Flats Plant  
P.O. Box 464  
Golden, CO 80401

E. Vejvoda, Director  
Chemical Operations  
Rockwell International  
Rocy Flats Plant  
P.O. Box 464  
Golden, CO 80401

R. G. Kepler  
Organic and Electronic  
Dept. 5810  
Sandia Laboratories  
Albuquerque, NM 87185

No. of  
Copies

D. E. Harrison  
Westinghouse Electric Corp.  
P.O. Box 355  
Pittsburgh, PA 15230

P. B. Macedo  
Keane Hall  
Vitreous State Laboratory  
The Catholic University of  
America  
Washington, DC 20017

L. L. Hench  
Dept. of Materials Science  
and Engineering  
University of Florida  
Gainesville, FL 32611

ONSITE

4 DOE Richland Operations Office

P. A. Craig (2)  
R. E. Gerton  
H. E. Ransom

2 Rockwell Hanford Operations

I. E. Reep  
D. D. Wodrich

UNC United Nuclear Industries

F. H. Bouse

Westinghouse Hanford Company

A. G. Blasewitz

52 Pacific Northwest Laboratory

S. M. Barnes (5)  
W. J. Bjorklund  
W. F. Bonner  
R. A. Brouns

No. of  
Copies

Pacific Northwest Laboratory  
(contd)

J. L. Buelt  
D. B. Cearlock  
T. D. Chikalla  
R. D. Dierks  
J. W. Finnigan  
C. R. Hann  
M. S. Hanson  
A. J. Haverfield  
J. H. Jarrett  
R. S. Kemper  
D. E. Knowlton  
L. T. Lakey  
D. E. Larson (5)  
J. M. Latkovich  
G. B. Long (3)  
B. K. Marshall  
R. P. Marshall  
J. L. McElroy  
G. B. Mellinger  
R. D. Nelson  
R. E. Nightingale  
D. E. Olesen  
A. M. Platt  
W. A. Ross  
J. M. Rusin  
D. H. Siemens  
R. L. Treat  
R. P. Turcotte  
H. H. Van Tuyl  
B. E. Vaughan  
L. D. Williams  
Technical Information (5)  
Publishing Coordination EI (2)